Phenomenology and LHC Signatures of Exotic Fermions

By

TANUMOY MANDAL

PHYS10200705002

The Institute of Mathematical Sciences, Chennai

A thesis submitted to the

Board of Studies in Physical Sciences

In partial fulfilment of requirements

For the Degree of

DOCTOR OF PHILOSOPHY

of

HOMI BHABHA NATIONAL INSTITUTE

September, 2013

Homi Bhabha National Institute

Recommendations of the Viva Voce Board

As members of the Viva Voce Board, we certify that we have read the dissertation prepared by **Tanumoy Mandal** entitled **“Phenomenology and LHC Signatures of Exotic Fermions”** and recommend that it maybe accepted as fulfilling the dissertation requirement for the Degree of Doctor of Philosophy.

____ Date:

Guide -

____ Date:

Member 1 -

____ Date:

Member 2 -

____ Date:

Member 3 -

____ Date:

External examiner -

Final approval and acceptance of this dissertation is contingent upon the candidate’s submission of the final copies of the dissertation to HBNI.

I hereby certify that I have read this dissertation prepared under my direction and recommend that it may be accepted as fulfilling the dissertation requirement.

Date: Guide: ____________________

Place:

STATEMENT BY AUTHOR

This dissertation has been submitted in partial fulfillment of requirements for an advanced degree at Homi Bhabha National Institute (HBNI) and is deposited in the Library to be made available to borrowers under rules of the HBNI.

Brief quotations from this dissertation are allowable without special permission, provided that accurate acknowledgement of source is made. Requests for permission for extended quotation from or reproduction of this manuscript in whole or in part may be granted by the Competent Authority of HBNI when in his or her judgment the proposed use of the material is in the interests of scholarship. In all other instances, however, permission must be obtained from the author.

Tanumoy Mandal

DECLARATION

I, hereby declare that the investigation presented in the thesis has been carried out by me. The work is original and has not been submitted earlier as a whole or in part for a degree/diploma at this or any other Institute/University.

Tanumoy Mandal

DEDICATIONS

... to my parents and Madhumita ...

ACKNOWLEDGEMENTS

First of all I would like to thank my supervisor Dr. Shrihari Gopalakrishna for his guidance and constant help throughout the rigorous journey of my Ph.D. He introduced me to the area of beyond the Standard Model physics and collider phenomenology, and is extraordinarily patient in explaining every detail of any physics/non-physics issue. He has always tried to make me as independent as possible in research and I am fortunate to have such a nice and ethical person as my Ph.D. guide.

At the very beginning of my research work, I started working with Dr. Prashanth Jaikumar who joined IMSc as a faculty in the same year as me and our collaboration is still alive although he has moved to USA. He first introduced me to the area of modern research and supervised my Masters thesis on color superconductivity in quark matter. He always encouraged me and motivated me to pursue research in future. I would like to thank my collaborator Dr. Sanatan Digal for many valuable discussions and helping me with some numerical techniques for the projects on color superconductivity.

Late Prof. Rahul Basu, who taught me perturbative QCD calculations and many collider related issues, was my first Ph.D. supervisor. I worked with him till the last day before he was admitted to hospital with severe lung infection and never returned to the Institute again. We started a project on central diffractive production of graviton at the LHC and the paper has been published very recently three years after his death. I dedicate this paper to him and it is a small tribute from me in memory of him.

I would like to thank my long time collaborator, mentor and friend Dr. Subhadip Mitra for innumerous brain-teasing academic discussions and rather brain-refreshing "social" chats via skype at anytime from anywhere or whenever we met face to face. I am also influenced by him on the perspectives of ethical research and his ways of thinking about how to keep yourself stable in a pressurized situation. I would like to convey my thanks to my collaborators Dr. Gregory Moreau and Dr. Rakesh Tibrewala.

I am thankful to Prof. Romesh Kaul for teaching me beautiful courses on quantum field theory. A special thanks goes to my batch-mate Neeraj for teaching me FORTRAN programming and always helping me in writing difficult codes. I would also like to thank the speakers of the Advanced School on Radiative Corrections at SINP and Think Tank on Physics @ LHC at Sariska, from them I learned to use some HEP packages and many collider physics issues.

It has always been an enjoyable experience to spend time with fellow students of IMSc. Thanks to Diganta, Dibya, Tuhin, Soumya, Modak and all HEP students of IMSc for many physics discussions. Thanks to Neeraj, Abhra, Kaju, Jahanur, Prateep, Panchu, Dhriti, Joyjit, Sudhir for many philosophical, social and political discussions. Thanks to Aritra, Upayan, Trisha and our Student Mess Dinning table for always keeping me updated about the scandalous gossips and rumors circulating in the IMSc's air. Thanks to my seniors Sarbeswar, Bireswar, Saptarshi, Amit, Samrat and many others for making my life at IMSc very colorful.

I express my deepest gratitude to my parents, grandmother and my brother for their unconditional love and affection. Without them it would have never been possible for me to become what I am today and to them I owe a debt that can never be repaid. I would like to thank my life-partner and greatest friend Madhumita for being always with me in every situation - tough, happy or normal. I am also thankful to her for bearing with my fluctuating moods and giving me "vocal-tonic" whenever needed. Without her love, support and encouragement I could not have finished this thesis.

Finally I thank IMSc for providing me with financial support and an excellent working environment during the whole period of my Ph.D. work.

My Publications

The thesis is based on the papers marked with "$*$" .

Published

1. **Graviton signals in central production at the LHC.**

   Rahul Basu, Tanumoy Mandal.

   Adv. High Energy Phys., 652714 (2013).

   arXiv:1305.3763 [hep-ph].

2. $*$ **Probing color octet electrons at the LHC.**

   Tanumoy Mandal, Subhadip Mitra.

   Phys. Rev. D **87**, 095008 (2013).

   arXiv:1211.6394 [hep-ph].

3. **Neutrality of a magnetized two-flavor quark superconductor.**

   Tanumoy Mandal, Prashanth Jaikumar.

   Phys. Rev. C **87**, 045208 (2013).

   arXiv:1209.2432 [nucl-th].

4. $*$ **LHC signatures of a vectorlike b'.**

   Shrihari Gopalakrishna, Tanumoy Mandal, Subhadip Mitra, Rakesh Tibrewala.

   Phys. Rev. D **84**, 055001 (2011).

   arXiv:1107.4306 [hep-ph].

On the arXiv

5. $*$ **LHC signatures of warped-space vectorlike quarks.**

   Shrihari Gopalakrishna, Tanumoy Mandal, Subhadip Mitra, Gregory Moreau.

   arXiv:1306.2656 [hep-ph] (Submitted to JHEP).

6. **Chiral and diquark condensates at large magnetic field in two-flavor superconducting quark matter.**

   Tanumoy Mandal, Prashanth Jaikumar, Sanatan Digal.

   arXiv:0912.1413 [nucl-th].

Conference proceedings

7. **Phenomenology of Warped-space Custodian b'.**

   Shrihari Gopalakrishna, Tanumoy Mandal, Subhadip Mitra, Rakesh Tibrewala.

   Pramana **76**, 707 (2011) (Working group report: WHEPP-XI).

Contents

List of Figures

List of Tables

Chapter 1

Introduction

The Standard Model (SM) of particle physics is a very successful theory in describing the interactions among elementary particles. All the experimental results so far indicate that the SM is the correct effective theory of elementary particles for energies below the TeV scale. All the fundamental particles predicted by the SM are confirmed by experiment including most likely the Higgs boson, since recently on the 4th of July 2012, CERN announced the discovery of a new boson of mass around 125 GeV whose properties seem to be consistent with the SM Higgs boson [1, 2]. It will, however, take more data and further analysis to positively confirm this particle as the SM Higgs boson. If it is confirmed to be the SM Higgs, it will complete the experimental verification of the particle spectrum and couplings of the SM. However, despite the spectacular agreement of the SM with experiments, there remain some theoretical shortcomings.

One of the major problems that the SM does not address is the gauge hierarchy problem. The fundamental Planck scale ($\sim 10^{19}$ GeV) is 16 orders of magnitude larger than the scale of electroweak symmetry breaking (EWSB) ($\sim 10^{3}$ GeV). One might assume that no beyond the SM (BSM) physics exists below the Planck scale and the SM is the only theory of particle physics valid all the way upto the Planck scale. However, this assumption can make the SM a very fine-tuned theory in order to keep the Higgs mass light in the presence quantum corrections that lifts the mass to the largest scale in the theory. The Higgs mass, which is not protected by any symmetry in the SM, receives quadratically divergent contributions at the loop level and becomes of the order of the Planck scale, the cutoff scale of the theory. If this fine tuning is to be removed, some new physics has to come in just above the TeV scale. This is one of the main motivations to extend the SM above the TeV scale.

In addition to the gauge hierarchy problem, the SM also leaves unexplained the large hierarchy of fermion masses. For instance, the mass of a top quark ($\approx$ 173 GeV) is 6 orders of magnitude larger than the mass of an electron ($\approx$ 0.5 MeV). However, unlike the Higgs mass, fermion masses are protected by chiral symmetry, and therefore stable under radiative corrections. This flavor hierarchy problem, although less severe than the gauge hierarchy problem, leaves a question, why are the masses of fundamental particles so widely separated? There are some observed facts like the dark matter and baryon asymmetry of the universe strongly that strongly suggest that we may need to go beyond the SM to explain them. There are other motivations too to extend the SM; we observe some puzzling facts common to the quark and lepton sectors of the SM, namely the weak coupling constants of quarks and leptons are the same, three generations with identical $SU(2)_L \otimes U(1)_Y$ gauge structure of quarks and leptons etc. In the last few decades enormous effort has been made to construct and test the bigger theory which will address some of the unanswered questions of the SM. Some well-known examples of these BSM theories are Supersymmetric (SUSY) theories, models with extra spatial dimension, dynamical models of EWSB such as technicolor, little Higgs models, quark-lepton compositeness etc.

In this thesis we restrict ourselves to warped extra dimension (WED) models which provide a beautiful solution to the hierarchy problems, and compositeness models which explain fermion family replication, similarities in the weak interaction of quarks and leptons etc. Many BSM extensions including WED and compositeness models predict the existence of new heavy fermions with masses near the TeV scale. If these new particles exist, they might be detected at colliders and yield direct evidence of new physics. Therefore, it is important to study the phenomenology of these exotic fermions at present day colliders like the LHC. The LHC experiments, ATLAS, CMS and LHCb, are looking for the signatures of some of these new resonances. The main focus of this thesis is to study the LHC phenomenology of two types of such heavy exotic fermions, namely the vectorlike quarks that arise in various warped extra dimensional theories and the color octet electrons which appear in some quark-lepton compositeness models.

All the SM fermions are chiral since their left and right chiralities belong to different representations of the SM gauge group. However, a fermion is defined to be vectorlike if its left and right chiralities belong to conjugate representations of the gauge group of the theory. New chiral sequential forth generation quarks are now excluded [3] by the recent Higgs-data [4,5] and by electroweak precision test (EWPT) [6]. On the other hand, heavy vectorlike quarks which do not receive masses from the Yukawa-like couplings to a Higgs boson are less severely constrained by the recent Higgs-data. So far there is no experimental evidence of the existence of vectorlike quarks, nevertheless they are the key ingredients for many BSM theories. For example, vectorlike quarks appear in extra-dimensional theories where higher excitations of SM quarks are vectorlike, composite Higgs models [7–10], little Higgs models [11–14], some non-minimal supersymmetric extensions [15–17] of the SM etc. In the literature extensive studies on the vectorlike fermions are available. Here we briefly survey some references that are relevant to our study.

Vectorlike fermions in the context of Higgs boson production have been considered in Refs. [18–22]. Based on the recent discovery of a Higgs boson at the LHC [1, 2], Refs. [23, 24] constrain vectorlike fermion masses and couplings from the recent data. It has been pointed out in Refs. [25–28] that vectorlike fermions can address the forward-backward asymmetry in top quark pair production at the Tevatron. Refs. [29–35] analyze vectorlike fermion representations and mixing of the new fermions with the SM quarks and the relevant experimental bounds. Refs. [36–44] study the LHC signatures of vectorlike quarks having electromagnetic (EM) charges -1/3, 2/3, and 5/3, which we denote as b', t' and χ respectively. Ref. [38] studies the LHC signatures of vectorlike b' and χ in the 4-W

channel. Ref. [43] studies multi-b signals for t' quarks at the LHC. The LHC signatures of vectorlike t' and b' decaying to a Higgs boson are discussed in Ref. [42]. Ref. [44] studies pair-production of the vectorlike quarks followed by their decays into single and multi-lepton channels. Pair-production of the Kaluza-Klein (KK) top is explored in Ref. [45]. Ref. [46] studies the signatures of vectorlike quarks resulting from the decay of a KK gluon. Ref. [47] analyzes the single production of t' and b' via KK gluon and finds that these channels could be competitive with the direct electroweak single production channels of these heavy quarks. Model independent LHC searches of vectorlike fermions have been discussed in Refs. [48–51]. Many important pair and single production channels for probing a vectorlike b' at the LHC in the context of a warped extra-dimension were explored in Ref. [52]. Mixing of the SM b-quark with a heavy vectorlike b' and partial decay widths were worked out in Ref. [53]. In Ref. [54], the LHC phenomenology of new heavy chiral quarks with electric charges $-4/3$ and $5/3$ are discussed.

Exploiting same-sign dileptons signal to beat the SM background, Refs. [36, 37] show that the pair-production at the 14 TeV LHC can discover charge $-1/3$ and $5/3$ vectorlike quarks with a mass up to 1 TeV (1.5 TeV) with about 10 fb^{-1} (200 fb^{-1}) integrated luminosity. Ref. [39] considers pair production of charge 5/3 vectorlike quarks and shows that with the search for same sign dilepton the discovery reach of the 7 TeV LHC is about 700 GeV with 5 fb^{-1} integrated luminosity. The LHC signatures of t' vectorlike quarks have been discussed in [40] using $pp \to t'\bar{t}' \to bW^+\bar{b}W^-$ channel with the semileptonic decay of the W's and the reach is found to be about 1 TeV with 100 fb^{-1} integrated luminosity at the 14 TeV LHC. With 14.3 fb^{-1} of integrated luminosity at the 8 TeV LHC, ATLAS has excluded a weak-isospin singlet b' quark with mass below 645 GeV, while for the doublet representation the limit is 725 GeV [55]. In Ref. [56] the ATLAS collaboration shows the exclusion limits for a t' quark in the BR($t' \to Wb$) versus BR($t' \to th$) plane. With 4.64 fb^{-1} luminosity, using single production channels with charged and neutral current interactions, vectorlike b', t' and χ quarks up to masses about 1.1 TeV, 1 TeV and 1.4 TeV respectively have been excluded [57], for couplings taken to be v/M, where

v is the Higgs vacuum expectation value (VEV), and M the mass of the vectorlike quark. With 19.6 fb^{-1} luminosity at the 8 TeV LHC and assuming 100% branching ratio (BR) for the $\chi \to tW$ channel, the CMS collaboration has set their limit on the χ quark mass to 770 GeV [58]. They set limit on t' mass between 687 GeV to 782 GeV for all possible BRs into bW, tZ and th decay modes using 8 TeV LHC data with 19.6 fb^{-1} integrated luminosity [59].

The quark-lepton composite models assume that the SM particles may not be fundamental and just as the proton has constituent quarks, they are actually bound states of substructural constituents (preons) [60]. These constituents are visible only beyond a certain energy scale known as the compositeness scale. A typical consequence of quark-lepton compositeness is the appearance of colored particles with nonzero lepton number (leptogluons, leptoquarks) and exited leptons etc. Some composite models naturally predict the existence of leptogluons (l_8) [60–66] that are color octet fermions with nonzero lepton number. Several studies on the collider searches of leptoquarks, exited fermions can be found in the literature [67–69] but there are only a few similar studies on l_8's. Various signatures of color octet leptons at different colliders were investigated in some earlier papers [70–75]. Recently some important production processes of the l_8 have been analyzed for future colliders like the Large Hadron-electron Collider (LHeC), International Linear Collider (ILC) and the Compact Linear Collider (CLiC) [76, 77]. We briefly review the limits on (charged) color octet leptons available in the literature. The lower mass limit of color octet charged leptons quoted in the latest Particle Data Book [78] is only 86 GeV. This limit is from the twenty three years old Tevatron data [79] from the pair production channel. A mass limit of $M_{l_8} > \mathcal{O}(110)$ GeV from the direct pair production via color interactions has been derived from $p\bar{p}$ collider data in [80]. Lower limits on the leptogluons masses were derived by JADE collaboration from the t-channel contribution to the total hadronic cross section in the M_{l_8} vs Λ plane, $M_{l_8}\Lambda^2 \gtrsim (150\text{ GeV})^3$ (where Λ is the compositeness scale) and from direct production via one photon exchange, $M_{l_8} \gtrsim 20$ GeV [81]. In Ref. [82], the compositeness scale $\Lambda \lesssim 1.8$ TeV was excluded at

95% confidence level (CL) for $M_{l_8} \simeq 100$ GeV and $\Lambda \lesssim 200$ GeV for $M_{l_8} \simeq 200$ GeV. It is also mentioned in Ref. [74] that the D0 cross section bounds on $eejj$ events exclude leptogluons mass up to 200 GeV and could naively place the constraint $M_{l_8} \gtrsim 325$ GeV.

The outline of the thesis is as follows: In Chapter 2 we review the warped-space extra dimensional model that has been proposed by Randall-Sundrum (RS) as a solution to the gauge hierarchy problem of the SM [83]. The fermion mass hierarchy of the SM can also be addressed by allowing SM fields to propagate in the bulk without badly violating flavor changing neutral current (FCNC) constraints [84, 85]. In Chapter 3 we give details of the parameter choices we make in the warped models and show the vectorlike fermion couplings and their dependence on the bulk mass parameters. In the same chapter we also give the partial decay widths and the branching ratios into the various decay modes for various warped-space models. In Chapter 4 we discuss some promising discovery channels for the vectorlike quarks having electromagnetic (EM) charges -1/3, 2/3, and 5/3, which we denote as b', t' and χ respectively. We also present the discovery reach of these new quarks for the 8 and 14 TeV LHC. Chapter 5 of the thesis deals with color octet electrons. We point out that composite models are proposed to answer some questions in the SM such as quark-lepton symmetry, family replications etc. A typical consequence of quark-lepton compositeness is the appearance of colored particles with nonzero lepton number (leptogluons, leptoquarks) and exited leptons etc. In this thesis we discuss the LHC phenomenology of color octet electron and present the discovery reach for the 14 TeV LHC.

Chapter 2

Warped models

During the last decade the Randall-Sundrum (RS) model [83] and its variants have attracted a lot of attention, both theoretically and phenomenologically as this model solves the gauge hierarchy problem in a very elegant manner. In Sec. 2.1 we briefly review the construction of the RS model, including the derivation of the warped metric as a solution to the Einstein's equations [83]. Then we show how this model solves the gauge hierarchy problem of the SM. After this, we present a short discussion on the bulk gauge and fermion fields coupled with an IR-brane localized Higgs field. In Sec. 2.2 we give the details of the warped models both without and with custodial protection of the $Z\bar{b}_L b_L$ coupling. We discuss the gauge sector and different quark representations of these models, and write various Lagrangian terms in the mass basis relevant to the phenomenology we discuss in the subsequent chapters.

2.1 Original RS model

Following Ref. [83], in this section we briefly review the construction of the RS model and present the derivation of the warped metric as a solution to the Einstein's equations. We consider a five dimensional spacetime with one extra spatial dimension y compactified on an orbifold $S^1/\mathbb{Z}_2$, where S^1 denotes a circle with compactification radius R and $\mathbb{Z}_2$ is a parity symmetry. In other words the fifth dimension y is periodic with a period $2\pi R$ and (x^μ, y) is identified with $(x^\mu, -y)$, where x^μ denote the 4D Minkowskian coordinates. Thus, the y coordinate is bounded in the interval $0 \le y \le \pi R$. The boundaries of this interval are called 3-branes. The branes at $y = 0$ and $y = \pi R$ are called the Ultraviolet (UV) or the Planck brane and the Infrared (IR) or the TeV brane respectively. The region between the UV brane and the IR brane (*i.e.* $0 < y < \pi R$) is called the bulk. The classical action for this setup can be split into three parts as follows

$$\mathcal{S} = \mathcal{S}_{bulk} + \mathcal{S}_{UV} + \mathcal{S}_{IR} \ , \tag{2.1}$$

where $\mathcal{S}_{bulk}$, $\mathcal{S}_{UV}$ and $\mathcal{S}_{IR}$ represent the actions for the bulk, the UV brane and the IR brane respectively, and they read as

$$\mathcal{S}_{bulk} = \int d^4x \int_0^{\pi R} dy \sqrt{-G} \left(-\Lambda + 2M^3 \mathcal{R}\right) \tag{2.2}$$

$$\mathcal{S}_{UV} = \int d^4x \sqrt{-G} \left(\mathcal{L}_{UV} - V_{UV}\right) \delta(y) \tag{2.3}$$

$$\mathcal{S}_{IR} = \int d^4x \sqrt{-G} \left(\mathcal{L}_{IR} - V_{IR}\right) \delta(y - \pi R) \ , \tag{2.4}$$

where G is the determinant of the 5D metric $G_{MN}(x^\mu, y)$ (where $M, N = 0, \ldots, 4$), Λ is the 5D cosmological constant, M is the 5D fundamental scale of gravity and $\mathcal{R}$ is the 5D Ricci scalar. In Eqs. (2.3) and (2.4), the 4D vacuum energy V_{UV} and V_{IR} act as gravitational sources even in the absence of particle excitations. Our strategy is to derive the background metric in absence of any particle excitation and then to add matter fields as perturbations on the background metric. Thus, we set $\mathcal{L}_{UV}, \mathcal{L}_{IR} = 0$ and write the 5D Einstein's equations for the action $\mathcal{S}$ as follows

$$\sqrt{-G} \left(\mathcal{R}_{MN} - \frac{1}{2} G_{MN} \mathcal{R}\right) = -\frac{1}{4M^3} \sqrt{-G} G_{MN} \left[\Lambda + V_{IR} \delta(y - \pi R) + V_{UV} \delta(y)\right] \ , \tag{2.5}$$

where $\mathcal{R}_{MN}$ is the 5D Ricci tensor. We assume that there exists a solution of Eq. (2.5) that respects 4D Poincare invariance in the x^μ directions. The general form of the 5D metric which satisfy this ansatz can be written as

$$ds^2 = e^{-2\sigma(y)}\eta_{\mu\nu}dx^\mu dx^\nu - dy^2 \ , \tag{2.6}$$

where $\eta_{\mu\nu} = \mathrm{diag}(1, -1, -1, -1)$ is the 4D Minkowskian metric. Our aim is to find out the unknown function $\sigma(y)$ appearing in Eq. (2.6). Using the metric in Eq. (2.6), the Einstein's equations shown in Eq. (2.5) reduce to two differential equations as follows

$$\frac{d\sigma}{dy} = \sqrt{\frac{-\Lambda}{24M^3}} \ ; \qquad \frac{d^2\sigma}{dy^2} = \frac{1}{12M^3R}\left[V_{UV}\delta(y) + V_{IR}\delta(y - \pi R)\right] \ . \tag{2.7}$$

The solution to the first order differential equation above consistent with the orbifold symmetry is

$$\sigma = |y|\sqrt{\frac{-\Lambda}{24M^3}} \ . \tag{2.8}$$

Since the metric is a periodic function in y, using Eq. (2.8) we calculate σ'' as follows

$$\frac{d^2\sigma}{dy^2} = \frac{2}{R}\sqrt{\frac{-\Lambda}{24M^3}}\left[\delta(y) - \delta(y - \pi R)\right] \ . \tag{2.9}$$

Comparing σ'' in Eq. (2.7) and Eq. (2.9), we find that a solution of Eq. (2.7) exists only if V_{UV}, V_{IR} and Λ are related in terms of a single scale k as

$$V_{UV} = -V_{IR} = 24M^3k \ ; \qquad \Lambda = -24M^3k^2 \ . \tag{2.10}$$

Thus, the form of the 5D metric as a solution to the 5D Einstein's equations for the RS warped geometry is given by

$$ds^2 = e^{-2ky}\eta_{\mu\nu}dx^\mu dx^\nu - dy^2 \ . \tag{2.11}$$

We note that the above solution is valid only if $\Lambda \leq 0$. The case $\Lambda = 0$ gives the flat extra dimension, while for the $\Lambda < 0$ case, the 5D bulk is a slice of 5D Anti-de-Sitter space (AdS_5). Due to the non-vanishing negative 5D cosmological constant, the extra dimension has a finite curvature and the factor e^{-2ky} in the metric describes the warped nature of the theory. But a slice of AdS_5 space at a fixed value of y the metric becomes flat and respects 4D Poincare invariance.

2.1.1 Solution to the hierarchy problem

Here we discuss how the RS geometry solves the gauge hierarchy problem. One can obtain a 4D effective theory by integrating over the extra dimension y. Using the 5D metric in Eq. (2.11) in the 5D action $\mathcal{S}$, we obtain the 4D action corresponding to the 4D curvature term as

$$\mathcal{S}_{4D} \supset \int d^4x \int_0^{\pi R} dy \; 2M^3 e^{-2ky} \sqrt{-\bar{g}}\bar{\mathcal{R}} \; , \tag{2.12}$$

where $\bar{\mathcal{R}}$ is the 4D Ricci scalar constructed from the 4D metric $\bar{g}_{\mu\nu}$ which has the form

$$\bar{g}_{\mu\nu}(x) = \eta_{\mu\nu} + h_{\mu\nu}(x) \; . \tag{2.13}$$

The $h_{\mu\nu}(x)$ describes local gravitational fluctuations on the background metric $\eta_{\mu\nu}$. From Eq. (2.12) one can relate the 4D effective Planck scale of gravity M_{Pl} to the 5D gravity scale M as

$$M_{Pl}^2 = \frac{M^3}{k}\left(1 - e^{-2k\pi R}\right) \approx \frac{M^3}{k} \quad (\text{since} \;\; e^{-2k\pi R} \ll 1) \; . \tag{2.14}$$

Now we move to a situation where $\mathcal{L}_{IR} \neq 0$ and consider a fundamental scalar field H on the IR brane with a vacuum expectation value (VEV) $\langle H \rangle = v_0$. The 4D action for this case is

$$S_{4D} \supset \int d^4x \, \sqrt{-g_{IR}} \left\{ g_{IR}^{\mu\nu} \partial_\mu H^\dagger \partial_\nu H - \lambda (H^\dagger H - v_0^2)^2 \right\} \ , \tag{2.15}$$

where $g_{IR}^{\mu\nu} = e^{2k\pi R}\eta^{\mu\nu}$ and $g_{IR} = \det(g_{IR}^{\mu\nu}) = -e^{-8k\pi R}$. We absorb a factor $e^{-k\pi R}$ in the definition of H to canonically normalize it and by replacing $H \to e^{k\pi R}H$ we obtain

$$S_{4D} \supset \int d^4x \ \left\{ \eta^{\mu\nu} \partial_\mu H^\dagger \partial_\nu H - \lambda (H^\dagger H - e^{-2k\pi R} v_0^2)^2 \right\} \ . \tag{2.16}$$

In the above equation, we observe that the fundamental Higgs VEV is rescaled by a warp factor and the effective symmetry breaking scale v is given by $v = e^{-k\pi R} v_0$. According to the naturalness principle, we assume that all the fundamental parameters are of same order *i.e.* $M, k, v_0 \sim \mathcal{O}(M_{pl})$. Thus, there is no large hierarchy present between the fundamental parameters. But we can derive a scale $v \sim \mathcal{O}(\text{TeV})$ by choosing $k\pi R \sim 35$, the scale of EWSB from the Planck scale. Therefore, the RS model offers an intriguing solution to the gauge hierarchy problem by reducing the large hierarchy between the Planck scale and the scale of EWSB. This concludes the review of the original Randall-Sundrum model [83].

2.1.2 SM fields in the Bulk

In the original RS model only gravity can propagate into the bulk. While all the SM fields are assumed to be confined on the TeV brane. The solution to the gauge hierarchy problem will not be spoiled if we allow gauge and matter fields to propagate into the extra dimension [84–88]. In addition to the gauge hierarchy problem, the fermion mass hierarchy problem of the SM can also be addressed by allowing SM fermions to propagate in the bulk [84,85]. We consider a scenario where gauge and fermion fields are allowed to propagate in the bulk while the Higgs field is confined on the IR brane. Here we mainly follow notations of Ref. [85]. Setting all interaction terms to zero, the free field action for gauge and fermion fields is given by

$$\mathcal{S} = \int d^4x \int_0^{\pi R} dy \sqrt{-G} \left[-\frac{1}{4} F_{MN} F^{MN} + \frac{1}{2} \bar{\psi} \left(i\Gamma^M (\partial_M + \omega_M) - ck \right) \psi \right] + \text{H.}c. \; , \tag{2.17}$$

where $F_{MN} = \partial_M A_N - \partial_N A_M$ is the field strength tensor of the 5D gauge field A_M. The 5D Dirac matrices and spin connections in curved spacetime is denoted by Γ_M and ω_M respectively. The bulk mass of the 5D fermion ψ is $m = ck$ where c is the bulk mass parameter. We obtain the equation of motions (EOM) for the gauge and the fermion fields using the variational principle $\delta\mathcal{S} = 0$ which yields

$$\left[-e^{2ky} \eta^{\mu\nu} \partial_\mu \partial_\nu + e^{s_\Phi ky} \partial_5 (e^{-s_\Phi ky} \partial_5) - M_\Phi^2 \right] \Phi(x^\mu, y) = 0 \; , \tag{2.18}$$

where $\Phi = \{A_M, e^{-2ky}\psi_{L,R}\}$. Fermion field is scaled by a factor e^{-2ky} as required for proper normalization and L, R represent the Lorentz chiralities. In case of gauge fields, $s_A = 2$ and $M_A^2 = 0$ with the gauge choice $\partial_\mu A^\mu = 0$ and $A_5 = 0$. In case of fermions, $s_\psi = 1$ and $M^2_{\psi_{L,R}} = c(c \pm 1)k^2$. In order to solve the EOM in Eq. (2.18), we decompose 5D gauge and fermion fields in a complete set $f_\Phi^{(n)}$ as follows

$$A_\mu(x^\mu, y) = \frac{1}{\sqrt{\pi R}} \sum_{n=0}^{\infty} A_\mu^{(n)}(x^\mu) f_A^{(n)}(y) \tag{2.19}$$

$$\psi_{L,R}(x^\mu, y) = \frac{e^{2ky}}{\sqrt{\pi R}} \sum_{n=0}^{\infty} \psi_{L,R}^{(n)}(x^\mu) f_{\psi_{L,R}}^{(n)}(y) \; . \tag{2.20}$$

This decomposition is called Kaluza-Klein (KK) decomposition. The infinite sums appearing in the decompositions correspond to a tower of 4D KK states and each KK state is associated with a profile f along the y direction. Using the KK decomposition of Φ in Eq. (2.18) we find that f satisfy the following equation

$$\left[\partial_y^2 - s_\Phi k \partial_y - \left(M_\Phi^2 - e^{2ky} m_n^2 \right) \right] f_\Phi^{(n)}(y) = 0 \; , \tag{2.21}$$

where m_n is the mass of the n-th KK mode satisfying the relation $\eta^{\mu\nu}\partial_\mu\partial_\nu\Phi^{(n)}(x^\mu) = m_n^2\Phi^{(n)}(x^\mu)$ relation. Eq. (2.21) is a second order differential equation which can be solved by specifying two boundary conditions (BCs) at the boundaries $y = 0$ and $y = \pi R$. Here we consider two types of BCs,

- Dirichlet $(-)$ BC: The field $\Phi(x^\mu, y)$ or equivalently $f_\Phi^{(n)}(y)$vanishes on the brane.
- Neumann $(+)$ BC: The derivative of the field $\partial_y\Phi(x^\mu, y)$ vanishes on the brane.

By properly choosing the BCs for the field content of the theory, one can construct phenomenologically interesting models in agreement with the current experimental constraints. Now we discuss the solution of the EOM for the bulk gauge and fermion fields.

Gauge fields in the bulk

Solving the EOM for the gauge field using the KK decomposition given in Eq. (2.19) we obtain the bulk gauge boson profiles as [85]

$$f_A^{(0)}(y) = 1; \quad f_A^{(n)}(y) = \frac{e^{ky/2}}{N_n}\left[J_1\left(\frac{m_n}{k}e^{ky}\right) + b_1(m_n)Y_1\left(\frac{m_n}{k}e^{ky}\right)\right] \ , \tag{2.22}$$

where $n = 1, 2, \ldots$ labels the n-th KK mode. The $J_1(x)$ and $Y_1(x)$ are the Bessel functions of order one of the first and the second kind respectively. We note that the zero mode profile $f_A^{(0)}(y)$ for a massless gauge field is flat (*i.e.* not dependent on y) whereas the higher KK profiles $f_A^{(n)}(y)$ are exponentially peaked towards the TeV brane. The flat zero mode, $f_A^{(0)}(y) = 1$ exists only for $(+,+)$ BCs. Here the signs in the braket indicate the BCs for each field on the UV and IR brane respectively. These profiles satisfy the following orthonormality conditions,

$$\frac{1}{\pi R}\int_0^{\pi R} dy f^{(m)}(y) f^{(n)}(y) = \delta_{mn} \ , \tag{2.23}$$

from which one can determine the normalization N_n. The KK mass m_n and the coefficient $b_1(m_n)$ depend on the choice of the BCs on the branes. Here we consider gauge fields with $(+,+)$ and $(-,+)$ BCs.

- For $(+,+)$ BCs, *i.e.* $\partial_y f_A^{(n)}(y)|_{y=0,\pi R} = 0$:

$$b_1(m_n) = -\frac{J_1\left(\frac{m_n}{k}\right) + \left(\frac{m_n}{k}\right) J_1'\left(\frac{m_n}{k}\right)}{Y_1\left(\frac{m_n}{k}\right) + \left(\frac{m_n}{k}\right) Y_1'\left(\frac{m_n}{k}\right)} = b_1(m_n e^{k\pi R}) \;, \tag{2.24}$$

which can be solved numerically for m_n and $b_1(m_n)$. For instance, solving Eq. (2.24) numerically for the first KK mode with $(+,+)$ BCs we find $m_1^{(+,+)} \approx 2.45 k e^{-k\pi R}$.

- For $(-,+)$ BCs, *i.e.* $f_A^{(n)}(y)|_0 = 0$ and $\partial_y f_A^{(n)}(y)|_{\pi R} = 0$:

$$b_1(m_n) = \frac{J_1\left(\frac{m_n}{k}\right)}{Y_1\left(\frac{m_n}{k}\right)} = -\frac{J_1\left(\frac{m_n}{k}e^{k\pi R}\right) + \left(\frac{m_n}{k}e^{k\pi R}\right) J_1'\left(\frac{m_n}{k}e^{k\pi R}\right)}{Y_1\left(\frac{m_n}{k}e^{k\pi R}\right) + \left(\frac{m_n}{k}e^{k\pi R}\right) Y_1'\left(\frac{m_n}{k}e^{k\pi R}\right)} \;, \tag{2.25}$$

Solving the above equation numerically we find that the first KK gauge boson mass with $(-,+)$ BCs is $m_1^{(-,+)} \approx 2.40 k e^{-k\pi R}$.

We note that $m_1^{(-,+)} < m_1^{(+,+)}$ and we define $M_{KK} = m_1^{(+,+)}$ *i.e.* the mass of the lowest gauge KK excitation.

Fermion fields in the bulk

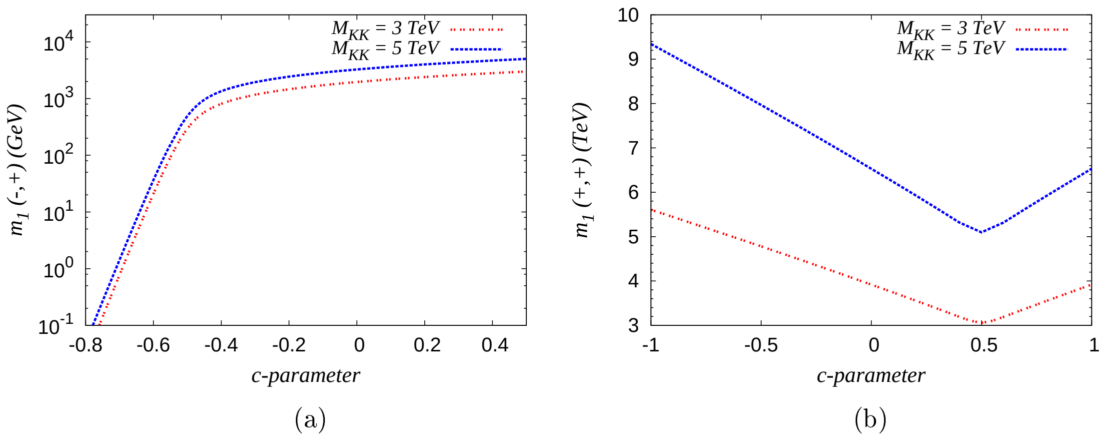

Figure 2.1: Masses of the first KK fermion with $(-,+)$ (*left*) and $(+,+)$ (*right*) BCs as functions of c-parameter for $M_{KK} = 3$ and 5 TeV.

Solving the EOM for the fermion field using the KK decomposition given in Eq. (2.20) we obtain the bulk profiles for left-handed fermion as [85]

$$f^{(0)}_{\Psi_L}(y) = \sqrt{\frac{(1-2c)k\pi R}{e^{(1-2c)k\pi R}-1}}\,e^{-cky} \tag{2.26}$$

$$f^{(n)}_{\Psi_L}(y) = \frac{e^{ky/2}}{N_n}\left[J_\alpha\left(\frac{m_n}{k}e^{ky}\right) + b_\alpha(m_n)Y_\alpha\left(\frac{m_n}{k}e^{ky}\right)\right] \ , \tag{2.27}$$

where $n = 1, 2, \ldots$ labels the n-th KK mode and $\alpha = |c + 1/2|$. The special functions J_α and Y_α are the Bessel functions of order α of the first and the second kind respectively. We note that a massless zero mode $f^{(0)}_{\Psi_L}(y)$ exists only for $(+,+)$ BCs. The profiles for the right-handed modes can be obtained by replacing c by $-c$ in the above formulae. We also note that the left-handed zero mode $f^{(0)}_{\Psi_L}(y)$ is flat for $c = 1/2$, peaked towards the UV brane for $c > 1/2$ and peaked towards the IR brane for $c < 1/2$. The fermionic profiles satisfy the following orthonormality conditions,

$$\frac{1}{\pi R}\int_0^{\pi R} dy\ e^{ky} f^{(m)}(y) f^{(n)}(y) = \delta_{mn} \ , \tag{2.28}$$

from which one can determine the normalization, N_n. The coefficient $b_\alpha(m_n)$ and KK mass m_n are determined through the BCs on the branes.

- For fermions obeying $(-,+)$ BCs, *i.e.* $f^{(n)}(y)|_{y=0} = 0$ and $(\partial_y + ck)f^{(n)}(y)|_{y=\pi R} = 0$, we obtain

$$b_\alpha(m_n) = -\frac{J_\alpha\left(\frac{m_n}{k}\right)}{Y_\alpha\left(\frac{m_n}{k}\right)} = -\frac{\left(c+\frac{1}{2}\right)J_\alpha\left(\frac{m_n}{k}e^{\pi kR}\right) + \left(\frac{m_n}{k}e^{\pi kR}\right)J'_\alpha\left(\frac{m_n}{k}e^{\pi kR}\right)}{\left(c+\frac{1}{2}\right)Y_\alpha\left(\frac{m_n}{k}e^{\pi kR}\right) + \left(\frac{m_n}{k}e^{\pi kR}\right)Y'_\alpha\left(\frac{m_n}{k}e^{\pi kR}\right)} \tag{2.29}$$

  This condition can be solved numerically for m_n and $b_\alpha(m_n)$. The first fermion KK mass m_1 with $(-,+)$ BC as functions of the bulk mass parameter c for $M_{KK} = 3$ and 5 TeV is shown in Fig. 2.1(a).

- For fermions obeying $(+,+)$ BCs, *i.e.* $(\partial_y + ck)f^{(n)}(y)|_{y=0,\pi R} = 0$, we obtain

$$b_\alpha(m_n) = -\frac{\left(c+\frac{1}{2}\right)J_\alpha\left(\frac{m_n}{k}\right) + \left(\frac{m_n}{k}\right)J'_\alpha\left(\frac{m_n}{k}\right)}{\left(c+\frac{1}{2}\right)Y_\alpha\left(\frac{m_n}{k}\right) + \left(\frac{m_n}{k}\right)Y'_\alpha\left(\frac{m_n}{k}\right)} = b_\alpha(m_n e^{\pi kR}) \tag{2.30}$$

This condition can be solved numerically for m_n and $b_\alpha(m_n)$. The first fermion KK mass m_1 with $(+,+)$ BCs as functions of the bulk mass parameter c for $M_{KK} = 3$ and 5 TeV is shown in Fig. 2.1(b).

In Fig. 2.1(a) we see that the m_1 for $(-,+)$ BCs can be significantly smaller in some c-parameter range and the LHC signatures of $(-,+)$ fermions might be very promising. Therefore, in this thesis our main aim is to study the LHC signatures of $(-,+)$ fermions.

2.2 Custodially Protected RS Model

In the previous section we reviewed the warped-space extra dimensional model that has been proposed by Randall-Sundrum (RS) as a solution to the gauge hierarchy problem of the SM [83]. The RS model is a theory defined on a slice of AdS_5 space. Due to the AdS/CFT correspondence [89] certain strongly coupled 4D theories can be interpreted as weakly coupled 5D theories in the AdS_5 background. Therefore, it is possible to calculate some observables perturbatively in the framework of the RS model. The fermion mass hierarchy of the SM can also be addressed by allowing SM fields to propagate in the bulk without badly spoiling electroweak precision test constraints [84, 85]. In particular the most stringent constraints come from the measurements of the Peskin-Takeuchi parameters [90] and the $Z\bar{b}_L b_L$ coupling. The Peskin-Takeuchi parameters are a set of three measurable quantities, called S, T, and U, which are very sensitive to the new physics contributions to the electroweak radiative corrections. They are parametrized as

$$S = \frac{4s_w^2c_w^2}{\alpha(M_Z)}\left[\Pi'_{ZZ}(0) - \frac{c_w^2-s_w^2}{s_wc_w}\Pi'_{Z\gamma}(0) - \Pi'_{\gamma\gamma}(0)\right] \tag{2.31}$$

$$T = \frac{1}{\alpha(M_Z)}\left[\frac{\Pi_{WW}(0)}{M_W^2} - \frac{\Pi_{ZZ}(0)}{M_Z^2}\right] \tag{2.32}$$

$$U = \frac{4s_w^2}{\alpha(M_Z)}\left[\Pi'_{WW}(0) - c_w^2\Pi'_{ZZ}(0) - 2s_wc_w\Pi'_{Z\gamma}(0) - s_w^2\Pi'_{\gamma\gamma}(0)\right] \tag{2.33}$$

where $\alpha(M_Z)$ is the fine structure constant measured at the scale M_Z. Here Π_{VV} denotes the vacuum polarization functions of the gauge boson V measured at the scale $q^2 = 0$

and the Π'_{VV} is the derivative of Π_{VV} with respect to q^2. The s_w and c_w are the sine and cosine of the weak mixing angle respectively. The Peskin-Takeuchi parameters are defined in such a way that they are all equal to zero at a reference point in the Standard Model, with a particular value chosen for the Higgs boson mass. Usually U is small in typical BSM theories. Assuming $U = 0$ and $M_h = 125$ GeV, a combined analysis of electroweak precision measurements leads to the constraint, $S = 0.04 \pm 0.09$ [78]. The T parameter is a measure of the violation of the custodial symmetry in the electroweak sector and very sensitive to the new physics effects (S parameter is also sensitive). The LEP data put very stringent bound on the T parameter, $T = 0.07 \pm 0.08$ [78]. Another EWPT observable which is very precisely measured is the $Z\bar{b}_L b_L$ coupling and in the SM it reads

$$\kappa_{Zb_Lb_L} = g_Z \left[-\frac{1}{2} + \frac{1}{3}\sin^2\theta_W \right] \, . \tag{2.34}$$

Experimentally the bound on the shift of the $Z\bar{b}_L b_L$ coupling from the SM value, $\Delta\kappa_{Zb_Lb_L}$ with 95% C.L. is given by [78]

$$-2 \times 10^{-3} \lesssim \Delta\kappa_{Zb_Lb_L} \lesssim 6 \times 10^{-3} \, . \tag{2.35}$$

In a simple extension of the RS model with SM fields in the bulk and the bulk gauge group being the SM gauge group $SU(2)_L \otimes U(1)_Y$, the mass of the lowest KK excitation of the gauge boson, M_{KK} is constrained by electroweak precision tests (in particular the T parameter) to be above 8 TeV [91]. Therefore, this simple extension will likely remain beyond the reach of the LHC. However, as shown in Ref. [91] this situation can be significantly improved by extending the bulk gauge group to $\mathcal{G} = SU(2)_L \otimes SU(2)_R \otimes U(1)_X$. The custodial symmetry in the Higgs sector offers an $SU(2)_R$ symmetry in the bulk [91] and protects the T-parameter from receiving large tree level corrections. In this scenario the limit relaxes to $M_{KK} \gtrsim 2 - 3$ TeV which could be discovered at the LHC. However, this scenario is still strongly constrained due to a large shift to the $Z\bar{b}_L b_L$ coupling. As shown in Ref. [92] the correction to the $Z\bar{b}_L b_L$ coupling can be kept under control by embedding the third generation quarks (t_L and b_L) into the bidoublet representation (*i.e.* $(\mathbf{2},\mathbf{2})_{2/3}$) of $\mathcal{G}$ together with an extra discrete $\mathbb{Z}_2$ ($SU(2)_L \leftrightarrow SU(2)_R$) symmetry of the theory.

Next we give the particle content of the warped model with bulk gauge group $\mathcal{G}$ and work out various Lagrangian terms in the mass basis. For the quark content of the theory we present various quark representations in models both without and with the custodial protection of the $Z\bar{b}_L b_L$ coupling.

2.2.1 Gauge sector

The bulk gauge group of the custodially protected RS model is larger and therefore, the particle content in this model is larger than the SM particle content. Here, we list all the gauge bosons associated with the bulk gauge group $SU(3)_c \otimes SU(2)_L \otimes SU(2)_R \otimes U(1)_X$, and the corresponding gauge couplings.

- $SU(3)_c$ gauge bosons are G^A_μ ($A = 1, \cdots, 8$) and the gauge coupling is g_S.
- $SU(2)_L$ gauge bosons are $W^1_{L\mu}$, $W^2_{L\mu}$, $W^3_{L\mu}$ and the gauge coupling is g_L.
- $SU(2)_R$ gauge bosons are $W^1_{R\mu}$, $W^2_{R\mu}$, $W^3_{R\mu}$ and the gauge coupling is g_R.
- $U(1)_X$ gauge bosons is X_μ and the gauge coupling is g_X.

To obtain the correct low energy spectrum, the bulk gauge group of the custodially protected RS model can be broken by an appropriate choice of BCs on the UV brane to the SM gauge group, and the SM gauge group is finally broken to $U(1)_{EM}$ by a nonzero Higgs VEV as in the SM [91]. Since $SU(3)_c$ is not broken, we do not always show $SU(3)_c$ explicitly. In short, the breaking pattern can be shown as

$$SU(2)_L \otimes SU(2)_R \otimes U(1)_X \xrightarrow{\text{UV brane}} SU(2)_L \otimes U(1)_Y \xrightarrow{\langle H\rangle} U(1)_{EM} \tag{2.36}$$

The symmetry breaking is achieved by the following assignment of BCs

$$W^a_{L\mu}(+,+), \quad B_\mu(+,+), \quad W^b_{R\mu}(-,+), \quad Z_{X\mu}(-,+) \ , \tag{2.37}$$

where $a = 1, 2, 3$ and $b = 1, 2$. The field Z_X and B are the linear combinations of W^3_R and X as follows

$$Z_{X\mu} = \cos\phi W^3_{R\mu} - \sin\phi X_\mu, \quad B_\mu = \sin\phi W^3_{R\mu} + \cos\phi X_\mu \tag{2.38}$$

where $\tan\phi = g_X/g_R$. At this point, W^a_L and B have massless zero modes before EWSB in their KK decompositions. We define $W^\pm_{L,R}$, Z and A as follows

$$W^\pm_{L\,\mu} = \frac{1}{\sqrt{2}}\left(W^1_{L\mu} \mp W^2_{L\mu}\right), \quad W^\pm_{R\,\mu} = \frac{1}{\sqrt{2}}\left(W^1_{R\mu} \mp W^2_{R\mu}\right) \tag{2.39}$$

$$Z_\mu = \cos\psi W^3_{L\mu} - \sin\psi B_\mu, \quad A_\mu = \sin\psi W^3_{L\mu} + \cos\psi B_\mu \tag{2.40}$$

where $\tan\psi = g_X/\sqrt{g_R^2 + g_X^2}$. It is important to note that the angle ψ is analogues to the weak mixing angle θ_W in the SM. Because of mixing between the gauge boson zero modes and heavy KK modes, ψ and θ_W are slightly different from each other.

2.2.2 Model without $Z\bar{b}_L b_L$ protection

To discuss fermion content of the theory, we present various quark representations which are phenomenologically interesting. We begin our analysis following Ref. [91] with the simplest quark representations (although the $Z\bar{b}_L b_L$ coupling is not protected in this case) where the third generation quarks transform under $\mathcal{G}$ as

$$Q_L \equiv (\mathbf{2},\mathbf{1})_{\frac{1}{6}} = \begin{pmatrix} t_L^{(++)} \\ b_L^{(++)} \end{pmatrix} ; \ Q_{t_R} \equiv (\mathbf{1},\mathbf{2})_{\frac{1}{6}} = \begin{pmatrix} t_R^{(++)} \\ b'^{(-+)} \end{pmatrix} ; \ Q_{b_R} \equiv (\mathbf{1},\mathbf{2})_{\frac{1}{6}} = \begin{pmatrix} t'^{(-+)} \\ b_R^{(++)} \end{pmatrix} . \tag{2.41}$$

Here we consider only the third generation quarks because the couplings of the third generation quarks with the Higgs are significantly bigger than the first two generations. Since they are localized closer to the Higgs profile (*i.e.* closer to the IR brane) as compared to the first two generations. Thus, the mixing effects of higher KK modes through the Higgs VEV on the third generation quarks can be important [93]. We use the notation for the field representations as $(\mathbf{l}, \mathbf{r})_X$ where $\mathbf{l}$ and $\mathbf{r}$ denote $SU(2)_L$ and $SU(2)_R$ representations respectively, and X denotes the $U(1)_X$ charge. The signs in the braket associated with each field indicate the BCs for each field on the UV and IR brane respectively. The "$+$" denotes a Neumann BC and "$-$" stands for a Dirichlet BC. The fields with $(+,+)$ BCs on the extra dimensional interval $[0, \pi R]$ have zero modes and these zero modes are identified with the SM fields, while the new fields t' and b' (the "custodians") have no zero modes by applying $(-,+)$ BCs. All the zero-modes (*i.e.* SM fields) are chiral, while all the higher KK excitations are vectorlike with respect to the SM gauge group.

The Higgs field which is responsible for the EWSB transforms as bidoublet under $\mathcal{G}$,

$$\Sigma \equiv (\mathbf{2}, \mathbf{2})_0 = \begin{pmatrix} \phi_0^* & \phi^+ \\ -\phi^- & \phi^0 \end{pmatrix} , \tag{2.42}$$

where ϕ_0 denotes the physical Higgs boson whose VEV eventually leads to EWSB, $\phi^\pm$ and ϕ_0^* denote the Goldstone bosons which are the longitudinal polarization of the gauge bosons $W^\pm$ and Z respectively after EWSB. The electroweak symmetry is broken by a nonzero VEV $\langle\Sigma\rangle = \mathrm{diag}(v, v)/\sqrt{2}$ (where v is the Higgs boson VEV, $v \approx 246$ GeV). Throughout this thesis we work in the unitary gauge in which the Goldstone bosons are the longitudinal polarizations of the gauge bosons.

To reproduce the large top mass requires that the localization of the Q_{t_R} near the IR brane as we cannot take the Q_L to be too close to the IR brane due to large corrections to the b couplings [94]. Thus, the b' which belongs to the Q_{t_R} is most likely the lightest KK excitation and the $b \leftrightarrow b'$ mixing is large due to the large off-diagonal term in the mixing matrix. Therefore, the b' promises to have the best observability at the LHC, and we will only study its phenomenology for the model without $Z\bar{b}_L b_L$ protection.

Lagrangian

We want to write down the 4D effective couplings of quarks shown in Eq. (2.41) with the SM gauge bosons and Higgs. One can write down an equivalent 4D theory starting from a 5D theory by using KK reduction in which one performs a KK expansion of the fields and then integrate over the extra dimension. The EWSB makes some zero modes massive like in the SM, and mixes various KK modes. After diagonalization of the various mass matrices the lightest eigenmodes of each mass matrix are identified with the SM states.

The kinetic energy (K.E.) terms for the quark multiplets defined in Eq. (2.41) are given by

$$\mathcal{L}_{KE} \supset \bar{Q}_L i\gamma^\mu D_\mu Q_L + \bar{Q}_{t_R} i\gamma^\mu D_\mu Q_{t_R} + \bar{Q}_{b_R} i\gamma^\mu D_\mu Q_{b_R} \ , \tag{2.43}$$

where D_μ is the covariant derivative for the SM gauge group $SU(3)_c \otimes SU(2)_L \otimes U(1)_Y$ written in the mass basis of the gauge bosons after EWSB as follows

$$D_\mu = \partial_\mu - ig_S T^\alpha G^\alpha_\mu - ieQA_\mu - i\frac{g_W}{\sqrt{2}}\left(T^+ W^+_\mu + T^- W^-_\mu\right) - ig_Z\left(T^3 - s^2_W Q\right) Z_\mu \ . \tag{2.44}$$

The K.E. term of the Lagrangian $\mathcal{L}_{KE}$ expressed in the mass basis of gauge boson is

$$\begin{aligned}\mathcal{L}_{KE} \supset & \sum_q \left(eQ_q \bar{q}\gamma^\mu q A_\mu + g_S \bar{q}\gamma^\mu T^\alpha q G^\alpha_\mu\right) + \frac{g_W}{\sqrt{2}}\left[\bar{t}_L \gamma^\mu b_L W^+_\mu + \text{H.c.}\right] \\ & + g_Z \left[\left(\frac{1}{2} - \frac{2}{3}s^2_W\right)\bar{t}_L\gamma^\mu t_L + \left(-\frac{2}{3}s^2_W\right)\bar{t}_R\gamma^\mu t_R + \left(-\frac{1}{2} + \frac{1}{3}s^2_W\right)\bar{b}_L\gamma^\mu b_L \right. \\ & \left. + \left(\frac{1}{3}s^2_W\right)\bar{b}_R\gamma^\mu b_R + \left(-\frac{1}{2} + \frac{1}{3}s^2_W\right)\bar{b}'\gamma^\mu b' + \left(\frac{1}{2} - \frac{2}{3}s^2_W\right)\bar{t}'\gamma^\mu t'\right] Z_\mu \ . \end{aligned} \tag{2.45}$$

After KK reduction, each term in the Lagrangian is associated with an overlap integral which is not shown explicitly above and can be written in a general form

$$\mathcal{I}_{q_1 q_2 V} = \frac{1}{\pi R}\int_0^{\pi R} dy \ e^{ky} f_{q_1}(y) f_{q_2}(y) f_V(y) \ , \tag{2.46}$$

where $q, q_{1,2} = \{t_{L,R}, b_{L,R}, t', b'\}$ and V is the vector bosons, either massless $V_0 = \{A, G\}$ or massive $V_M = \{W^\pm, Z\}$. Photon and gluons will remain massless after EWSB since $U(1)_{EM}$ and $SU(3)_c$ are unbroken. Therefore, the zero mode profiles of V_0, $f^{(0)}_{V_0}(y)$ will remain flat (*i.e.* $f^{(0)}_{V_0}(y) = 1$) after EWSB along the extra dimension. Thus, the overlap integrals $\mathcal{I}_{qqV_0}$ become unity using the orthonormality condition of the normalized fermion wavefunctions. Whereas, $\mathcal{I}_{q_1q_2V_M}$ differ from unity by a few percent as the zero modes $V^{(0)}_M$ of the EW gauge bosons mix with their higher KK modes due to EWSB. In our analysis we neglect this small mixing effect and take all the $\mathcal{I}_{q_1q_2V_M} = 1$ for simplicity. Later we give more quantitative comparison of mixing effects in quark sector and in gauge sector.

The couplings $q_1q_2V_M$ can be modified due to the mixing in the quark sector or mixing in the EW gauge boson sector. For LHC phenomenology, it is sufficient to consider only the dominant mixing effects *i.e.* mixing between zero mode and first KK excitations. In this thesis, we keep mixings between zero-mode and first KK modes in the quark sector as these can be bigger owing to the smaller mass of the custodians with $(-,+)$ BCs. Whereas, we ignore mixing effects in the gauge sector as these effects are only a few percent compared to the mixing effects in the quark sector.

To compare the mixing effects in the quark sector with the EW gauge boson sector more quantitatively, we, for example, consider the $b' \to tW$ decay. The $b'tW$ vertex can be modified due to $b \leftrightarrow b'$ mixing as well as mixing in the W sector. The contribution to the $b' \to tW$ decay rate due to $b \leftrightarrow b'$ mixing is proportional to the $(M_{bb'}/M_{b'})^2$ (in the limit of large $M_{b'}$), while due to $W^{(0)}_L \leftrightarrow W^{(1)}_R$ mixing it is proportional to $\left(\sqrt{k\pi R}(g_R/g_L)M^2_W/M^2_{W'_R}\right)^2$ [95]. An additional $\sqrt{k\pi R}$ appears in the gauge sector mixing, due to an IR-brane-peaked Higgs. The gauge KK boson mass $M_{W'_R}$ is constrained to be about 2 TeV by EWPT (see Ref. [96] and references therein). Thus, the contribution due to gauge KK mixing is about 1.3 % of the quark KK mixing contribution for $M_{b'} = M_{W'_R} = 2$ TeV (we assume $g_L = g_R$ and $\sqrt{k\pi R} \sim 6$), and even smaller for lighter b' masses. Therefore, the mixing effects in the gauge sector have little impact on the phenomenology we discuss in this thesis and we do not consider any gauge KK mixing anymore.

The top and the bottom quarks Yukawa couplings are obtained from the invariant combination $\overline{(\mathbf{2},\mathbf{1})}_{1/6}(\mathbf{2},\mathbf{2})_0(\mathbf{1},\mathbf{2})_{1/6}$. The 5D Yukawa interactions are given by [52]

$$\begin{aligned}
\mathcal{L}_Y &\supset -\tilde{\lambda}_t \bar{Q}_L \Sigma Q_{t_R} - \tilde{\lambda}_b \bar{Q}_L \Sigma Q_{b_R} + \text{H.}c. \\
\mathcal{L}_Y &\supset -\tilde{\lambda}_t \left(\bar{t}_L t_R \phi_0^* + \bar{t}_L b_R' \phi^+ - \bar{b}_L t_R \phi^- + \bar{b}_L b_R' \phi^0\right) \\
&\quad - \tilde{\lambda}_b \left(\bar{t}_L t_R' \phi_0^* + \bar{t}_L b_R \phi^+ - \bar{b}_L t_R' \phi^- + \bar{b}_L b_R \phi^0\right) + \text{H.}c. \,, \qquad (2.47)
\end{aligned}$$

where $\tilde{\lambda}_{t,b}$ are dimensionless 5D Yukawa coupling constants which we take to be $\mathcal{O}(1)$. One can write down an equivalent 4D theory by performing a KK expansion of the fields and then integrating over the extra dimension. After EWSB, the off-diagonal terms in the bottom mass matrix resulting from Eq. (2.47) lead to the mixing of the fields $(b^{(0)}, b'^{(n)}, b_L^{(n)}, b_R^{(n)})$ where n (≥ 1) denotes the n-th KK states. To simplify our analysis, we consider only the dominant mixing (*i.e.* $b^{(0)} \leftrightarrow b'^{(1)}$ mixing) and ignore mixing to all heavier KK states. We call $b^{(0)}$ and $b'^{(1)}$ as b and b' respectively and write the bottom mass matrix in the (b, b') basis as follows:

$$\mathcal{L} \supset - \begin{pmatrix} \bar{b}_L & \bar{b}_L' \end{pmatrix} \begin{pmatrix} M_b & M_{bb'} \\ 0 & M_{b'} \end{pmatrix} \begin{pmatrix} b_R \\ b_R' \end{pmatrix} + \text{H.}c. \,, \qquad (2.48)$$

where $M_b = \tilde{\lambda}_b \frac{v}{\sqrt{2}} \frac{e^{k\pi R}}{k\pi R} f_{Q_L}^{(0)}(\pi R) f_{Q_{b_R}}^{(1)}(\pi R)$, the $M_{b'}$ is the vector-like mass of the b', and $M_{bb'} = \tilde{\lambda}_t \frac{v}{\sqrt{2}} \frac{e^{k\pi R}}{k\pi R} f_{Q_L}^{(0)}(\pi R) f_{Q_{t_R}}^{(1)}(\pi R)$ is the off-diagonal mass term induced after EWSB, and f_ψ's are the fermion wavefunctions which depend on the fermion bulk mass parameters c_ψ.

The mass matrix in Eq. (2.48) is diagonalized by a bi-orthogonal rotation and we denote the sine (cosine) of the mixing angles by $s_{L,R}$ ($c_{L,R}$).

$$\begin{pmatrix} b_L \\ b_L' \end{pmatrix} = \begin{pmatrix} c_L & -s_L \\ s_L & c_L \end{pmatrix} \begin{pmatrix} b_{1L} \\ b_{2L} \end{pmatrix} \; ; \quad \begin{pmatrix} b_R \\ b_R' \end{pmatrix} = \begin{pmatrix} c_R & -s_R \\ s_R & c_R \end{pmatrix} \begin{pmatrix} b_{1R} \\ b_{2R} \end{pmatrix} \,, \qquad (2.49)$$

where $\{b_1, b_2\}$ are the mass eigenstates. The mixing angles are given by

$$\tan(2\theta_L) = -\frac{2M_{b'}M_{bb'}}{(M_{b'}^2 - M_b^2 - M_{bb'}^2)} \;\; ; \quad \tan(2\theta_R) = -\frac{2M_b M_{bb'}}{(M_{b'}^2 - M_b^2 + M_{bb'}^2)} \; . \tag{2.50}$$

The mass eigenstates are given by

$$M_{b_1,b_2}^2 = \frac{1}{2}M_{b'}^2\left[\left(1 + x_b^2 + x_{bb'}^2\right) \mp \sqrt{\left(1 + x_b^2 + x_{bb'}^2\right)^2 - 4x_b^2}\right] \; , \tag{2.51}$$

where $x_b = M_b/M_{b'}$ and $x_{bb'} = M_{bb'}/M_{b'}$. In the limit of large $M_{b'}$, *i.e.*, $x_b, x_{bb'} \ll 1$, the mixing angles behave as $\sin\theta_L \sim x_{bb'}$, $\sin\theta_R \sim x_b x_{bb'}$ and the mass eigenvalues become

$$M_{b_1} = M_b\left[1 + \mathcal{O}\left(x_b^4, x_{bb'}^4\right)\right] \;\; ; \quad M_{b_2} = M_{b'}\left[1 + \frac{1}{2}x_{bb'}^2 + \mathcal{O}\left(x_b^4, x_{bb'}^4\right)\right] \; . \tag{2.52}$$

The Lagrangian in the mass basis consists of the following interactions [53],

- Interactions with photon (A) and gluon (G):

$$\mathcal{L}_{A+G} \supset -\frac{e}{3}\left[\bar{b}_1\gamma^\mu b_1 + \bar{b}_2\gamma^\mu b_2\right] A_\mu + g_S\left[\bar{b}_1\gamma^\mu T^\alpha b_1 + \bar{b}_2\gamma^\mu T^\alpha b_2\right] G_\mu^\alpha \; . \tag{2.53}$$

- Interactions with W-boson (charged current):

$$\mathcal{L}_W \supset \frac{g_W}{\sqrt{2}}\left[c_L \bar{t}_L\gamma^\mu b_{1L} - s_L \bar{t}_L\gamma^\mu b_{2L}\right] W_\mu^+ + \text{H.}c. \; . \tag{2.54}$$

- Interactions with Z-boson (neutral current):

$$\begin{aligned}\mathcal{L}_Z \supset g_Z\Bigg[&\left(-\frac{1}{2}c_L^2 + \frac{1}{3}s_W^2\right)\bar{b}_{1L}\gamma^\mu b_{1L} + \left(\frac{1}{3}s_W^2\right)\bar{b}_{1R}\gamma^\mu b_{1R} \\ &+ \left(-\frac{1}{2}s_L^2 + \frac{1}{3}s_W^2\right)\bar{b}_{2L}\gamma^\mu b_{2L} + \left(\frac{1}{3}s_W^2\right)\bar{b}_{2R}\gamma^\mu b_{2R} \\ &+ \left\{\left(\frac{1}{2}c_L s_L\right)\bar{b}_{1L}\gamma^\mu b_{2L} + \text{H.c.}\right\}\Bigg] Z_\mu \; .\end{aligned} \tag{2.55}$$

- Interactions with Higgs boson:

$$\mathcal{L}_h \supset -\frac{1}{v}\Big[(M_b\ c_L c_R + M_{bb'}\ c_L s_R)\,\bar{b}_{1L} b_{1R} + (M_b\ s_L s_R - M_{bb'}\ s_L c_R)\,\bar{b}_{2L} b_{2R}$$
$$+ (-M_b\ c_L s_R + M_{bb'}\ c_L c_R)\,\bar{b}_{1L} b_{2R} + (-M_b\ s_L c_R - M_{bb'}\ s_L s_R)\,\bar{b}_{2L} b_{1R}\Big]\, h + \text{H.c.}\ . \tag{2.56}$$

As mentioned earlier, the $Z\bar{b}_L b_L$ coupling is very precisely measured. The shift in the $Z\bar{b}_L b_L$ coupling can be defined as

$$\Delta\kappa_{Zb_Lb_L} = \kappa_{BSM} - \kappa_{SM} = \frac{g_Z}{2}(1 - c_L^2) = \frac{g_Z}{2} s_L^2\ . \tag{2.57}$$

The experimental constraints shown in Eq. (2.35) require that this shift be less than about 1%, roughly implying $s_L \lesssim 0.1$, *i.e.* equivalently $M_{b'} \gtrsim 10 M_{bb'} \approx 3$ TeV. We have discussed the model without $Z\bar{b}_L b_L$ protection for simplicity, but in the following subsections we discuss models with $Z\bar{b}_L b_L$ protection which will relax this constraints.

2.2.3 Models with $Z\bar{b}_L b_L$ protection

In this section we consider a class of models where $Z\bar{b}_L b_L$ coupling is protected using the custodial symmetry as detailed in [92]. We follow the discussion of Ref. [97]. One way to achieve this is to embed the third generation left handed quarks (t_L and b_L) into the bidoublet representation (*i.e.* $(\mathbf{2},\mathbf{2})_{2/3}$) of the bulk gauge group $\mathcal{G} = SU(2)_L \otimes SU(2)_R \otimes U(1)_X$ and the theory should be made invariant under a discrete $\mathbb{Z}_2$ ($SU(2)_L \leftrightarrow SU(2)_R$) symmetry. The component fields of the bidoublet representation are

$$Q_L \equiv (\mathbf{2},\mathbf{2})_{\frac{2}{3}} = \begin{pmatrix} t_L^{(++)} & \chi^{(-+)} \\ b_L^{(++)} & t'^{(-+)} \end{pmatrix}\ . \tag{2.58}$$

In the bidoublet representation above, the $SU(2)_L$ acts vertically and $SU(2)_R$ acts horizontally. Note that to complete the bidoublet representation, two new quarks namely χ (charge 5/3) and t' (charge 2/3) have been introduced. The K.E. term for Q_L is

$$\mathcal{L}_{KE} \supset \mathrm{Tr}\left[\bar{Q}_L i\gamma^\mu D_\mu Q_L\right] \ , \tag{2.59}$$

where D_μ is the covariant derivative define in Eq. (2.44). The Higgs field also transforms as a bidoublet representation of the gauge group $\mathcal{G}$ as shown in Eq. (2.42).

It is possible to write down an invariant top quark Yukawa coupling with either the $t_R = (\mathbf{1}, \mathbf{1})_{2/3}$ or with $t_R \subset (\mathbf{1}, \mathbf{3})_{2/3} \oplus (\mathbf{3}, \mathbf{1})_{2/3}$ [92]. We will elaborate on both these possibilities in the following subsections. The invariant bottom quark Yukawa coupling can be written in many ways by embedding b_R in various multiplets of $\mathcal{G}$ as detailed in [92]. The c-parameter required for obtaining the correct bottom mass implies that all the $(-,+)$ partners of b_R are heavier than 3 TeV. Thus, the mixing effects of these heavier quarks with the lighter modes are much smaller and phenomenologically uninteresting. Therefore, we ignore all b_R partners in our analysis and show couplings of b_R in some places where its relevant.

Model with $t_R \subset (\mathbf{1}, \mathbf{1})_{2/3}$

In this subsection we explore the possibility where t_R is a singlet under both $SU(2)_L$ and $SU(2)_R$, and this can be represented as

$$Q_{t_R} \equiv (\mathbf{1}, \mathbf{1})_{\frac{2}{3}} = t_R^{(++)} \ . \tag{2.60}$$

The K.E. term for Q_{t_R} can be written as (K.E. term for Q_L is given in Eq. (2.59))

$$\mathcal{L}_{KE} \supset \bar{Q}_{t_R} i\gamma^\mu D_\mu Q_{t_R} \ . \tag{2.61}$$

Using the invariant operator $\overline{(\mathbf{2},\mathbf{2})}_{2/3}(\mathbf{2},\mathbf{2})_0(\mathbf{1},\mathbf{1})_{2/3}$ one can write down the 5D top-quark Yukawa coupling as follows

$$\mathcal{L}_Y \supset \tilde{\lambda}_t \mathrm{Tr}\left[\bar{Q}_L \Sigma\right] Q_{t_R} + \mathrm{H}.c. \tag{2.62}$$

$$\mathcal{L}_Y \supset \tilde{\lambda}_t \left(\bar{t}_L t_R \phi_0^* - \bar{b}_L t_R \phi^- + \bar{\chi} t_R \phi^+ + \bar{t}' t_R \phi_0\right) + \mathrm{H}.c. \ , \tag{2.63}$$

where $\tilde{\lambda}_t \equiv k\lambda_t$ is the dimensionless $5D$ Yukawa coupling. The K.E. terms in Eq. (2.59) and (2.61) can be expressed in the mass basis of gauge bosons as

$$\begin{aligned}\mathcal{L}_{KE} \supset & \sum_q \left(eQ_q \bar{q}\gamma^\mu q A_\mu + g_S \bar{q}\gamma^\mu T^\alpha q G_\mu^\alpha\right) + \frac{g_W}{\sqrt{2}}\left[\left(\bar{t}_L\gamma^\mu b_L + \bar{\chi}\gamma^\mu t'\right) W_\mu^+ + \mathrm{H.c.}\right] \\ & + g_Z \left[\left(\frac{1}{2} - \frac{2}{3}s_W^2\right)\bar{t}_L\gamma^\mu t_L + \left(-\frac{2}{3}s_W^2\right)\bar{t}_R\gamma^\mu t_R + \left(-\frac{1}{2} + \frac{1}{3}s_W^2\right)\bar{b}_L\gamma^\mu b_L\right. \\ & \left. + \left(\frac{1}{3}s_W^2\right)\bar{b}_R\gamma^\mu b_R + \left(\frac{1}{2} - \frac{5}{3}s_W^2\right)\bar{\chi}\gamma^\mu\chi + \left(-\frac{1}{2} - \frac{2}{3}s_W^2\right)\bar{t}'\gamma^\mu t'\right] Z_\mu \ .\end{aligned} \tag{2.64}$$

In the quark sector, the top-mass matrix including zero-mode and the lightest KK mode mixing but neglecting the smaller mixings to heavier KK states is

$$\mathcal{L}_t \supset \begin{pmatrix} \bar{t}_L & \bar{t}'_L \end{pmatrix} \begin{pmatrix} M_t & 0 \\ M_{tt'} & M_{t'} \end{pmatrix} \begin{pmatrix} t_R \\ t'_R \end{pmatrix} + \mathrm{H}.c. \tag{2.65}$$

where $M_t = \tilde{\lambda}_t \frac{v}{\sqrt{2}} \frac{e^{k\pi R}}{k\pi R} f_{Q_L}^{(0)}(\pi R) f_{Q_{t_R}}^{(1)}(\pi R)$, the $M_{t'}$ is the vectorlike mass of t', and $M_{tt'} = \tilde{\lambda}_t \frac{v}{\sqrt{2}} \frac{e^{k\pi R}}{k\pi R} f_{Q_L}^{(0)}(\pi R) f_{Q_{t_R}}^{(1)}(\pi R)$ is the off-diagonal mass term induced after EWSB. We have not shown mass matrix for the bottom sector as in this model the new heavy charge $-1/3$ vectorlike quarks could only arise as the partners of the b_R and we ignore them since they are very heavy. The above mass matrix is diagonalized by a bi-orthogonal rotation as follows

$$\begin{pmatrix} t_L \\ t'_L \end{pmatrix} = \begin{pmatrix} c_L & -s_L \\ s_L & c_L \end{pmatrix} \begin{pmatrix} t_{1L} \\ t_{2L} \end{pmatrix} \ ; \quad \begin{pmatrix} t_R \\ t'_R \end{pmatrix} = \begin{pmatrix} c_R & -s_R \\ s_R & c_R \end{pmatrix} \begin{pmatrix} t_{1R} \\ t_{2R} \end{pmatrix} \ , \tag{2.66}$$

where $\{t_1, t_2\}$ are the mass eigenstates (ignoring mixings to higher KK states), with the mixing angles given by

$$\tan(2\theta_L) = -\frac{2M_t M_{tt'}}{(M_{t'}^2 - M_t^2 + M_{tt'}^2)} \; ; \quad \tan(2\theta_R) = -\frac{2M_{tt'} M_{t'}}{(M_{t'}^2 - M_t^2 - M_{tt'}^2)} \; . \tag{2.67}$$

The mass eigenvalues $m_{1,2}$ are given by

$$M_{t_1,t_2}^2 = \frac{M_{t'}^2}{2}\left[(1 + x_t^2 + x_{tt'}^2) \mp \sqrt{(1 + x_t^2 + x_{tt'}^2)^2 - 4x_t^2}\right] \; , \tag{2.68}$$

where $x_t = M_t/M_{t'}$ and $x_{tt'} = M_{tt'}/M_{t'}$. In the limit of large $M_{t'}$, *i.e.*, $x_t, x_{tt'} \ll 1$, the mixing angles behave as $\sin\theta_R \sim x_{tt'}$, $\sin\theta_L \sim x_t x_{tt'}$ and the mass eigenvalues become

$$M_{t_1} = M_t\left[1 + \mathcal{O}\left(x_t^4, x_{tt'}^4\right)\right] \; ; \quad M_{t_2} = M_{t'}\left[1 + \frac{1}{2}x_{tt'}^2 + \mathcal{O}\left(x_t^4, x_{tt'}^4\right)\right] \; . \tag{2.69}$$

In the mass basis the final interactions we obtain are as below

- Interactions with photon (A) and gluon (G):

$$\begin{aligned}\mathcal{L}_{A+G} \supset\; & e\left[\left(\frac{5}{3}\right)\bar{\chi}\gamma^\mu\chi + \left(\frac{2}{3}\right)\bar{t}_1\gamma^\mu t_1 + \left(\frac{2}{3}\right)\bar{t}_2\gamma^\mu t_2 + \left(-\frac{1}{3}\right)\bar{b}\gamma^\mu b\right] A_\mu \\ & + g_S\left[\bar{\chi}\gamma^\mu T^\alpha\chi + \bar{t}_1\gamma^\mu T^\alpha t_1 + \bar{t}_2\gamma^\mu T^\alpha t_2 + \bar{b}\gamma^\mu T^\alpha b\right] G_\mu^\alpha \; .\end{aligned} \tag{2.70}$$

- Interactions with W-boson (charged current):

$$\begin{aligned}\mathcal{L}_W \supset\; & \frac{g_W}{\sqrt{2}}\left(c_L\bar{t}_{1L}\gamma^\mu b_L - s_L\bar{t}_{2L}\gamma^\mu b_L + s_L\bar{\chi}_L\gamma^\mu t_{1L} + c_L\bar{\chi}_L\gamma^\mu t_{2L}\right. \\ & \left. + s_R\bar{\chi}_R t_{1R} + c_R\bar{\chi}_R t_{2R}\right) W_\mu^+ + \text{H.c.} \; .\end{aligned} \tag{2.71}$$

- Interactions with Z-boson (neutral current):

$$\begin{aligned}\mathcal{L}_Z \supset g_Z \Bigg\{ & \left[\frac{1}{2}\cos 2\theta_L - \frac{2}{3}s_W^2\right]\bar{t}_{1L}\gamma^\mu t_{1L} + \left[-\frac{1}{2}\cos 2\theta_L - \frac{2}{3}s_W^2\right]\bar{t}_{2L}\gamma^\mu t_{2L} \\ & + \left[-\frac{1}{2}s_R^2 - \frac{2}{3}s_W^2\right]\bar{t}_{1R}\gamma^\mu t_{1R} + \left[-\frac{1}{2}c_R^2 - \frac{2}{3}s_W^2\right]\bar{t}_{2R}\gamma^\mu t_{2R} \\ & + \left[\left(-\frac{1}{2}\sin 2\theta_L\right)\bar{t}_{2L}\gamma^\mu t_{1L} + \left(-\frac{1}{2}s_R c_R\right)\bar{t}_{2R}\gamma^\mu t_{1R} + \mathrm{H.c.}\right] \\ & + \left[-\frac{1}{2} - s_W^2\left(-\frac{1}{3}\right)\right]\bar{b}_L\gamma^\mu b_L + \left[\frac{1}{2} - s_W^2\left(\frac{5}{3}\right)\right]\bar{\chi}\gamma^\mu\chi\Bigg\} Z_\mu \, . \end{aligned} \tag{2.72}$$

- Interactions with Higgs boson:

$$\begin{aligned}\mathcal{L}_h \supset -\frac{1}{v} & \left[(M_t\; c_L c_R + M_{tt'}\; s_L c_R)\,\bar{t}_{1L}t_{1R} + (M_t\; s_L s_R - M_{tt'}\; c_L s_R)\,\bar{t}_{2L}t_{2R}\right. \\ & \left. + (-M_t\; c_L s_R - M_{tt'}\; s_L s_R)\,\bar{t}_{1L}t_{2R} + (-M_t\; s_L c_R + M_{tt'}\; c_L c_R)\,\bar{t}_{2L}t_{1R}\right] h + \mathrm{H.c.}\, . \end{aligned} \tag{2.73}$$

Model with $t_R \subset (\mathbf{1},\mathbf{3})_{2/3} \oplus (\mathbf{3},\mathbf{1})_{2/3}$

In this subsection we pursue another option in which the t_R is embedded into a $(\mathbf{1},\mathbf{3})_{2/3}$ representation of $\mathcal{G}$. As explained in Ref. [92], due to the required P_{LR} invariance to protect the $Z\bar{b}_L b_L$ coupling, a $(\mathbf{3},\mathbf{1})_{2/3}$ must also be added. Thus, the multiplet containing the t_R is

$$Q_{t_R} \equiv Q'_{t_R} \oplus Q''_{t_R} = \begin{pmatrix} \frac{1}{\sqrt{2}}t_R^{(++)} & \chi'^{(-+)} \\ b'^{(-+)} & -\frac{1}{\sqrt{2}}t_R^{(++)} \end{pmatrix} \oplus \begin{pmatrix} \frac{1}{\sqrt{2}}t''^{(-+)} & \chi''^{(-+)} \\ b''^{(-+)} & -\frac{1}{\sqrt{2}}t''^{(-+)} \end{pmatrix} \, , \tag{2.74}$$

where $Q'_{t_R} \equiv (\mathbf{1},\mathbf{3})_{2/3}$ and $Q''_{t_R} \equiv (\mathbf{3},\mathbf{1})_{2/3}$. The top Yukawa couplings are obtained from [97]

$$\mathcal{L}_Y \supset -\sqrt{2}\tilde{\lambda}'_t \mathrm{Tr}\left[\bar{Q}_L \Sigma Q'_{t_R}\right] - \sqrt{2}\tilde{\lambda}''_t \mathrm{Tr}\left[\bar{Q}_L Q''_{t_R}\Sigma\right] + \mathrm{H.}c. \tag{2.75}$$

where $\tilde{\lambda}'_t, \tilde{\lambda}''_t$ are 5D Yukawa couplings and P_{LR} invariance of the theory requires $\tilde{\lambda}'_t = \tilde{\lambda}''_t$ which we just denote as $\tilde{\lambda}_t$ henceforth. The P_{LR} invariance also implies that the c-

parameters for Q'_{t_R} and Q''_{t_R} are equal *i.e.* $c_{Q'_{t_R}} = c_{Q''_{t_R}}$. The factor of $\sqrt{2}$ is introduced for proper normalization of the K.E. terms. The EM charge of the b', b'' is $-1/3$, the t'' is $2/3$ and the χ', χ'' is $5/3$.

One can write bottom Yukawa couplings that respects the custodial symmetry of the theory. Many possibilities for b_R representations are discussed in Ref. [92]. For example with $Q_L = (\mathbf{2},\mathbf{2})_{2/3}$, the b_R can be embedded into the representation $Q'_{b_R} = (\mathbf{1},\mathbf{3})_{2/3}$ and the bottom Yukawa coupling is obtained from, $\mathcal{L}_Y \supset -\lambda'_b \mathrm{Tr}\left[\bar{Q}_L \Sigma Q'_{b_R}\right] + \mathrm{H.}c.$. However, this choice breaks the P_{LR} symmetry but the resulting shifts are acceptable since the c_{b_R} choice required to get the correct bottom mass makes the new states in the Q'_{b_R} multiplet all very heavy (>3 TeV). Therefore, in our analysis we have ignored the mixing effects and the signatures of these heavy b_R partners.

After EWSB due to $\langle\phi_0\rangle = v/\sqrt{2}$, with the restrictions due to P_{LR} symmetry mentioned earlier the mass matrices are [97]

- Mass matrix for charge $-1/3$ states (b sector):

$$\mathcal{L}_b \supset -\begin{pmatrix} \bar{b}_L & \bar{b}'_L & \bar{b}''_L \end{pmatrix} \begin{pmatrix} M_b & \sqrt{2}M_{bb'} & \sqrt{2}M_{bb''} \\ 0 & M_{b'} & 0 \\ 0 & 0 & M_{b''} \end{pmatrix} \begin{pmatrix} b_R \\ b'_R \\ b''_R \end{pmatrix} + \mathrm{H.}c. \tag{2.76}$$

  where due to P_{LR} symmetry we have $M_{b'} = M_{b''}$ and $M_{bb'} = M_{bb''}$.

- Mass matrix for charge $2/3$ states (t sector):

$$\mathcal{L}_t \supset -\begin{pmatrix} \bar{t}_L & \bar{t}'_L & \bar{t}''_L \end{pmatrix} \begin{pmatrix} M_t & 0 & M_{tt''} \\ -M_{tt'} & M_{t'} & -M_{t't''} \\ 0 & -M_{t't''} & M_{t''} \end{pmatrix} \begin{pmatrix} t_R \\ t'_R \\ t''_R \end{pmatrix} + \mathrm{H.}c. \tag{2.77}$$

- Mass matrix for charge 5/3 states (χ sector):

$$\mathcal{L}_\chi \supset -\begin{pmatrix} \bar{\chi}_L & \bar{\chi}'_L & \bar{\chi}''_L \end{pmatrix} \begin{pmatrix} M_\chi & \sqrt{2}M_{\chi\chi'} & \sqrt{2}M_{\chi\chi''} \\ \sqrt{2}M_{\chi\chi'} & M_{\chi'} & 0 \\ \sqrt{2}M_{\chi\chi''} & 0 & M_{\chi''} \end{pmatrix} \begin{pmatrix} \chi_R \\ \chi'_R \\ \chi''_R \end{pmatrix} + \text{H.}c. \tag{2.78}$$

where due to P_{LR} symmetry we have $M_{\chi'} = M_{\chi''}$ and $M_{\chi\chi'} = M_{\chi\chi''}$.

In all the three mass matrices, the M_q (except M_b and M_t) denotes the vectorlike masses, and the EWSB generated off-diagonal masses M_{pq} which are given by

$$M_{pq} = \tilde{\lambda}_t \frac{v}{\sqrt{2}} \frac{e^{k\pi R}}{k\pi R} f^{(n)}_{Q_{p_L}}(\pi R) f^{(m)}_{Q_{q_R}}(\pi R) \tag{2.79}$$

The chiral masses also arise after EWSB and they are

$$M_{b,t} = \tilde{\lambda}_{b,t} \frac{v}{\sqrt{2}} \frac{e^{k\pi R}}{k\pi R} f^{(0)}_{Q_L}(\pi R) f^{(0)}_{Q_{b_R,t_R}}(\pi R) \tag{2.80}$$

In the above expressions $\tilde{\lambda}_{b,t} \equiv k\lambda_{b,t}$ is the dimensionless 5D Yukawa couplings.

Next, our aim is to work out couplings in the mass basis. For this, let us define the flavor eigenstates $\psi^\alpha \equiv (\psi \ \psi' \ \psi'')^T$ and the mass eigenstates as $\psi^i \equiv (\psi_1 \ \psi_2 \ \psi_3)^T$ for each of the $\psi = \{b, t, \chi\}$ sectors (where $\alpha, i = \{1, 2, 3\}$). We perform a bi-orthogonal rotation (we take the masses to be real for simplicity) $\psi^\alpha_L = R^{\alpha i}_{\psi_L} \psi^i_L$ and $\psi^\alpha_R = R^{\alpha i}_{\psi_R} \psi^i_R$ to diagonalize each of the mass matrices in Eqs. (2.76)-(2.78).

The gluonic and photonic interactions are standard and we do not show them explicitly. We have checked numerically that mixing effects in the gauge sector can give only a few percent correction to the couplings we are interested in. Therefore, we ignore differences in the overlap integrals and take all $\mathcal{I} = 1$ while deriving Lagrangian terms. In unitary gauge the interactions we obtain in the mass basis are as below:

- Interactions with W boson (charged current):

$$\begin{aligned}\mathcal{L}_W \supset \frac{g_W}{\sqrt{2}} & \left[R^{1i^*}_{t_L} R^{1j}_{b_L} \bar{t}^i_L \gamma^\mu b^j_L + R^{1i^*}_{\chi_L} R^{2j}_{t_L} \bar{\chi}^i_L \gamma^\mu t^j_L + R^{1i^*}_{\chi_R} R^{2j}_{t_R} \bar{\chi}^i_R \gamma^\mu t^j_R \right. \\ & + \sqrt{2}\left(R^{3i^*}_{t_L} R^{3j}_{b_L} \bar{t}^i_L \gamma^\mu b^j_L - R^{3i^*}_{\chi_L} R^{3j}_{t_L} \bar{\chi}^i_L \gamma^\mu t^j_L + R^{3i^*}_{t_R} R^{3j}_{b_R} \bar{t}^i_R \gamma^\mu b^j_R \right. \\ & \left.\left. - R^{3i^*}_{\chi_R} R^{3j}_{t_R} \bar{\chi}^i_R \gamma^\mu t^j_R\right)\right] W^+_{L\,\mu} + \text{H.}c. \; . \end{aligned} \tag{2.81}$$

- Interactions with Z boson (neutral current):

$$\mathcal{L}_Z \supset g_Z \left[R^{\alpha i^*}_{\psi_{L,R}} \left(q^{3L}_{\psi^\alpha_{L,R}} - Q_\psi s^2_W\right) R^{\alpha j}_{\psi_{L,R}}\right] \bar{\psi}^i_{L,R} \gamma^\mu \psi^j_{L,R} Z_\mu \;, \tag{2.82}$$

where $Q_\psi = \{-1/3, 2/3, 5/3\}$ are EM charges and the q^{3L} are the $SU(2)_L$ charges of $\psi = \{b, t, \chi\}$ as given below

$$\begin{aligned} & q^{3L}_{b^\alpha_L} = \{-1/2, 0, -1\}\,,\ q^{3L}_{t^\alpha_L} = \{1/2, -1/2, 0\}\,,\ q^{3L}_{\chi^\alpha_L} = \{1/2, 0, 1\} \\ & q^{3L}_{b^\alpha_R} = \{0, 0, -1\}\,,\ q^{3L}_{t^\alpha_R} = \{0, -1/2, 0\}\,,\ q^{3L}_{\chi^\alpha_R} = \{1/2, 0, 1\} \end{aligned} \tag{2.83}$$

- Interactions with Higgs boson:

$$\mathcal{L}_h \supset -\frac{1}{v}\left[M_b\; R^{11^*}_{b_L} R^{11}_{b_R} \bar{b}_{1L} b_{1R} + M_t\; R^{11^*}_{t_L} R^{11}_{t_R} \bar{t}_{1L} t_{1R} + M^\psi_{\alpha\beta}\; R^{\alpha i^*}_{\psi_L} R^{\beta j}_{\psi_R} \bar{\psi}^i_L \psi^j_R\right] h + \text{H.}c. \; . \tag{2.84}$$

where $M^\psi_{\alpha\beta}$ ($\alpha \neq \beta = \{1, 2, 3\}$) are the off-diagonal mass terms of ψ-sector induced after EWSB.

b-mass matrix diagonalization

We have shown in the earlier sections some simple analytical derivation of mixing angles and Lagrangian terms for those cases where mass matrices were 2×2 dimensions. But it is not always possible to give simple analytical results for mass matrices with dimensions 3×3 or more. That is why, for the case of $t_R \subset (\mathbf{1}, \mathbf{3})_{2/3} \oplus (\mathbf{3}, \mathbf{1})_{2/3}$ model we present the general structure of the interaction terms and use numerical diagonalization for the LHC phenomenology. However, for the b-sector we derive some simple analytical results in some limiting cases. From those results we observe some interesting features of these models.

In case of b mass matrix in Eq. (2.76), due to P_{LR} symmetry we have $M_{b'} = M_{b''}$ ($= M$ say) and $M_{bb'} = M_{bb''}$ ($= m$ say). Taking $M_b = 0$ in the b mass matrix since $M_b \ll M$ and defining $r = m/M$, we find two orthogonal rotation matrices in the following form [97]

$$R_L = \frac{1}{\sqrt{1+2r^2}} \begin{pmatrix} -1 & 0 & \sqrt{2}r \\ r & -\frac{\sqrt{1+2r^2}}{\sqrt{2}} & \frac{1}{\sqrt{2}} \\ r & \frac{\sqrt{1+2r^2}}{\sqrt{2}} & \frac{1}{\sqrt{2}} \end{pmatrix} \quad ; \quad R_R = \begin{pmatrix} 1 & 0 & 0 \\ 0 & -\frac{1}{\sqrt{2}} & \frac{1}{\sqrt{2}} \\ 0 & \frac{1}{\sqrt{2}} & \frac{1}{\sqrt{2}} \end{pmatrix} \tag{2.85}$$

with the mass eigenvalues $0, M, M\sqrt{1+2r^2}$. The b_1 is identified as the SM b-quark, and the zero eigenvalue will be lifted when non-zero M_b is included. In unitary gauge the interaction terms in the mass basis are (we will not show charged current interactions since they involve diagonalization of t and χ sectors)

- Interactions with Z boson (neutral current):

$$\begin{aligned}\mathcal{L}_Z \supset g_Z \Bigg\{ & \left(-\frac{1}{2} - s_W^2 Q_b\right) \bar{b}_{1L}\gamma^\mu b_{1L} + \left(-s_W^2 Q_b\right) \bar{b}_{1R}\gamma^\mu b_{1R} + \left(-\frac{1}{2} - s_W^2 Q_b\right) \\ & \times \left(\bar{b}_{2L}\gamma^\mu b_{2L} + \bar{b}_{2R}\gamma^\mu b_{2R} + \bar{b}_{3L}\gamma^\mu b_{3L} + \bar{b}_{3R}\gamma^\mu b_{3R}\right) + \left[\left(\frac{-r}{\sqrt{2+4r^2}}\right) \bar{b}_{1L}\gamma^\mu b_{2L} \right. \\ & \left. + \left(\frac{-1}{\sqrt{4+8r^2}}\right) \bar{b}_{2L}\gamma^\mu b_{3L} + \bar{b}_{2R}\left(-\frac{1}{2}\right) b_{3R} + \text{H.c.}\right] \Bigg\} Z_\mu \end{aligned} \tag{2.86}$$

where $Q_b = -1/3$. We have taken all $\mathcal{I}_{\psi\psi V} = 1$ as earlier, ignoring corrections to this due to EWSB $(0)-(1)$ gauge boson mixing which are at most a few percent. Note that the $b_1 b_1 Z$ interactions come out standard due to the custodial protection.

- Interactions with Higgs boson:

$$\mathcal{L}_h \supset \frac{m}{v}\left[-\left(\frac{2\sqrt{2}r}{\sqrt{1+2r^2}}\right)\bar{b}_{3L}b_{3R}+\left(\frac{2}{\sqrt{1+2r^2}}\right)\bar{b}_{1L}b_{3R}\right]h+\mathrm{H}.c.\ . \tag{2.87}$$

The Higgs interactions are got by replacing $v \to v(1+h/v)$.

Interestingly we observe that in Eqs. (2.86) and (2.87), some possible interaction terms (like b_1b_3Z, b_1b_2h etc.) are not present. This is because, due to the P_{LR} symmetry of the theory the b-mass matrix has a special structure and some couplings will become zero after mixing. In the next chapter we will show various parameters and couplings for the different warped models we have discussed here.

Chapter 3

Warped-model parameters and couplings

In this chapter we present the parameter choices, which we use for our numerical results, for the different warped-space models discussed in Chapter 2. New vectorlike fermions with EM charge -1/3, 2/3 and 5/3 arise in those warped models and we generally denote them as b', t' and χ respectively. The vectorlike fermions can mix among themselves and with the SM quarks as shown in the previous chapter. After mixing we denote the n-th mass eigenstates of ψ type quark (where $\psi = \{b', t', \chi\}$) by ψ_n except for the SM quarks where we use t or t_1 and b or b_1 interchangeably. We parametrize the left and right couplings of ψ_n with the SM fields as follows

- Interactions with V: $\kappa_{\psi_{nL}\psi_{mL}V}\ \bar{\psi}_{nL}\gamma^\mu\psi_{mL}V_\mu$, $\kappa_{\psi_{nR}\psi_{mR}V}\ \bar{\psi}_{nR}\gamma^\mu\psi_{mR}V_\mu$

- Interactions with Higgs: $\kappa_{\psi_{nL}\psi_{mR}h}\ \bar{\psi}_{nL}\psi_{mR}h$, $\kappa_{\psi_{nR}\psi_{mL}h}\ \bar{\psi}_{nR}\psi_{mL}h$

where $n, m = \{1, 2, 3\}$, $\psi_n = \{b_n, t_n, \chi_n\}$ and $V = \{W^\pm, Z\}$. For convenience we call the model without $Z\bar{b}_Lb_L$ protection as the "doublet top" or DT model where t_R is embedded in a doublet of $SU(2)_R$. Similarly, in case of the $Z\bar{b}_Lb_L$ protected models, we call the model with $t_R \subset (\mathbf{1},\mathbf{1})_{2/3}$ as the "singlet top" or ST model and the model with $t_R \subset (\mathbf{1},\mathbf{3})_{2/3} \oplus (\mathbf{3},\mathbf{1})_{2/3}$ as the "triplet top" or TT model. In all these models, we have seven free model parameters, they are the 5D Yukawa couplings $\tilde{\lambda}_{b,t}$, the lowest gauge KK mass M_{KK}, the three bulk mass parameters c_{q_L}, c_{t_R} and c_{b_R} and the combination kR. The theoretical constraint on k is $k/M_{Pl} \lesssim 0.1$ for the theory not to be in the quantum gravity regime [98]. We find that after mixing the couplings relevant for our study are largely insensitive to the choice of $k\pi R$ and $\tilde{\lambda}_{b,t}$; for instance, for $M_{KK} = 3$ TeV, varying k/M_{Pl} between 0.1 and 1 changes the couplings by at most 1 % and varying $\tilde{\lambda}_{b,t}$ between 1 and 2 changes couplings only by about a few percent. For our numerical analysis we set $\tilde{\lambda}_{b,t} = 1$ and take M_{KK} to be 3 TeV. Various choices of c-parameters are possible that reproduce the measured masses and couplings. After fixing kR, M_{KK}, $\tilde{\lambda}_{b,t}$ and imposing the physical top mass $m_t = 172$ GeV and bottom mass $m_b = 4.2$ GeV constraints, only one free parameter remains. For our numerical studies we take c_{q_L} as the free parameter, and show various masses and couplings as functions of c_{q_L}.

Due to mass-mixing in the top and bottom sectors, the CKM matrix element V_{tb} can be shifted. The current measured value of $|V_{tb}|$ from the direct measurement of the single top production cross section at the Tevatron with $\sqrt{s} = 1.96$ TeV is $|V_{tb}| = 0.88 \pm 0.07$ with a limit [78] of $|V_{tb}| > 0.77$ at the 95% C.L. assuming a top quark mass $m_t = 170$ GeV. While presenting the results for the warped-space models, the parameters we use for numerical computations satisfy the above $|V_{tb}|$ constraint.

3.1 b' Parameters and Couplings

New charge -1/3 quarks appear in the DT (one new state b') and the TT (two new states b' and b'') models. In Fig. 3.1 we display the mass eigenvalues M_{b_n} (where $n = 2, 3$) as functions of c_{q_L} in the DT and TT models. We observe that in the region $c_{q_L} \gtrsim 0$ is the phenomenologically interesting region at the LHC since $M_{b_n} \lesssim 2$ TeV. We find that in Eq. (2.48) the off-diagonal mass term $M_{bb'} \sim m_t$ in the DT model. Thus, for simplicity in our paper in Ref. [99] we use the benchmark couplings shown in Table 3.1 taking $M_{bb'} = 172$ GeV for our model independent study of the b' phenomenology. In Table 3.2

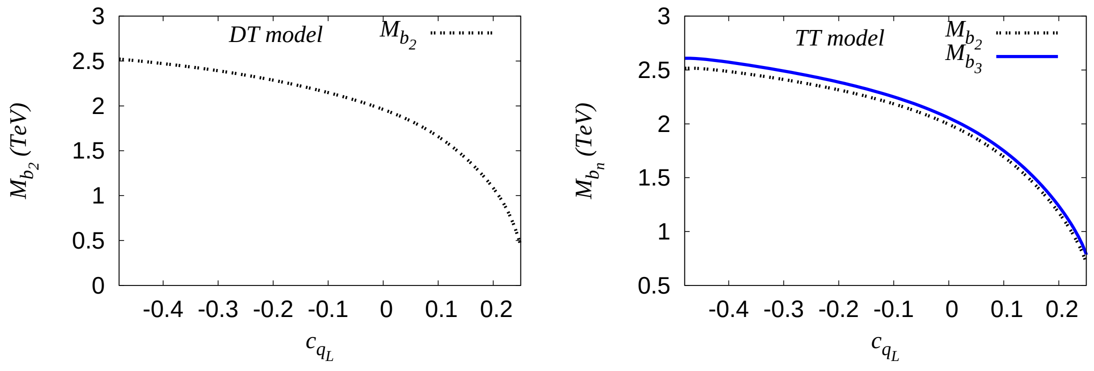

(a) (b)

Figure 3.1: M_{b_n} (where $n = 2, 3$) as functions of c_{q_L} in the DT and TT models, with $\tilde{\lambda}_t = 1$, $\tilde{\lambda}_b = 1$ and $M_{KK} = 3$ TeV.

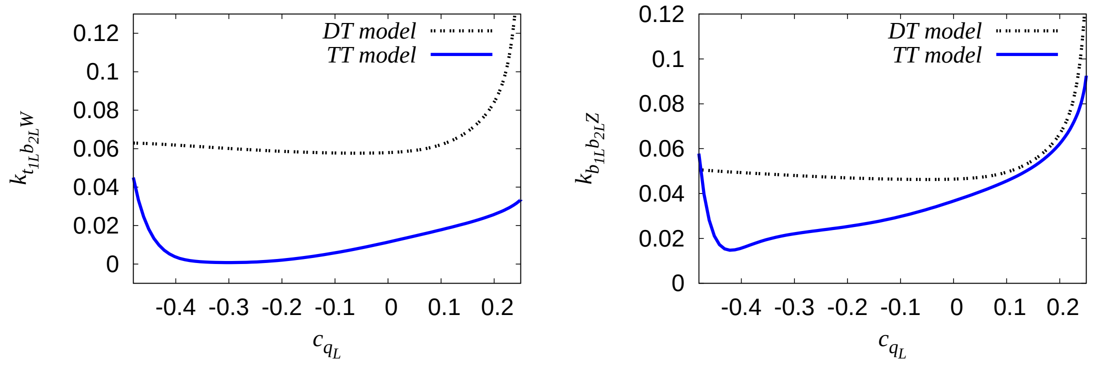

(a) (b)

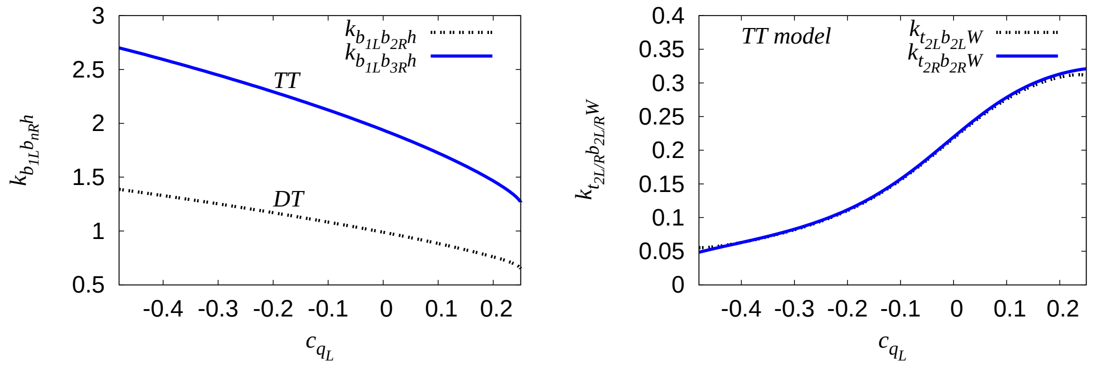

(c) (d)

Figure 3.2: The couplings as functions of c_{q_L} in the DT and TT models, with $\tilde{\lambda}_t = 1$, $\tilde{\lambda}_b = 1$ and $M_{KK} = 3$ TeV.

we show the parameters for some benchmark points in the TT model. The elements of the rotation matrices $R^{12}_{b_L}$ and $R^{12}_{b_R}$ are given in section 2.2.3.

M_{b_2} (GeV)	250	500	750	1000	1250	1500
$\kappa_{b_{1L}b_{2L}Z}$	0.185	0.121	0.084	0.064	0.051	0.043
$\kappa_{t_{1L}b_{2L}W}$	0.322	0.161	0.107	0.080	0.064	0.054
$\kappa_{b_{1L}b_{2R}h}$	0.505	0.663	0.687	0.697	0.700	0.702
M_{b_2} (GeV)	1750	2000	2250	2500	2750	3000
$\kappa_{b_{1L}b_{2L}Z}$	0.037	0.032	0.029	0.026	0.024	0.022
$\kappa_{t_{1L}b_{2L}W}$	0.046	0.040	0.036	0.032	0.029	0.027
$\kappa_{b_{1L}b_{2R}h}$	0.704	0.704	0.705	0.705	0.705	0.705

Table 3.1: The benchmark masses and couplings used in the model independent b_2 signatures in Chapter 4. These couplings are obtained taking $M_{bb'} = 172$ GeV.

$\mathcal{B}$	c_{q_L}	c_{t_R}	c_{b_R}	$R^{12}_{b_L}$	$R^{12}_{b_R}$
$\mathcal{B}_1$	0.259	-0.464	0.562	-0.400	-0.0034
$\mathcal{B}_2$	0.247	-0.414	0.566	-0.299	-0.0017
$\mathcal{B}_3$	0.226	-0.350	0.569	-0.242	-0.0010
$\mathcal{B}_4$	0.197	-0.274	0.571	-0.207	-0.0007
$\mathcal{B}_5$	0.156	-0.186	0.574	-0.186	-0.0005
$\mathcal{B}_6$	0.098	-0.088	0.577	-0.173	-0.0004
$\mathcal{B}$	M_{b_2}	$\kappa_{t_{1L}b_{2L}W}$	$\kappa_{b_{1L}b_{2L}Z}$	$\kappa_{b_{2L}t_{2L}W}$	$\kappa_{b_{2R}t_{2R}W}$
$\mathcal{B}_1$	500	-0.118	0.210	0.300	0.322
$\mathcal{B}_2$	750	-0.077	0.158	0.311	0.321
$\mathcal{B}_3$	1000	-0.060	0.128	0.313	0.319
$\mathcal{B}_4$	1250	-0.050	0.109	0.311	0.315
$\mathcal{B}_5$	1500	-0.044	0.098	0.303	0.306
$\mathcal{B}_6$	1750	-0.041	0.091	0.283	0.286

Table 3.2: Benchmark parameters (parameter set denoted by $\mathcal{B}$) and couplings obtained using $\tilde{\lambda}_t = 1$, $\tilde{\lambda}_b = 1$ and $M_{KK} = 3$ TeV in the TT model for b_2 phenomenology.

The presence of large off-diagonal terms both in the DT and TT models can lead to a shift in V_{tb}. In the DT model we have $V_{tb} \approx \cos\theta_L$ and in the TT model $V_{tb} \approx R^{11*}_{t_L} R^{11}_{b_L}$, and for the lower b' masses this may be somewhat close to the experimental limit quoted earlier. While generating benchmark couplings, we check that V_{tb} satisfy the experimental limit.

In Fig. 3.2 we display some relevant couplings of b_n in the DT and the TT models as functions of c_{q_L}. There are some interesting features we observed in the TT model. In the TT model we have $M_{b'} = M_{b''}$ due to the P_{LR} symmetry of the theory and we find that the $b_{1L}b_{2R}h$ and $b_{1R}b_{2L}h$ couplings to be zero as a consequence of this. The $b_{2L}b_{3R}h$

and $b_{2R}b_{3L}h$ couplings are also zero. Furthermore, the P_{LR} symmetry also constrains $M_{bb'} = M_{bb''}$ and as a result we find that b_3b_1Z (both L and R) couplings to be zero. These are explicitly seen in the analytical formulas shown in Eqs. (2.86) and (2.86) in the small mixing limit. In Fig. 3.2 we observe that in the TT model $\kappa_{t_{2L}b_{2L}W} \approx \kappa_{t_{2R}b_{2R}W}$ which we expect since b_2 and t_2 are both vectorlike. In Fig. 3.1 we see after mass matrix diagonalization we have two almost degenerate states b_2 and b_3.

3.2 t' Parameters and Couplings

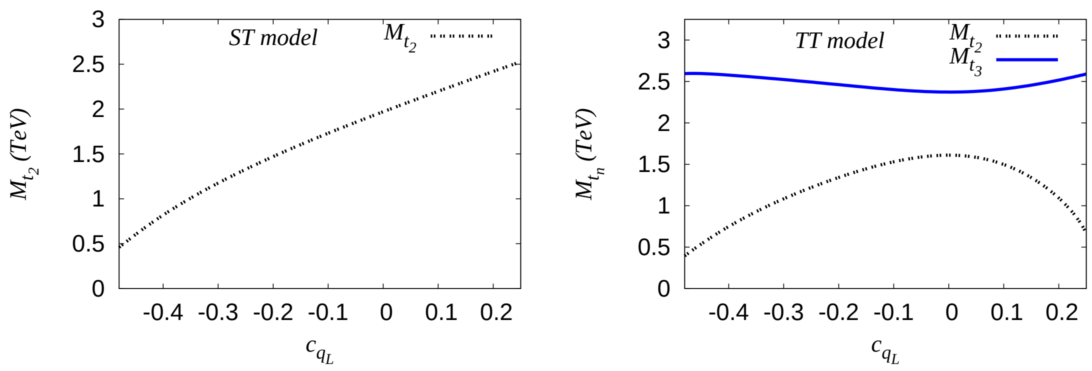

(a) (b)

Figure 3.3: M_{t_n} (where $n = 2, 3$) as functions of c_{q_L} in the ST and TT models, with $\tilde{\lambda}_t = 1$, $\tilde{\lambda}_b = 1$ and $M_{KK} = 3$ TeV.

New charge 2/3 quarks appear in the DT (one new state t'), ST (one new state t') and TT (two new states t' and t'') models. In Fig. 3.3 we display the mass eigenvalues M_{t_n} (where $n = 2, 3$) as functions of c_{q_L}. In the DT model, the t' is quite heavy (above 3 TeV) due to the choice of the c_{b_R} required for the correct $m_b = 4.2$ GeV, making its LHC discovery challenging. Therefore, we will not discuss the t' phenomenology further in the DT model. In Fig. 3.3 we observe that in the region $c_{q_L} \lesssim 0$ is the phenomenologically interesting region for the ST model at the LHC since $M_{t_2} \lesssim 2$ TeV in this region. The M_{t_2} as a function of c_{q_L} in the TT model shows an unusual behavior – with increasing c_{q_L}, it first increases and then decreases. We understand this from the diagonalization of top mass matrix, since we find that one side, $c_{q_L} \lesssim 0$, corresponds to $M_{t'} < M_{t''}$ while

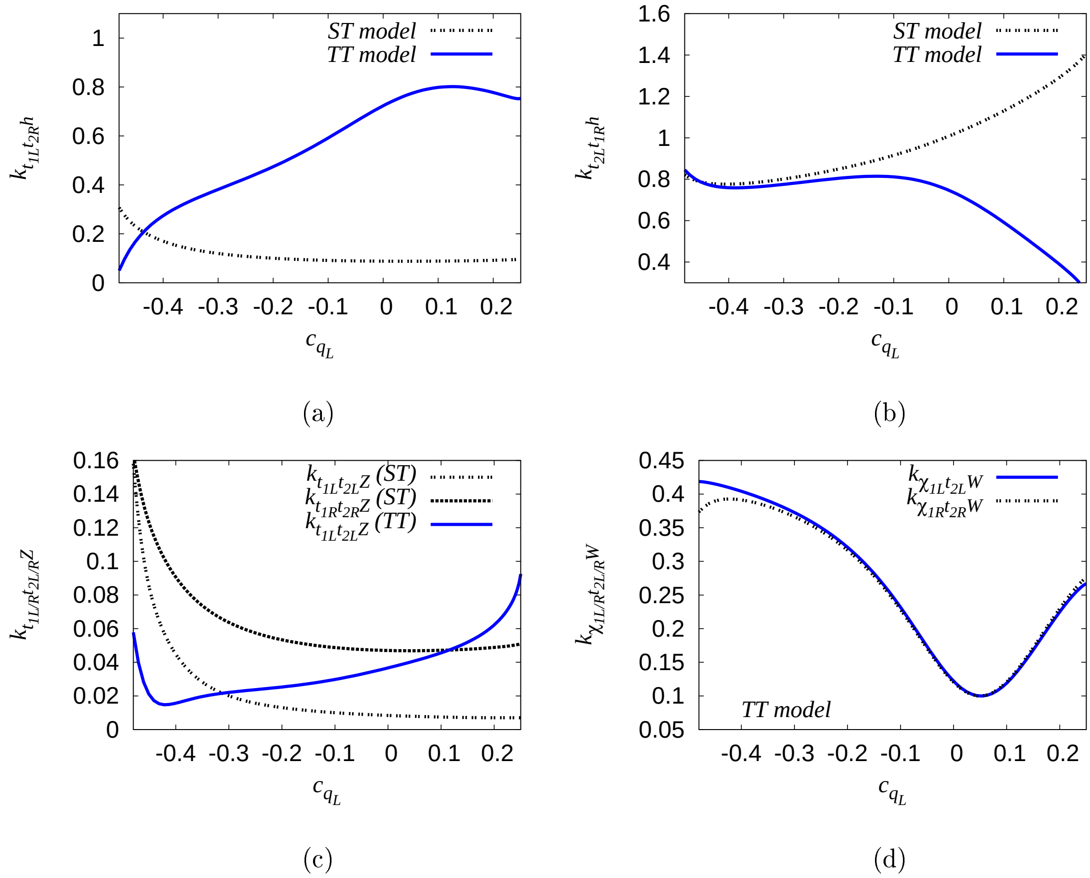

Figure 3.4: The couplings as functions of c_{q_L} in the ST and TT models, with $\tilde{\lambda}_t = 1$, $\tilde{\lambda}_b = 1$ and $M_{KK} = 3$ TeV.

the other to $M_{t'} > M_{t''}$ and the maximum is attained when $M_{t'} = M_{t''}$.

In Fig. 3.4 we display some relevant couplings of t_2 as functions of c_{q_L} in the ST and TT models. We note that the couplings $\kappa_{t_2\chi_1 W}$ are large since it is given by the $t'\chi W$ or $t''\chi'' W$ couplings, and is not proportional to any small off-diagonal mixing-matrix elements. We also note that both left and right $\kappa_{t_2\chi_1 W}$ couplings are almost equal due to the vectorlike nature of t_2 and χ_1. In Table 3.3 we display the benchmark parameters and couplings in the ST model for the t_2 phenomenology that are used for our numerical computations.

$\mathcal{T}$	c_{q_L}	c_{t_R}	c_{b_R}	$\sin\theta_L$	$\sin\theta_R$
$\mathcal{T}_1$	-0.471	0.196	0.586	-0.167	-0.442
$\mathcal{T}_2$	-0.419	0.216	0.585	-0.062	-0.262
$\mathcal{T}_3$	-0.356	0.204	0.584	-0.034	-0.195
$\mathcal{T}_4$	-0.279	0.179	0.583	-0.022	-0.161
$\mathcal{T}_5$	-0.191	0.140	0.581	-0.016	-0.141
$\mathcal{T}_6$	-0.094	0.082	0.578	-0.013	-0.130

$\mathcal{T}$	M_{t_2}	$\kappa_{t_{2L}t_{1R}h}$	$\kappa_{t_{1L}t_{2R}h}$	$\kappa_{t_{2R}t_{1R}Z}$	$\kappa_{t_{2L}t_{1L}Z}$
$\mathcal{T}_1$	500	0.806	0.277	0.148	0.123
$\mathcal{T}_2$	750	0.769	0.176	0.094	0.046
$\mathcal{T}_3$	1000	0.778	0.134	0.071	0.026
$\mathcal{T}_4$	1250	0.807	0.111	0.059	0.017
$\mathcal{T}_5$	1500	0.851	0.098	0.052	0.012
$\mathcal{T}_6$	1750	0.915	0.090	0.048	0.010

Table 3.3: Benchmark parameters (parameter set denoted by $\mathcal{T}$) and couplings obtained using $\tilde{\lambda}_t = 1$, $\tilde{\lambda}_b = 1$ and $M_{KK} = 3$ TeV in the ST model for t_2 phenomenology.

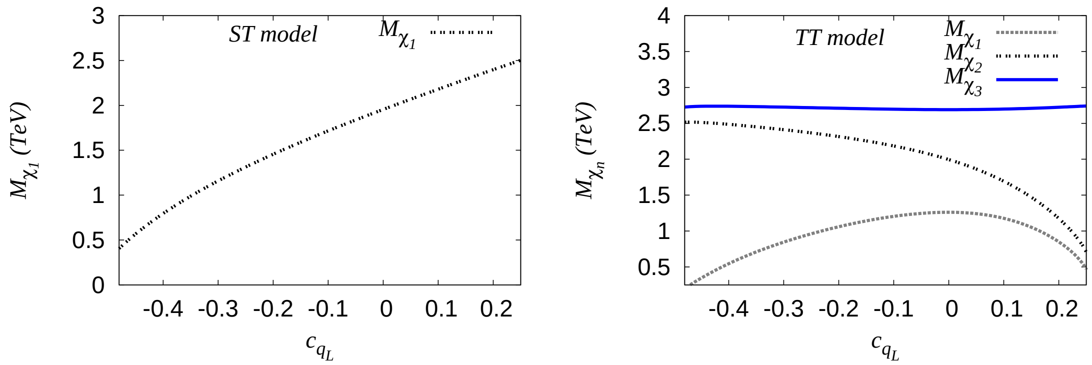

(a) (b)

Figure 3.5: M_{χ_n} (where $n = 2, 3$) as functions of c_{q_L} in the ST and TT models, with $\tilde{\lambda}_t = 1$, $\tilde{\lambda}_b = 1$ and $M_{KK} = 3$ TeV.

3.3 χ Parameters and Couplings

New charge 5/3 quarks appear in the ST (one new state χ) and TT (three new states χ, χ' and χ'') models. In Fig. 3.5 we display the mass eigenvalues M_{χ_n} as functions of c_{q_L}. We find that $c_{q_L} \lesssim 0$ region might be phenomenologically interesting for the ST model since in this region $M_{\chi_2} \lesssim 2$ TeV that can be probed at the LHC. Similar to the M_{t_2} in the TT model, M_{χ_1} as a function of c_{q_L} shows an unusual behavior – with increasing c_{q_L}, it first increases and then decreases. This can be understood from the diagonalization of the χ

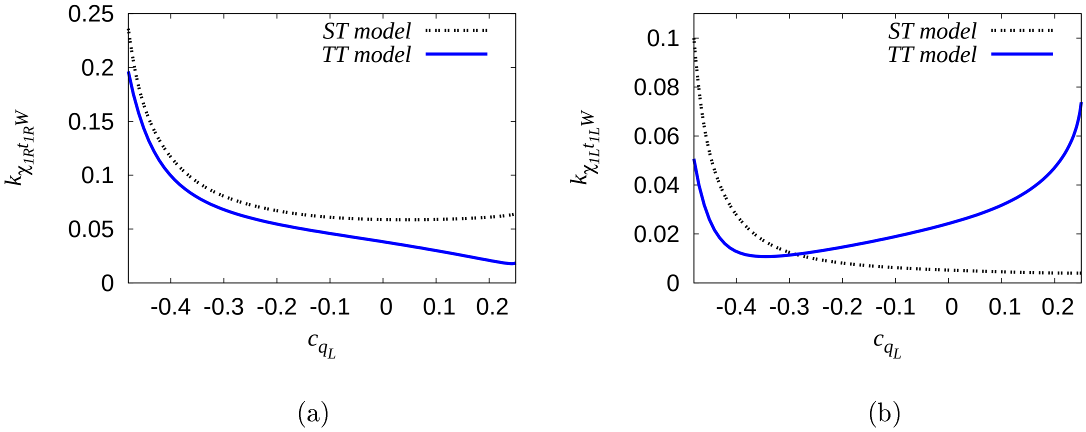

Figure 3.6: The couplings as functions of c_{q_L} in the ST and TT models, with $\tilde{\lambda}_t = 1$, $\tilde{\lambda}_b = 1$ and $M_{KK} = 3$ TeV.

mass matrix. In the TT model, after χ-χ'-χ'' mixing, the χ_2, χ_3 becomes much heavier than χ_1 because the appearance of the large off-diagonal term in the χ mass matrix causes a large split between M_{χ_1} and M_{χ_2,χ_3}. In the range $-0.5 \leq c_{q_L} \leq 0.25$, M_{χ_3} is around 2.7 TeV and $M_{\chi_2} \gtrsim 1.5$ TeV in $c_{q_L} \lesssim 0.1$ region (which is almost the entire c_{q_L} region we have considered) whereas $M_{\chi_1} < 1.3$ TeV in the entire c_{q_L} region of consideration. Therefore, for both the ST and TT models, we focus only on the phenomenology of χ_1. In Table 3.4 we explicitly display the benchmark parameters and couplings in the ST

$\mathcal{X}$	c_{q_L}	c_{t_R}	c_{b_R}	$\sin\theta_L$	$\sin\theta_R$
$\mathcal{X}_1$	-0.463	0.206	0.586	-0.136	-0.394
$\mathcal{X}_2$	-0.414	0.216	0.585	-0.058	-0.253
$\mathcal{X}_3$	-0.350	0.202	0.584	-0.033	-0.192
$\mathcal{X}_4$	-0.274	0.177	0.583	-0.022	-0.159
$\mathcal{X}_5$	-0.186	0.137	0.581	-0.016	-0.140
$\mathcal{X}_6$	-0.088	0.078	0.578	-0.013	-0.129
$\mathcal{X}$	M_χ	$\kappa_{\chi_{1R}t_{1R}W}$	$\kappa_{\chi_{1L}t_{1L}W}$	$\kappa_{\chi_{1R}t_{2R}W}$	$\kappa_{\chi_{1L}t_{2L}W}$
$\mathcal{X}_1$	500	0.182	0.063	0.424	0.458
$\mathcal{X}_2$	750	0.117	0.027	0.447	0.461
$\mathcal{X}_3$	1000	0.089	0.015	0.453	0.462
$\mathcal{X}_4$	1250	0.074	0.010	0.456	0.462
$\mathcal{X}_5$	1500	0.065	0.007	0.457	0.462
$\mathcal{X}_6$	1750	0.060	0.006	0.458	0.462

Table 3.4: Benchmark parameters (parameter set denoted by $\mathcal{X}$) and couplings obtained using $\tilde{\lambda}_t = 1$, $\tilde{\lambda}_b = 1$ and $M_{KK} = 3$ TeV in the ST model for χ phenomenology.

model that we use for our numerical computations for χ_1 phenomenology. In the ST model, we restrict ourselves to $c_{q_L} < 0$, i.e. with the q_L partners peaked towards the IR brane, since otherwise the partners become very heavy and this may be out of reach at the LHC. In the TT model we have $M_{\chi'} = M_{\chi''}$ due to the P_{LR} symmetry of the theory and we find the $\kappa_{\chi_{1L}\chi_{2R}h}$ and $\kappa_{\chi_{1R}\chi_{2L}h}$ couplings to be zero as a consequence of this. The $\chi_2\chi_3 h$ couplings are also zero. Furthermore, the P_{LR} symmetry also constrains $M_{\chi\chi'} = M_{\chi\chi''}$ and as a result we find $\chi_3\chi_1 Z$ (both L and R) couplings to be zero.

3.4 Decay widths and branching ratios

In this section we present the total decay widths (TDWs) and branching ratios (BRs) of vectorlike quarks arising in different warped models discussed in Chapter 2. The off-diagonal Lagrangian terms which lead to $q_2 \to q_1 V, q_1 h$ decays are parametrized as

$$\mathcal{L} \supset \kappa_V^L\ \bar{q}_{1L}\gamma^\mu q_{2L} V_\mu + \kappa_V^R\ \bar{q}_{1R}\gamma^\mu q_{2R} V_\mu + \kappa_h^L\ \bar{q}_{1R} q_{2L} h + \kappa_h^R\ \bar{q}_{1L} q_{2R} h + \text{H.}c.\ . \tag{3.1}$$

From the above Lagrangian terms we compute the analytical expressions of partial decay widths (PDWs) for the vectorlike quarks and the expressions are as follows,

$$\begin{aligned}
\Gamma_{q_2\to q_1 V} = {} & \frac{1}{32\pi}\frac{M_{q_2}^3}{M_V^2}\Big[\Big\{(\kappa_L^V)^2 + (\kappa_R^V)^2\Big\}\Big\{\big(1-x_{q_1}^2\big)^2 + x_V^2\left(1+x_{q_1}^2\right) - 2x_V^4\Big\} \\
& - 12\kappa_L^V\kappa_R^V x_{q_1} x_V^2\Big] \times \left(1 + x_{q_1}^4 + x_V^4 - 2x_{q_1}^2 - 2x_V^2 - 2x_{q_1}^2 x_V^2\right)^{\frac{1}{2}} \qquad (3.2) \\
\Gamma_{q_2\to q_1 h} = {} & \frac{1}{32\pi} M_{q_2}\Big[\Big\{(\kappa_L^h)^2 + (\kappa_R^h)^2\Big\}\Big\{\big(1-x_{q_1}^2 - x_h^2\big)^2\Big\} + 4\kappa_L^h\kappa_R^h x_{q_1}\Big] \\
& \times \left(1 + x_{q_1}^4 + x_h^4 - 2x_{q_1}^2 - 2x_h^2 - 2x_{q_1}^2 x_h^2\right)^{\frac{1}{2}}\ , \qquad (3.3)
\end{aligned}$$

where $x_{q_1} \equiv M_{q_1}/M_{q_2}$, $x_V \equiv M_V/M_{q_2}$ and $x_h \equiv M_h/M_{q_2}$. In any model we can obtain the TDWs and BRs of vectorlike fermions using the above equations of PDWs. In the large M_{q_2} limit (*i.e.* $M_{q_2} \gg M_{q_1}, M_V, M_h$), the PDWs shown above behave as

$$\Gamma_{q_2 \to q_1 V} \sim \frac{1}{32\pi} \frac{M_{q_2}^3}{M_V^2} \left\{ (\kappa_L^V)^2 + (\kappa_R^V)^2 \right\}; \quad \Gamma_{q_2 \to q_1 h} \sim \frac{1}{32\pi} M_{q_2} \left\{ (\kappa_L^h)^2 + (\kappa_R^h)^2 \right\} \tag{3.4}$$

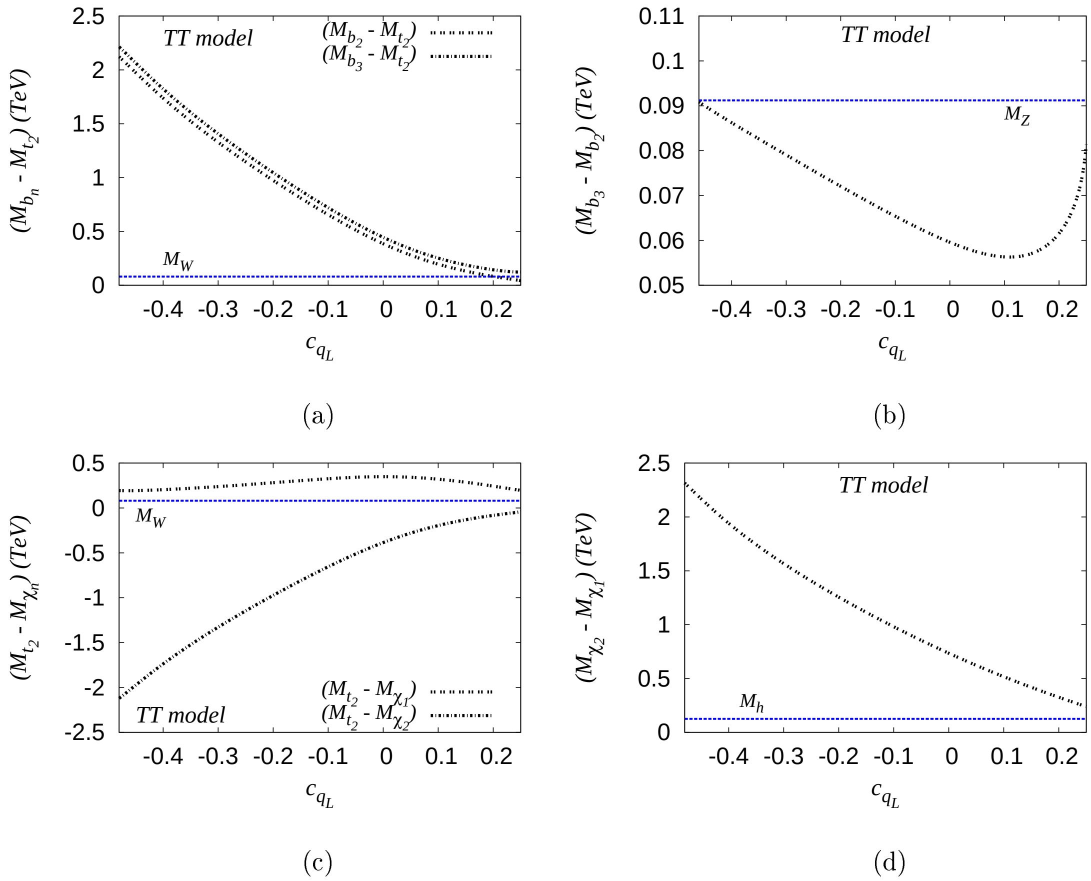

Figure 3.7: Mass differences of vectorlike quarks in the TT model as functions of c_{q_L}.

Next, we present some results for the DT, ST and TT models. In the DT model we have only one b_2 and the allowed two-body decay modes are $b_2 \to b_1 Z, b_1 h, t_1 W$. Among these three decay modes, $b_1 Z$ and $b_1 h$ modes are unique signatures of a vectorlike b_2. On the other hand, a chiral b_2 has only one decay mode *i.e.* $b_2 \to t_1 W$. Similarly, a vectorlike t_2 decays to $t_1 Z, t_1 h$ and $b_1 W$ modes as can be seen in the ST model. In the ST model we find $(M_{t_2} - M_{\chi_1}) < M_W$ in the entire c_{q_L} range we have considered. Thus, $t_2 \to \chi_1 W$ decay is not allowed in this case. Whereas, in the TT model many new two-body decay modes are allowed kinematically. For example, in Fig. 3.7(a) $(M_{b_2,b_3} - M_{t_2}) > M_W$ almost in the entire c_{q_L} range. Therefore, b_2, b_3 can decay to t_2W in addition to b_1Z, b_1h, t_1W modes. From Fig. 3.7(b) we conclude that the $b_3 \to b_2Z, b_2h$ decay modes are not possible since $(M_{b_3} - M_{b_2}) < M_Z$. Similarly, from Fig. 3.7(c) we see $t_2 \to \chi_1 W$ and $\chi_2 \to t_2W$ decays are allowed. In the ST and TT models χ_1 has only one decay mode, $\chi_1 \to t_1W$. Whereas, χ_2 in the TT model can have many decay modes. From Fig. 3.7(d) we infer that χ_2 can decay to $\chi_1 Z$ and $\chi_1 h$ in addition to t_1W, t_2W modes. In various warped models, we list possible kinematically allowed two-body decay modes of the vectorlike quarks whose phenomenology could be interesting at the LHC,

- DT model
  - $b_2 \to b_1Z, b_1h, t_1W$
- ST model
  - $t_2 \to t_1Z, t_1h, b_1W$
  - $\chi_1 \to t_1W$
- TT model
  - $b_2 \to b_1Z, b_1h, t_1W, t_2W$
  - $b_3 \to b_1Z, b_1h, t_1W, t_2W$
  - $t_2 \to t_1Z, t_1h, b_1W, \chi_1W$
  - $\chi_1 \to t_1W$
  - $\chi_2 \to \chi_1Z, \chi_1h, t_1W, t_2W$

In Fig. 3.8 we show the TDW and BRs of the b_2 as functions of M_{b_2} in the DT model. We observe that the TDW is a few percent of the mass and behaves almost linearly as a function of M_{b_2}. Its roughly linear dependence can be understood by noting that for the decay of b_2 the dominant couplings $\kappa_{b_{1L}b_{2L}V} \propto s_L \approx M_{bb'}/M_{b_2}$ (in Eqs. 2.54 and 2.55) and $\kappa_{b_{1L}b_{2R}h} \propto c_L \approx 1$ (in Eq. 2.56) in the large M_{b_2} limit. This large M_{b_2} behavior of the

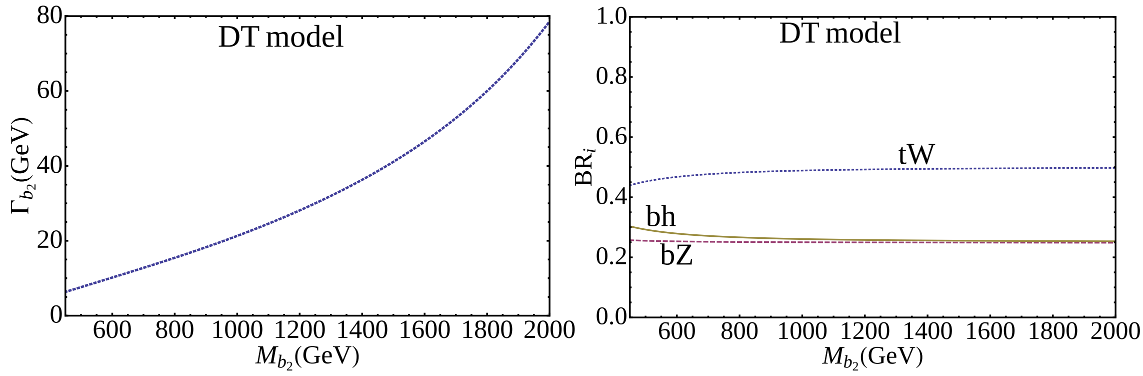

(a) (b)

Figure 3.8: Total decay width and branching ratios of b_2 in the DT model.

couplings leaves $\Gamma_i \sim M_{b_2}$ for all the PDWs. We also observe that all three decay modes have comparable BRs. Interestingly we observe that in the large M_{b_2} limit BRs of the b_2 in bW, bZ and bh decay modes are in $2:1:1$ proportion. This can be understood by looking at the couplings behavior in the large mass limit

- $\kappa_{t_{1L}b_{2L}W} = \dfrac{g_W}{\sqrt{2}} s_L \xrightarrow[M_{b_2}]{Large} \dfrac{g_W}{\sqrt{2}} \dfrac{M_{bb'}}{M_{b_2}} = \dfrac{1}{\sqrt{2}} \left(\dfrac{2M_W}{v}\right) \dfrac{M_{bb'}}{M_{b_2}}$
- $\kappa_{b_{1L}b_{2L}Z} = \dfrac{g_Z}{2} c_L s_L \xrightarrow[M_{b_2}]{Large} \dfrac{g_Z}{2} \dfrac{M_{bb'}}{M_{b_2}} = \dfrac{1}{2} \left(\dfrac{2M_Z}{v}\right) \dfrac{M_{bb'}}{M_{b_2}}$
- $\kappa_{b_{1L}b_{2R}h} = \dfrac{1}{v} \left(-M_b\ c_L s_R + M_{bb'}\ c_L c_R\right) \xrightarrow[M_{b_2}]{Large} \dfrac{M_{bb'}}{v}$

Putting this behavior in Eq. (3.4) we can see the BRs are indeed in $2:1:1$ ratio as mentioned.

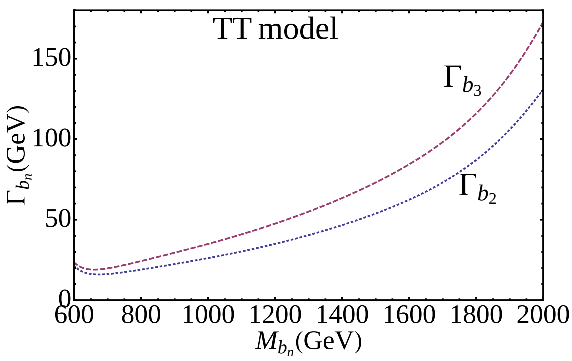

Figure 3.9: Total decay widths of b_n as functions of M_{b_n} (where $n = 2, 3$) in the TT model.

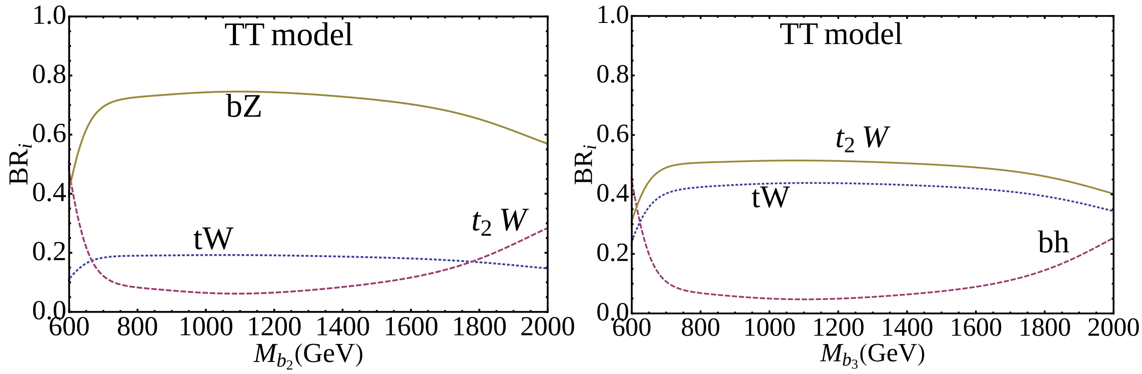

(a) (b)

Figure 3.10: Branching ratios of b_2 and b_3 as functions of M_{b_2} and M_{b_3} respectively in the TT model.

In Fig. 3.9 we show TDWs of b_n as functions of M_{b_n} in the TT model. The TDWs of b_2 and b_3 in the TT model is somewhat larger than the TDW of b_2 in the DT model. This is because in the TT model the off-diagonal mass terms in the mass matrix is $\sqrt{2}$ times bigger than that in the DT model leads to larger mixing.

Although kinematically allowed, $b_2 \to b_1 h$ and $b_3 \to b_1 Z$ decay modes are not present in the BR plots of b_2 and b_3 in the TT model as shown in Fig. 3.10. As mentioned earlier as a consequence of the P_{LR} symmetry $b_1 b_2 h$ couplings are zero which makes $BR(b_2 \to b_1 h) = 0$. On the other hand, $b_1 b_3 Z$ couplings become zero after mixing and leads to $BR(b_3 \to b_1 Z) = 0$. An additional decay mode $b_2 \to t_2 W$ opens up at large M_{b_2}. Since this BR is not too big for the masses of interest, we do not consider this mode further.

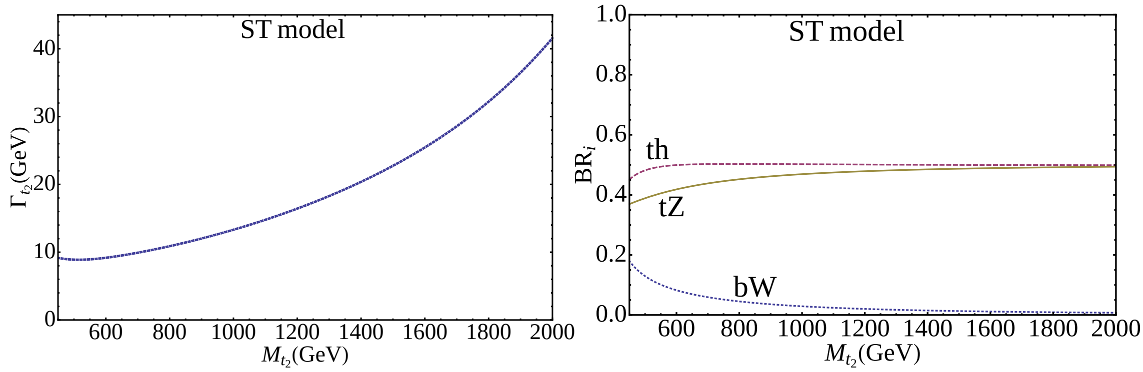

(a) (b)

Figure 3.11: Total decay width and branching ratios of t_2 in the ST model.

In Fig. 3.11 we show TDW and BR of t_2 as functions of M_{t_2} in the ST model. We notice that the $t_2 \to bW$ decay width becomes small at large M_{t_2}. The reason for this is that there is no $t'b\phi^+$ coupling in Eq. (2.63) and it will be generated after mixing as a $t_2 b\phi^+$ term. This is of $\mathcal{O}(x_{tt'})$ and is negligible in the large M_{t_2} limit. We also observe $\mathrm{BR}(t_2 \to th) \approx \mathrm{BR}(t_2 \to tZ)$ in the large M_{t_2} limit. This is similar to the case of b_2 BRs in the DT model and can be understood looking at the couplings behavior in the large mass limit.

In Fig. 3.12 we show the TDW of t_2 as a function of M_{t_2} in the TT model. We notice that for a particular M_{t_2} TDW has two values one for $c_{q_L} < 0$ and the other for $c_{q_L} > 0$. This is because in the TT model a particular M_{t_2} value can be obtained for two different c_{q_L} choices as shown in Fig. 3.3.

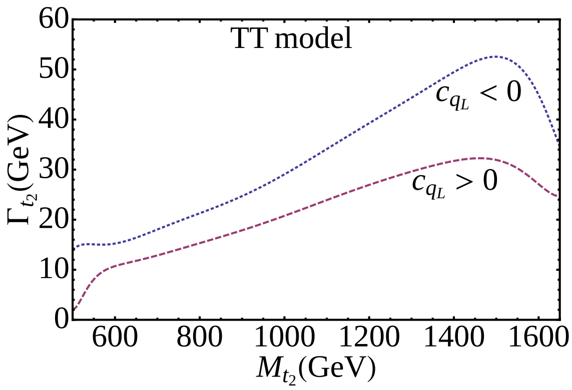

Figure 3.12: Total decay width of t_2 as a functions of M_{t_2} in the TT model for $c_{q_L} < 0$ and $c_{q_L} > 0$.

In Fig. 3.12 we show BRs of t_2 as functions of M_{t_2} in the TT model for $c_{q_L} < 0$ and $c_{q_L} > 0$. In the TT model, the additional decay mode $t_2 \to \chi_1 W$ is present, and ends up being the dominant decay mode. The reason for this is the large coupling involved here as shown in Fig. 3.4. For $c_{q_L} < 0$ the $t_2 \to tZ$ BR is quite small while for $c_{q_L} > 0$ it increases to about 0.2. Therefore, $t_2 \to tZ$ mode is also important in addition to $t_2 \to th$ mode.

In Fig. 3.14 we show TDW of χ_1 as a function of M_{χ_1} in the TT model for $c_{q_L} < 0$ and $c_{q_L} > 0$. The χ_1 BR is 100 % into the tW mode as this is the only channel accessible. The

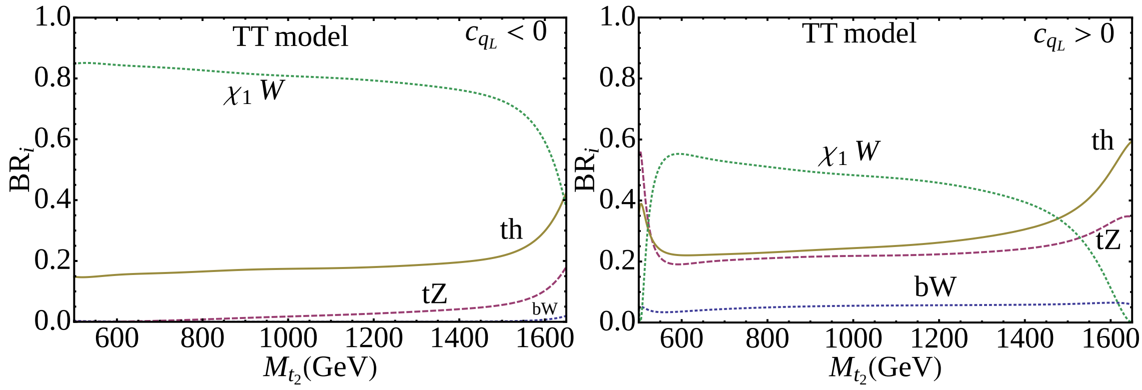

(a) (b)

Figure 3.13: Branching ratios of t_2 as functions of M_{t_2} in the TT model for $c_{q_L} < 0$ and $c_{q_L} > 0$.

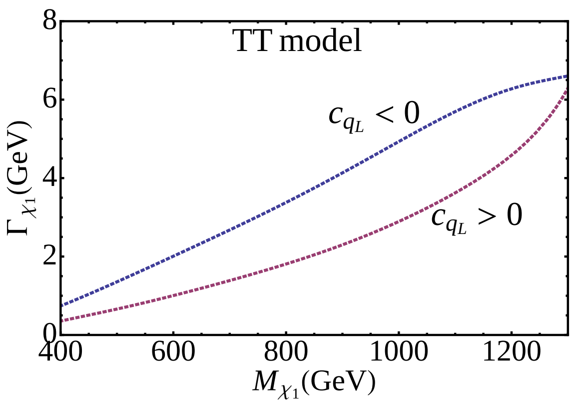

Figure 3.14: Total decay width of χ_1 as a function of M_{χ_1} in the TT model for $c_{q_L} < 0$ and $c_{q_L} > 0$.

double-valued behavior of TDW as a function of M_{χ_1} in the TT model can be understood looking at the unusual behavior of M_{χ_1} in the TT model as shown in Fig. 3.5.

In the TT model, the additional decay mode $\chi_2 \to \chi_1 Z$ is present, and ends up being the dominant decay mode with BR about 0.8. The reason for this is the large coupling involved in this decay. Although kinematically allowed, we observe that $\chi_2 \to \chi_1 h$ is not present. This is because $\chi_2\chi_1 h$ couplings are zero as a consequence of P_{LR} symmetry. We do not consider the χ_2 signatures later as we expect its production cross-section to be smaller owing to its larger mass.

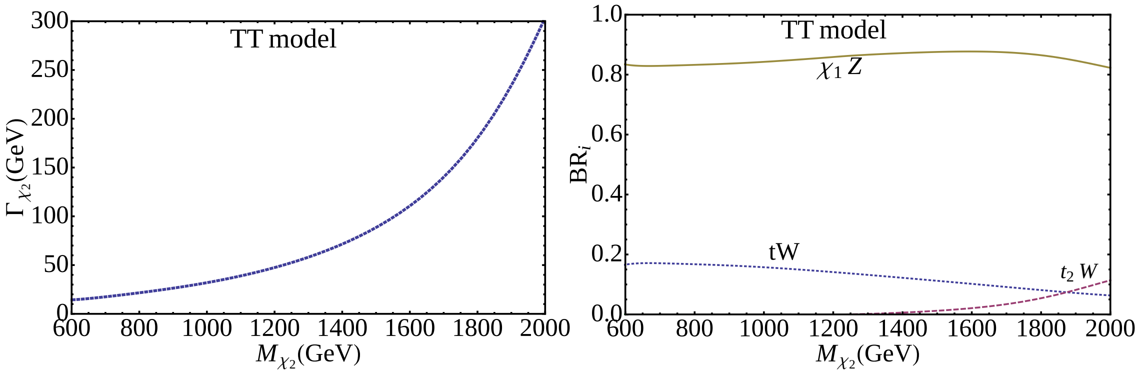

(a) (b)

Figure 3.15: Total decay width and branching ratios of χ_2 as functions of M_{χ_2} in the TT model.

Chapter 4

LHC signatures of vectorlike quarks

In this chapter we present the LHC signatures of vectorlike quarks arising in various warped-space models discussed in Chapter 2. We study the LHC signatures of EM charge -1/3, 2/3 and 5/3 vectorlike quarks, which we generally denote as b', t' and χ respectively, arising in those models. We present many signatures model-independently, and also display many results for the DT, ST and TT models for the benchmark parameter choices as given in Chapter 3. These results have been presented in Refs. [99] and [97].

Generally, at the LHC, the dominant production channel of vectorlike quarks is their pair production for the quark masses in the sub-TeV region. However in this paper, in addition to the pair production channels, we also look into some of their important single production channels. The single production channels can give useful information about model-dependent weak coupling parameters and thus, help us to identify the underlying model at colliders. In general, single production channels have less complicated final state compared to the pair-production channels and hence, mass reconstruction is easier. Moreover, in general, for a fixed mass of the heavy quark single production is less phase space suppressed than pair production. Thus, depending on the couplings, some single production channels can even be the dominant production channels if the vectorlike quark is heavy enough. For instance, for electroweak size couplings (*i.e.* g_W, g_Z order), the single production starts to dominate for vectorlike quark masses roughly about 700 GeV.

At a hadron collider such as the LHC, the resonant production of vectorlike quarks (ψ) can occur via the gg, gq and qq initiated processes where q can either be a light quark or a bottom quark. The gluon PDF (parton distribution function) dominates at low x (where x is the momentum fraction of proton carried by a parton) region whereas the quark PDFs take over at high x region. Thus, depending on M_ψ, all of the gg, gq and qq initiated processes can contribute significantly to the production of ψ at the LHC. For sub-TeV ψ mass, we expect the gluon PDF to be bigger than the quark PDFs, and therefore we expect the gg, gq and qq signal (and background) rates to be in decreasing order. Therefore, to get good significance, if the signal is qq initiated for example, the background should not be gg or gq initiated, and similarly for the other possibilities.

For each of the b', t' and χ we identify promising pair and single production channels, compute the signal (S) cross section (c.s.) and dominant SM backgrounds (B). Using signal and background c.s. we compute the luminosity required ($\mathcal{L}_5$) for 5σ significance, *i.e.* $S/\sqrt{B} = 5$, and luminosity ($\mathcal{L}_{10}$) for obtaining 10 signal events. We define the luminosity for discovery, $\mathcal{L}_D = \mathrm{Max}\{\mathcal{L}_5, \mathcal{L}_{10}\}$.

We compute the signal c.s. for various masses and compute the main irreducible SM backgrounds for these channels using Monte Carlo event generators. We have defined the warped-space model with the vectorlike quarks in the matrix-element and event generators MadGraph 5 [100] and CalcHEP Version 2.5.6 [101,102], and all our results in this section are obtained using these event generators. We use CTEQ6L [103] PDFs for all our numerical computations. If the final state involves too many particles the simulation of the full decay chain may be impractical and to reduce time for event generation, wherever possible, we use the narrow-width approximation and multiply by the appropriate BRs in order to obtain the required c.s. This will mean that the acceptance in transverse momentum (p_T) and rapidity (y) for the final state particles will not be taken into account exactly, but since we mostly deal with high-p_T particles, the inaccuracies should be small.

4.1 b' LHC signatures

If the mass of the b_2 (mass eigenstate) is in the sub-TeV region, the $pp \to b_2 b_2$ pair production is expected to have the largest production rate compared to the single production due to the larger gluon PDF and the bigger value of α_S. The QCD backgrounds for this process will also be large that can lead to poor significance in those channels. Large background can be reduced by properly choosing kinematical cuts and, we have to optimized them in order to get good significance. For processes for which QCD induced background is not present, the single production channel can lead to a good reach at the LHC. Single production of vectorlike b_2 proceeds via the offdiagonal $b_2 b_1 Z$, $b_2 b_1 h$ and $b_2 t W$ couplings. For the discovery of b_2 at the LHC, we focus on the pair production channel. To learn about the couplings we also study some important single production channels of b_2.

In this study, we consider $pp \to b_2 b_2$, $b_2 Z$, $b_2 h$ and $b_2 b Z$ processes as the discovery channel of the b_2 and to show its vector-like character. The b_2, once produced, decays to bZ, bh and tW tree level decay modes. Thus, depending on which modes we are considering, pair and single production of b_2 will lead to various final states. Here we focus on some of the interesting production channels of b_2 at the LHC to reveal its vectorlike nature.

4.1.1 $pp \to b_2 b_2$ process

Following Ref. [99], we analyze the b_2 pair production which is initiated by the gg and qq initial states as shown in Fig. 4.1.

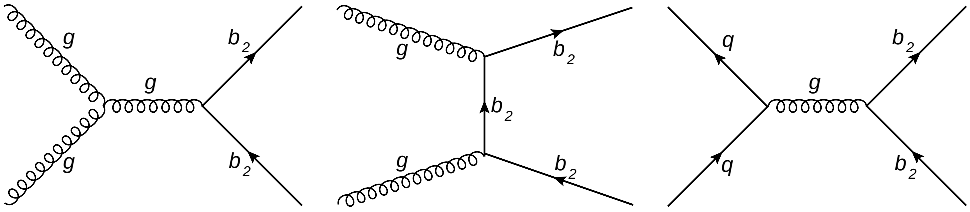

Figure 4.1: Sample partonic Feynman diagrams for $pp \to b_2 b_2$ process at the LHC.

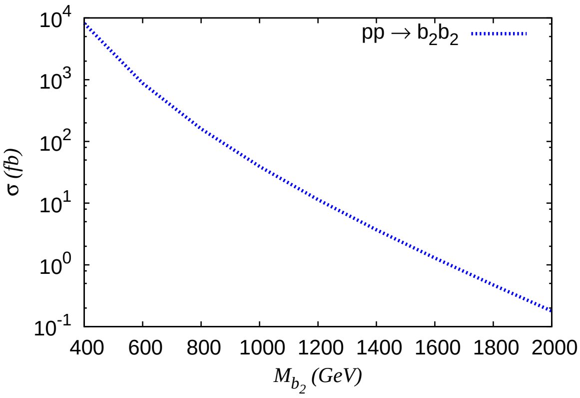

Figure 4.2: The $pp \to b_2 b_2$ c.s. as a function of M_{b_2} at the 14 TeV LHC.

Since the production c.s. is mostly dominated by the b_2 coupling to the gluon (*i.e.* g_s), our results are largely model-independent [1]. In Fig. 4.2 we show the $pp \to b_2 b_2$ c.s. as a function of M_{b_2} at the 14 TeV LHC. We see that for sub-TeV M_{b_2} the pair production c.s. is large, but decreases rapidly with increasing M_{b_2}.

$b_2 b_2 \to bZbZ$ decay mode:

Here we consider both the b_2's, produced in pair production process, decaying into the bZ mode resulting in the $bZbZ$ final state. From $bZbZ$ level one can have three possible decay patterns of Z namely,

1. *Fully hadronic:* both the Z's decay hadronically.

2. *Dileptonic (DL):* both the Z's decay leptonically.

3. *Semileptonic (SL):* one Z decays hadronically and the other decays leptonically.

Here we mainly focus on the semileptonic decay channel of the Z's. Although the fully hadronic decay channel has the largest rate, it is very difficult to reconstruct two Z's from the $bbjjjj$ final state and the QCD background is also huge for this channel. On the other hand, the dileptonic channel, although very clean and can be reconstructed with

[1] We have roughly estimated the Higgs mediated contribution via the effective ggh (top triangle diagram) vertex to b_2 pair production and find this to be much smaller than the contribution shown in Fig. 4.1.

good efficiency, suffers from low rate due to small $Z \to \ell\ell$ BR. Therefore, we consider the semileptonic channel taking one of the Z's to decay hadronically (including only u, d, c, s, but not the b) and the other Z decaying leptonically ($\ell = e, \mu$ with $\mathrm{BR}(Z \to \ell\ell) = 0.066$), resulting in the channel $pp \to b_2 b_2 \to bZbZ \to b\ell\ell bjj$. Here we demand two b-tagged jets in the final state. To avoid combinatorics issues with the four b's that will be present if the Z decays to bb, we ask that this will not happen by demanding that the tagged-b is not among the two jets that reconstruct to the Z. We obtain the signal and electroweak background c.s. at the $bZbZ$ level and multiply the $\sigma(pp \to bZbZ)$ c.s. by the factor

$$2\eta_b^2 \times \mathrm{BR}_{Z\to\ell\ell}\left[\mathrm{BR}_{Z\to jj} + (1-\eta_b)^2\, \mathrm{BR}_{Z\to bb}\right] \approx 0.019\ , \tag{4.1}$$

with $j = \{u, d, c, s\}$, where, η_b is the b-tagging efficiency, the $(1-\eta_b)^2\,\mathrm{BR}_{Z\to bb}$ term counts the $Z \to bb$ decays that fail the b-tag, and a factor of 2 is because the hadronic-Z and the leptonic-Z can be exchanged resulting in the same final state. We take the b-tagging efficiency $\eta_b = 0.5$. We obtain the QCD background at the $bjjbZ$ level as we explain in more detail below.

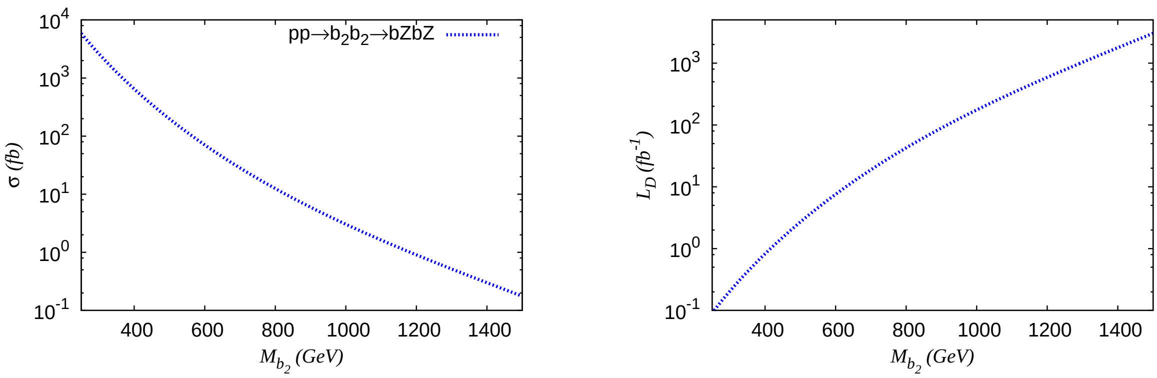

(a) (b)

Figure 4.3: (a) The $pp \to b_2 b_2 \to bZbZ$ c.s. after y, p_T cuts and, (b) the luminosity for discovery $\mathcal{L}_D$ required in the $pp \to b_2 b_2 \to bZbZ \to b\ell\ell bjj$ channel after "All cuts" with $\mathrm{BR}(b_2 \to bZ) = 1/3$ assumed at the 14 TeV LHC. See text for the details of the cuts used.

In Fig. 4.3(a) we show the $pp \to b_2 b_2 \to bZbZ$ c.s. as a function of M_{b_2} at the 14 TeV LHC after the following p_T and y cuts at the $bZbZ$ level,

$$p_T(b, Z) > 25 \text{ GeV} \ , \ |y(b, Z)| < 2.5 \ . \tag{4.2}$$

To maximize the signal at the expense of the SM background, finally we apply the following kinematical cuts at the $b\ell\ell bjj$ level:

- y and p_T cuts: (a) $|y(b, j, Z)| < 2.5$; (b) $p_T(b, j, Z) > 25$ GeV
- *Invariant mass cuts*: $|M_{jj} - M_Z| < 10$ GeV; $|M_{b_2} - M(bZ)| < 0.05 M_{b_2}$

where, in the last invariant-mass cut, we accept the event if the invariant mass of a b with either Z lies within the invariant mass window, *and*, the invariant mass of the other b with either Z also lies within the window. We define "All cuts" as the y, p_T cuts together with the invariant mass cuts shown above.

In Table 4.1 we show the signal and background c.s. after only y, p_T and "All cuts" for different values of M_{b_2} with the corresponding κ as shown in Table 3.1, and show the luminosity required for discovery ($\mathcal{L}_D$) at the 14 TeV LHC. The $(bjjbZ)_{\text{tot}}$ column in Table 4.1 shows the total background which is the sum of the QCD and electroweak backgrounds, where the QCD background is got from the components shown in the second table as

$$(bjjbZ)_{\text{QCD}} = (bjjbZ) + (1 - \eta_b)(bbjbZ) + (1 - \eta_b)^2 (bbbbZ) \ , \tag{4.3}$$

where b includes both b and $\bar{b}$, and the $(1 - \eta_b)$ factor take into account a b-quark that has failed the b-tag, *i.e.* we assume here that a b-quark that fails the b-tag will be taken to be a light-jet. We find that the luminosity required is signal-rate limited for all the M_{b_2} values we have considered.

The results shown here are largely model-independent since the production c.s. mostly relies on the color quantum number of the b_2 since the c.s. is dominated by the gluon

M_{b_2} (GeV)	Signal σ_s (in fb) $bZbZ$ y, p_T cuts	Signal σ_s (in fb) $bZbZ$ All cuts	Background σ_b (in fb) $bZbZ$ y, p_T cuts	Background σ_b (in fb) $bZbZ$ All cuts	Background σ_b (in fb) $(bjjbZ)_{\rm tot}$ y, p_T cuts	Background σ_b (in fb) $(bjjbZ)_{\rm tot}$ All cuts	$\mathcal{L}_D$ (fb^{-1})
250	25253	25082	21.804	0.3797	16938	29.52	0.021
500	171.34	148.69	21.804	0.047	16938	3.74	3.514
750	14.508	12.221	21.804	0.0097	16938	0.997	42.752
1000	2.314	1.9214	21.804	0.0027	16938	0.259	271.92
1250	0.484	0.399	21.804	0.0011	16938	0.048	1310

M_{b_2} (GeV)	QCD background (in fb) $bjjbZ$ y, p_T cuts	$bjjbZ$ All cuts	$bbjbZ$ y, p_T cuts	$bbjbZ$ All cuts	$bbbbZ$ y, p_T cuts	$bbbbZ$ All cuts
250	16790	27.304	255.41	2.7	81.01	1.92
500	16790	3.513	255.41	0.256	81.01	0.194
750	16790	0.958	255.41	0.031	81.01	0.057
1000	16790	0.2514	255.41	0.0052	81.01	0.008

Table 4.1: Signal and background c.s. at the 14 TeV LHC for the process $pp \to b_2 b_2 \to bZbZ$, and the discovery luminosity required ($\mathcal{L}_D$) in the semileptonic decay mode, for the benchmark masses and couplings shown in Table 3.1. The $bZbZ$ columns do not include b-tagging factors, BR($Z \to \ell\ell$) or BR($Z \to jj$), while $\mathcal{L}_D$ includes all these factors. $(bjjbZ)_{\rm tot}$ shows the total background (including electroweak and QCD) where the QCD background is computed using the channels detailed in the second table weighted by appropriate factors as explained in the text.

exchange contribution, with a coupling g_s. In Fig. 4.3(b) we show the discovery luminosity $\mathcal{L}_D$ at the 14 TeV LHC, in the $pp \to b_2 b_2 \to bZbZ \to b\ell\ell bjj$ channel after "All cuts", with BR($b_2 \to bZ$) $= 1/3$ assumed.

The dileptonic mode, *i.e.* when both Z's decay leptonically, is much cleaner since there is no QCD background, but the BR is smaller. Since we are limited by signal rate, we expect the luminosity required to be much bigger than for the semileptonic mode we have focussed on. The luminosity required for the dileptonic mode can easily be computed from the signal and background c.s. at the $bZbZ$ level given in Table 4.1 after multiplying the factor $\eta_b^2 \times (\mathrm{BR}_{Z\to\ell\ell})^2 \approx 0.0011$. One can also consider demanding only one b-tag rather than the two that we have, which will increase the signal rate, but so will the background, although the luminosity required may end up being lesser.

$b_2 b_2 \to bZbh$ **and other decay modes:**

Here we consider the channel $pp \to b_2 b_2 \to bZbh \to b\ell\ell bbb$ where a light Higgs dominantly decaying to bb pair with BR ≈ 1. We demand four b-tagged jets in the final state. For this, the c.s. multiplied by the branching fractions and b-tagging efficiency, will be about half the $bZbZ$ case shown in Table 4.1 and in Fig. 4.3(a). The dominant SM backgrounds will then be $bbbbZ$, which we have already computed for the $bZbZ$ channel and shown in Table 4.1. As we can see from this, for large M_{b_2}, the required luminosity will be signal-rate limited as it was in the previous case, and therefore the luminosity required will be about twice that needed for the $bZbZ$ case shown in Table 4.1 and in Fig. 4.3(b).

One could also consider the $bZtW$ or other combinations of decay modes of the b_2 pair, but we do not consider these here, as our main motivation is to focus on those decay-modes which help in revealing aspects of the vector-like nature of the b_2. Apart from the usual pair production of channel, a vectorlike b_2 can be produced through the two-body and three-body single production channels via the off-diagonal couplings $b_2 tW$, $b_2 bZ$ and $b_2 bh$. An exhaustive list of b_2 single production channels is given in Ref. [53]. Here we consider some of the important single production channels relevant at the LHC.

4.1.2 $pp \to b_2 Z, b_2 h$ processes

Following Ref. [99], we analyze here the $pp \to b_2 Z$ and $pp \to b_2 h$ single production processes which are initiated by the bg initial state as shown in Fig. 4.4. In Fig. 4.5(a) we

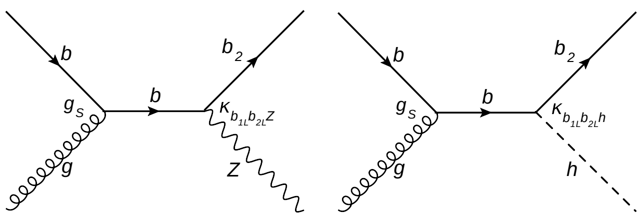

Figure 4.4: Sample partonic Feynman diagrams for $pp \to b_2 Z, b_2 h$ at the LHC.

show contours of the $pp \to b_2 Z$ c.s., after y and p_T cuts, in the $\kappa_{b_{1L} b_{2L} Z}$ vs M_{b_2} plane at the 14 TeV LHC. These cuts are applied after the $b_2 \to bZ$ decay, requiring $|y(b, Z)| < 2.5$ and $p_T(b, Z) > 0.1M_{b_2}$. The blue dots show the M_{b_2} and $\kappa_{b_{1L}b_{2L}Z}$ as given in Table 3.1.

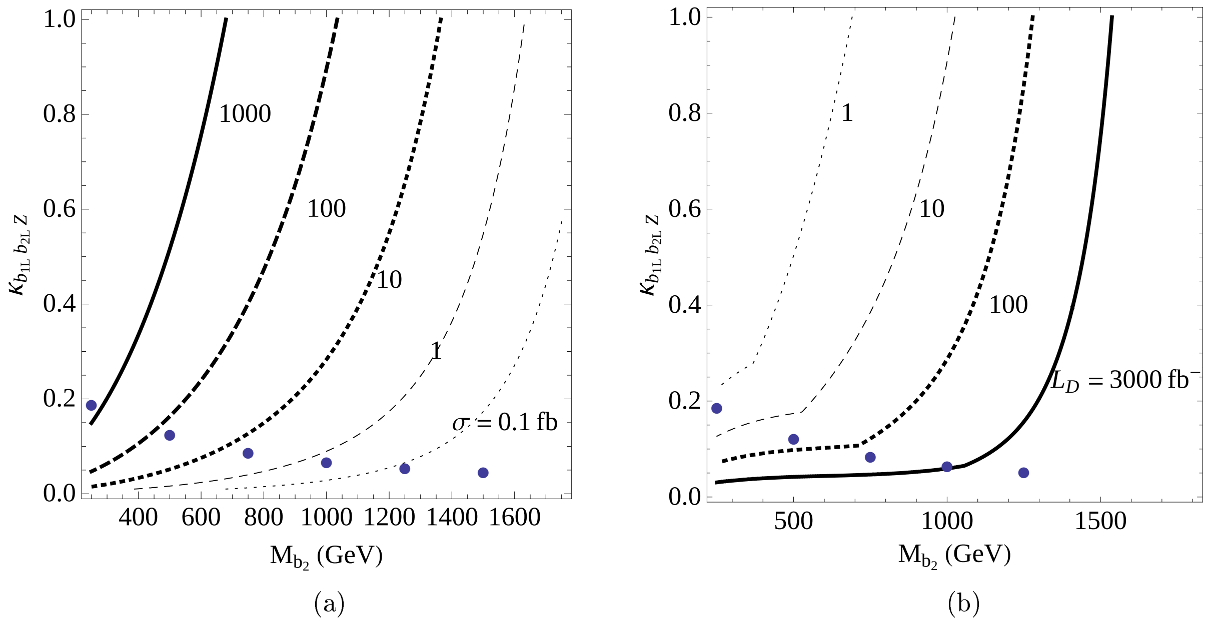

Figure 4.5: (a) Model-independent contours of the $pp \to b_2Z$ c.s. in fb after y and p_T cuts, and, (b) contours of the discovery luminosity-required $\mathcal{L}_D$ in the $pp \to b_2Z \to bZZ \to b\ell\ell jj$ channel after "All cuts", with the region to the left of a contour covered by that luminosity, and BR$(b_2 \to bZ) = 1/3$ assumed. These are for the 14 TeV LHC. The blue dots show the M_{b_2} and $\kappa_{b_{1L}b_{2L}Z}$ as given in Table 3.1.

The b_2h c.s. is expected to be similar to the $bg \to b_2Z$ case above. In the following, we consider the $b_2 \to bZ$, tW, or bh decay modes. For the bZh final state both $bg \to b_2h \to bZh$, and $bg \to b_2Z \to bhZ$ channels will contribute. We will discuss each of these channels later.

$bg \to b_2Z \to bZZ$ **channel:**

We will consider next, in turn, the semileptonic decay mode *i.e.* $bZZ \to bjj\ell\ell$, and, dileptonic decay mode *i.e.* $bZZ \to b\ell\ell\ell\ell$ channels.

Semileptonic decay mode: For the semileptonic $pp \to b_2Z \to bZZ \to bjj\ell\ell$ channel, we assume that the leptonically decaying Z is fully reconstructed, and perform our analysis at the $bjjZ$ level. We multiply the c.s. at the $bjjZ$ level by BR$(Z \to \ell\ell) \approx 0.066$. We could have indeed performed the analysis at the bZZ level, but because this channel will be limited by QCD background as we demonstrate below, we include the latter and perform the analysis at the $bjjZ$ level. We demand one tagged b-jet, and apply the following cuts:

- y and p_T cuts: (a) $|y(b, j, Z)| < 2.5$; (b) $p_T(b, j, Z) > 0.1 M_{b_2}$
- *Invariant mass cuts*: $|M(jj) - M_Z| < 10$ GeV; $|M(bZ)\ OR\ M(bjj) - M_{b_2}| < 0.05 M_{b_2}$

where Z means the leptonically decaying Z, and in the last invariant mass cut we accept the event if either of $M(bZ)$ *OR* $M(bjj)$ lies within the window. Here, j will exclude the b to avoid combinatorics issues with the three b's that will be present if the Z decays to bb. We ask that this not happen by demanding that the tagged-b is not among the two jets that reconstruct to the Z. We therefore multiply the signal $bjjZ$ and the electroweak background $(bjjZ)_{\rm EW}$ c.s. by $\eta_b \times {\rm BR}_{Z\to\ell\ell} = 0.033$ with $j = \{u, d, c, s\}$, where, we include the $Z \to bb$ decays that fail the b-tag. Since experimentally light-quark jets and gluon jets cannot be differentiated effectively, for the background, we take $j = \{g, u, d, c, s\}$, and in addition to the bZZ SM background for which the multiplicative factor is as shown above, we include the QCD backgrounds, namely,

$$(bjjZ)_{\rm QCD} = (bjjZ) + (1 - \eta_b)(bjbZ) + (1 - \eta_b)^2\ (bbbZ)\ , \tag{4.4}$$

where a $(1 - \eta_b)$ factor is included for a b-quark that fails to be tagged, and, we multiply these with an overall multiplicative factor of $\eta_b \times {\rm BR}_{Z\to\ell\ell}$. The signal and the background c.s. along with the discovery luminosity required for the semileptonic decay mode for various values of M_{b_2} and κ given in Table 3.1 are shown in Table 4.2. In the table, "All cuts" includes y, p_T cuts together with $M_{(bZ)\ OR\ (bjj)}$ invariant mass cut. The required luminosity for discovery for the semileptonic case is denoted as $\mathcal{L}_D^{\rm SL}$ which is always background limited.

In Fig. 4.5(b) we show the model-independent contours of the 14 TeV LHC luminosity-required for $5\,\sigma$ significance with at least 10 signal events in the $\kappa_{b_{1L} b_{2L} Z}$ – M_{b_2} plane.

The region to the left of a contour is covered by that luminosity. $\mathrm{BR}(b_2 \to bZ) = 1/3$ is assumed. The kinks seen is the cross-over from being background-limited at lower masses to signal-rate-limited at higher masses. The blue dots show the M_{b_2} and $\kappa_{b_{1L} b_{2L} Z}$ given in Table 3.1 for which Table 4.2 applies.

M_{b_2} (GeV)	signal σ_s (in fb)		background σ_b (in fb)				$\mathcal{L}_D^{\mathrm{SL}}$ (fb^{-1})
	$bjjZ$		$(bjjZ)_{EW}$		$(bjjZ)_{\mathrm{QCD}}$		
	y, p_T cuts	all cuts	y, p_T cuts	all cuts	y, p_T cuts	all cuts	
250	1017.66	995.86	77.03	10.33	7853.02	867.82	0.66
500	16.84	15.50	8.81	0.68	419.75	14.11	45.94
750	1.26	1.14	1.85	0.10	56.26	0.86	551.26
1000	0.14	0.12	0.47	0.01	12.38	0.05	3399.67

M_{b_2} (GeV)	QCD background (in fb)		
	$bjjZ$	$bjbZ$	$bbbZ$
250	546.36	634.32	17.19
500	10.14	7.76	0.35
750	0.52	0.66	0.03
1000	0.02	0.06	0.002

Table 4.2: Signal and background c.s. at the 14 TeV LHC for the $pp \to b_2 Z \to bZZ \to bjjZ$ channel with its charge-conjugate process also included. The discovery luminosity $\mathcal{L}_D^{\mathrm{SL}}$ is shown for the semileptonic decay modes corresponding to the benchmark masses and couplings shown in Table 3.1. The $bjjZ$ columns neither include b-tagging factors nor $\mathrm{BR}(Z \to \ell\ell)$, while $\mathcal{L}_D^{\mathrm{SL}}$ is shown after all these factors are included. $(bjjZ)_{\mathrm{QCD}}$ shows the total QCD background computed using the different channels detailed in the second table weighted by appropriate factors as explained in the text.

Dileptonic decay mode: For the channel $pp \to b_2 Z \to bZZ \to b\ell\ell\ell\ell$, we perform the analysis at the bZZ level and multiply the c.s. by $\eta_b \times \mathrm{BR}(Z \to \ell\ell)^2 \approx 0.002$. We apply the following cuts on the bZZ events:

- y and p_T cuts: (a) $|y(b, Z)| < 2.5$; (b) $p_T(b, Z) > 25$ GeV
- *Invariant mass cut*: $|M(bZ) - M_{b_2}| < 0.05 M_{b_2}$

where Z means either of the leptonically decaying Z, and in the invariant mass cut, M_{bZ} is evaluated for both the Z's with the event kept if either one of them falls within the window. We have relaxed the p_T cut here since we do not have to suppress the larger

QCD background that we had to contend with in the semileptonic case. The signal and background c.s. along with the luminosity required for the dileptonic decay mode for various values of M_{b_2} and κ given in Table 3.1 are shown in Table 4.3. As before, in the table, "All cuts" includes basic y, p_T cuts together with the $M_{(bZ)}$ invariant mass cut. The

M_{b_2} (GeV)	signal σ_s (in fb) bZZ		bkgrnd σ_b (in fb) bZZ		$\mathcal{L}_D^{\rm DL}$ (fb^{-1})
	y, p_T cuts	All cuts	y, p_T cuts	All cuts	
250	1119.42	1088.84	77	10.54	2.1
500	25.15	22.80	77	2.16	97.6
750	2.32	2.04	77	0.52	1091.9
1000	0.36	0.32	77	0.15	6962.4

Table 4.3: Signal and background c.s. at the 14TeV LHC for the $pp \to b_2 Z \to bZZ$ with its charge-conjugate process also included, and the luminosity required for the dileptonic decay mode corresponding to the benchmark masses and couplings shown in Table 3.1. The bZZ columns neither include b-tagging factors nor BR$(Z \to \ell\ell)$, while $\mathcal{L}_D^{\rm DL}$ includes all these factors.

required luminosity for the dileptonic case is always signal limited.

$bg \to b_2 Z \to tWZ$ **channel:**

M_{b_2} (GeV)	signal σ_s (in fb)		bkgrnd σ_b (in fb)	
	y, p_T cuts	All cuts	y, p_T cuts	All cuts
300	307.92	288.04	72.78	9.10
500	40.02	35.88	72.78	5.72
750	4.20	3.74	72.78	1.84
1000	0.70	0.62	72.78	0.64

Table 4.4: Signal and background c.s. for the $pp \to b_2 Z \to tWZ$ channel with the charge-conjugate process also included at the 14 TeV LHC. The κ are taken to be as given in Table 3.1.

In this case, at the tWZ level, the three particles in the final state are different, and therefore there is no combinatorial issue. For the semileptonic decay mode we have two possibilities, namely, when the Z decays leptonically and the W hadronically, and vice-versa. If the Z decays hadronically and the W leptonically, we have a neutrino in the final state, leading to missing energy. At a hadron collider, since the incoming parton energies are not known, this missing energy will prevent the full reconstruction of the event, but can only be done in the transverse plane. However, one can apply the W mass constraint in order to infer p_{ν_z} (upto a two-fold ambiguity) as explained in Ref. [104]. The signal and SM background at the tWZ level are shown in Table 4.4. The choice for all the cuts here is similar to the ones for the dileptonic bZZ case above. Since the tW decay mode is present for a chiral b_2 also, and our main motivation in this study is to expose the vector-like nature of the b_2 and have not determined the luminosity required.

$bg \to b_2 Z, b_2 h \to bZh$ **channel:**

We assume a light Higgs that dominantly decays to bb with BR ≈ 1, and the Z decaying leptonically, resulting in the $b\ell\ell bb$ channel. We demand three b-tagged jets in the final state. We perform the analysis at the bZh level and multiply the c.s. by $\eta_b^3 \times \text{BR}(Z \to \ell\ell)$, but for the QCD background which we take at the $bZbb$ level (multiplied by effectively the same factor since we have taken $h \to bb$ BR to be 1). The $bZbb$ background is the same as in the previous case given in Table 4.2. We show in Table 4.5 the signal and background c.s. and the luminosity required. The luminosity is signal-rate limited.

M_{b_2} (GeV)	signal σ_s (in fb)		background σ_b (in fb)				$\mathcal{L}_D$ (fb^{-1})
	bZh		bZh		$bbbZ$		
	y, p_T cuts	All cuts	y, p_T cuts	All cuts	y, p_T cuts	All cuts	
250	1093.10	1056.96	4.68	0.74	569.35	18.01	1.13
500	44.30	34.70	4.68	0.14	569.35	2.22	34.41
750	5.94	3.54	4.68	0.03	569.35	0.37	337.30
1000	1.44	0.58	4.68	0.01	569.35	0.03	2058.67

Table 4.5: Signal and background c.s. for the leptonic $pp \to b_2 Z + b_2 h \to bZh$ channel. The bZh and $bbbZ$ columns neither include b-tagging factors nor BR$(Z \to \ell\ell)$, while $\mathcal{L}_D$ includes all these factors. The κ are taken to be as given in Table 3.1.

We could perhaps gain in luminosity by only demanding one or two b-tags as opposed to the three we demand here, but then the QCD background may be too large. One could also consider the hadronic decay of the Z resulting in the $bbbjj$ channel, but the QCD background may be large. We have not considered those possibilities here.

4.1.3 $pp \to b_2 b Z$ process

We consider $pp \to b_2 b Z$ channel as a probe of the new physics coupling $\kappa_{b_2 b Z}$ involved in this process which includes two types of resonant production of the b_2 as described below and shown in Fig. 4.6.

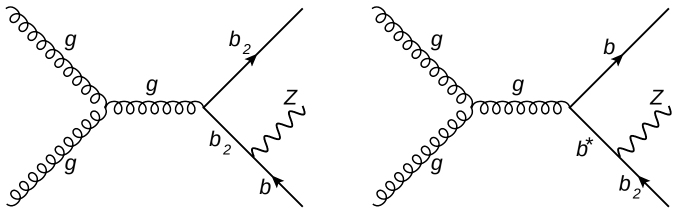

Figure 4.6: Sample partonic Feynman diagrams for $pp \to b_2 b Z$ process at the LHC. In (a) when both the b_2's are on-shell, we have a double resonant (DR) contribution, while when one of them is off-shell we have the single resonant (SR) process. The other contribution to the SR production coming from the strict single production diagram shown in (b).

- *Double resonant (DR) production:* pair production of b_2 where both b_2's are onshell followed by the decay of one b_2 to bZ leads to $b_2 b Z$ final state.
- *single resonant (SR) production:* this includes $b_2 b_2^* \to b_2 b Z$ (one of the b_2 is off-shell) and the strict single production of b_2 shown in Fig. 4.6(b).

The coupling $\kappa_{b_2 b Z}$ can be probed by isolating the SR contribution from the total $pp \to b_2 b Z$ events which includes DR and SR contributions. At the $b_2 b Z$ level to get sensitivity to couplings we isolate the SR contribution by applying only the following kinematical cut on the invariant mass $M(bZ)$,

$$|M(bZ) - M_{b_2}| \geq \alpha_{cut} M_{b_2} \quad (\text{with } \alpha_{cut} = 0.05) \ , \tag{4.5}$$

which ensures that the b quark and the Z do not reconstruct to an on-shell b_2, *i.e.* this cut removes the DR contribution. To obtain the SR c.s., σ_{SR}, the choice of α_{cut} is crucial [105].

It is dictated by the fact that we expect σ_{SR} to scale as $\kappa^2_{b_2bZ}$ whereas σ_{DR} is governed by g_s. Taking α_{cut} too small will spoil the scaling because of the contamination from the pair production, but it cannot be too large either as that will make the c.s. very small. In Table 4.6 we explicitly demonstrate that our choice of α_{cut} retains the $\kappa^2_{b_2bZ}$ scaling. We observe that before cut c.s. decreases with increasing κ_{b_2bZ} due to destructive interference.

$\kappa_{b_{2L}b_{1L}Z}$	σ_{b_2bZ} (fb) before cut	σ_{b_2bZ} (fb) after cut
0.05	239.37	2.613
0.10	238.91	11.10
0.15	236.31	24.17
0.20	233.52	41.95
0.25	229.40	62.48

Table 4.6: Scaling behavior of $pp \to b_2bZ$ single production c.s. at the 14 TeV LHC after the invariant mass cut defined in Eq. (4.18), for $M_{b_2} = 750$ GeV. Here we take $\kappa_{b_{2R}b_{1R}Z} = 0$.

Here we have in mind the $bb\ell\ell JJ$ channel (where J stands for either a light-jet or an untagged b-jet). To obtain the luminosity requirements, we multiply the cross-section obtained at the $bZbZ$ level by the factor

$$\eta_{b_2} = 2 \times \eta_b^2 \times \epsilon_{rec}^{(\ell\ell\to Z)} \times \epsilon_{rec}^{(JJ\to Z)} \times (BR_{Z\to JJ}) \times (BR_{Z\to\ell\ell}) \approx 0.023 \,, \tag{4.6}$$

to take into account the various BRs and efficiencies. Here $\epsilon_{rec}^{(\ell\ell\to Z)}$ and $\epsilon_{rec}^{(JJ\to Z)}$ stand for reconstruction efficiency of Z from $\ell\ell$ and JJ respectively. We take $\eta_b = 0.5$, $\epsilon_{rec}^{(\ell\ell\to Z)} = 1$ and $\epsilon_{rec}^{(JJ\to Z)} = 1$. The factor of two appears because either of the Z can decay to the $\ell\ell$ pair. In Fig. 4.7 we present the luminosity requirement for $pp \to b_2bZ$ SR production channel in a model-independent manner assuming $\mathrm{BR}_{b_2\to bZ}$ to be 100%. The kinks in the graphs appear because of the transition from $\mathcal{L}_5$ to $\mathcal{L}_{10}$ along the increasing values of the coupling parameter. We vary $\kappa_{b_{2L}b_{1L}Z}$ keeping the other coupling $\kappa_{b_{2R}b_{1R}Z}$ zero while computing model-independent SR contribution. This assumption is indeed a valid for the DT and TT models where $\kappa_{b_{2L}b_{1L}Z}$ dominates over $\kappa_{b_{2R}b_{1R}Z}$. The background is computed

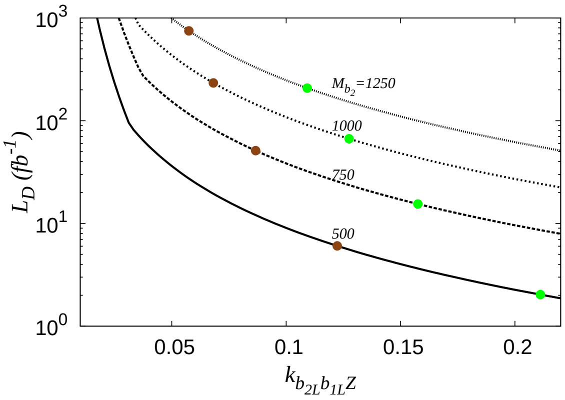

Figure 4.7: Discovery luminosity ($\mathcal{L}_D$) for observing the $pp \to b_2 bZ$ single production channel as functions of $\kappa_{b_{2L}b_{1L}Z}$ for different M_{b_2} at the 14 TeV LHC. Luminosity is computed after including all BR's and b-tagging efficiency. The green and brown dots correspond to the TT and DT models respectively.

at the $bZbZ$ level. We demand that any one of the bZ pairs satisfies the invariant mass cut of Eq. (4.5). The brown and green dots in Fig. 4.7 correspond to the DT and TT warped models respectively for the SR process.

M_{b_2} (GeV)	$\sigma_{pp \to b_2 Z}$ (fb)	$\sigma_{pp \to b_2 b}$ (fb)	$\sigma_{pp \to b_2 bZ}$ (fb)
500	81.50	15.86	47.12
750	16.67	3.910	11.10
1000	4.630	1.256	3.933
1250	1.534	0.472	1.722
1500	0.565	0.193	0.804

Table 4.7: SR production c.s. of b_2 for different M_{b_2} with $\kappa_{b_{2L}b_{1L}Z} = 0.1$ and $\kappa_{b_{2R}b_{1R}Z} = 0$ at the 14 TeV LHC. The $b_2 bZ$ c.s. is after applying the invariant mass cut of Eq. (4.5), while the others are without any cuts.

In Table 4.7 we compare the c.s. of various SR channels model-independently. The $b_2 bZ$ cross-section is after applying the invariant mass cut of Eq. (4.5), while the others are without any cuts. We see that the $b_2 Z$ channel studied earlier and the $b_2 bZ$ SR process studied here are comparable in signal c.s.. However, the latter case requires larger luminosity since the background is larger.

In the warped models, vectorlike b''s are present in the DT and TT models, and the κ's are shown in chapter 2. For the DT model in the $pp \to b'b' \to bZbZ \to b\ell\ell bjj$ channel,

DT model			TT model		
M_{b_2} (GeV)	$\kappa_{b_{1L}b_{2L}Z}$	σ_{b_2bZ} (fb)	$\mathcal{B}$	M_{b_2} (GeV)	σ_{b_2bZ} (fb)
500	0.122	70.49	$\mathcal{B}_1$	500	210.05
750	0.087	8.341	$\mathcal{B}_2$	750	27.56
1000	0.068	1.829	$\mathcal{B}_3$	1000	6.394
1250	0.057	0.569	$\mathcal{B}_4$	1250	2.054

Table 4.8: Cross-sections for the process $pp \to b_2bZ$ in the DT and TT models for different choices of M_{b_2} at the 14 TeV LHC. The cross-sections are obtained after applying the invariant mass cut of Eq. (4.5). The couplings for the TT model corresponding to the parameter sets labelled by $\mathcal{B}_i$ are shown in Table 3.2.

the 14 TeV LHC reach is about 1250 GeV with about 500 fb^{-1}. For the TT model, the BR($b' \to bZ$) is about a factor of two bigger compared to the DT model; hence the luminosity being signal-rate limited, is about 250 fb^{-1}. Turning next to the SR process, the brown and green dots in Fig. 4.7 are for the DT and TT warped models respectively. The corresponding signal c.s. are shown in Table 4.8. One can also look at the $bhbh$ channel which we have not explored in this work. In the TT model, for simplicity, we have focused only on the b_2 signatures, although the b_3 is almost degenerate; a more complete analysis can include the b_3 contributions also. In the DT model, for the choice of benchmark parameters discussed in chapter 3, we have a reach of $M_{b_2} = 1000$ GeV with about 250 fb^{-1}, and in the TT model it is about $M_{b_2} = 1250$ GeV with about 250 fb^{-1}.

4.1.4 Other Processes

Here we collect some processes that we have considered, but have not analyzed in full detail, since based on rough estimates we think that they may lead to a larger luminosity requirement compared to the ones we have considered in detail above. We give below some indication for what c.s. we expect for these processes for the benchmark points given in Table 3.1.

$pp \to b_2tW, b_2bh$ **processes:** These processes are similar to the $pp \to b_2bZ$ process and include contributions both from the DR and SR productions. Since the DR c.s. is much bigger than the SR c.s., the LHC reach of M_{b_2} in these channels are effectively determined by the DR contributions. We have already discussed the reach in subsection 4.1.1 using only DR contributions. In this thesis we have not estimated SR contributions of these channels by applying invariant mass cut on tW or bh pair.

$bq \to b_2 q$ **process:** For the process $bq \to b_2 q$, the signal is induced by the t-channel exchange of a Z boson. We find the signal c.s. to be small compared to the SM background. For example, for $M_{b_2} = 750$ GeV with couplings shown in table 3.1, the signal c.s. for $bQ \to b_2 q \to bZq \to b\ell\ell q$ is about 0.65 fb, which is about 40 times smaller than the background, which we have computed with an invariant mass cut of $|M(bZ) - M_{b_2}| \leq 25$ GeV.

$bq \to qb_2W, qb_2Z, qb_2h$ **and** $bg \to gb_2Z, gb_2h$ **processes:** The channels with a q in the final state proceed through bq initial state, and W and Z come from the initial quark line. The backgrounds are also bq initiated, and is potentially under control. But since these processes are qb initiated, rates might be much smaller compared to g initiated processes. The background is particularly small for $bq \to qb_2Z \to qbhZ$ since h has to attach to a b line which is suppressed by λ_b, the b-quark Yukawa coupling. Similar situation should also apply for the channel $bq \to qb_2h \to qbhh$. Since experimentally we cannot easily tell the difference between a light q and g, we should include $bg \to gb_2Z, gb_2h$ here, which will result in the same final state as the above processes.

We expect these 3-body final state processes in general to have smaller c.s. compared to the 2-body single productions or the SR (offshell) contributions considered earlier. For $M_{b_2} = 750\,GeV$ and b_2 decaying as $b_2 \to bZ$ the total signal strength is about 0.08 fb (which includes the charge conjugate process), with one of the Z decaying leptonically and the other decaying into light jets.

$qg \to qb_2b, qb_2t$ **processes:** These proceed via gZ and gW fusion respectively. Comparing to the $bg \to b_2Z$ process, we see that this is a 3-body final state which would suppress the c.s.. For $b_2 \to bh$, the $qbhb$ irreducible background should be small since it is suppressed by λ_b^2. But, the SM background will include processes in which the q is replaced by a g, which will mean that the background is gg initiated, and is likely to be much larger.

$qq \to b_2 b, b_2 t$ **processes:** The signal for the $b_2 b$ final state is small as this is a qq initiated process. For example, if we consider the b_2 decaying into a b and a Z with the Z decaying leptonically, the signal turns about 0.009 fb for $M_{b_2} = 750$ GeV. Moreover, the background, which has gg initiated contributions, is expected to be much bigger than the signal.

$gg \to b_2 b$ **and** $gb \to b_2 g$ **process:** These proceed via s-channel and t-channel Higgs exchange respectively, with an effective ggh vertex (top triangle diagram). We roughly estimate this contribution to be potentially bigger than the $\sigma(bg \to b_2 Z)$ we have considered earlier; however these channels are susceptible to the gg initiated SM background which is large, and therefore might lead to a larger luminosity required.

4.2 t' LHC Signatures

At the LHC, apart from the usual pair production channel, a charge 2/3 vectorlike t_2 (mass eigenstate) can be produced through the following single production channels via the off-diagonal couplings $t_2 bW$, $t_2 tZ$ and $t_2 th$:

$$pp \to t_2 W, t_2 b, t_2 t, t_2 bW, t_2 tZ, t_2 th \ . \tag{4.7}$$

Once produced the t_2 can decay to th, tZ and bW decay modes leads to various possible final states. Here we consider those channels which are dominant production channels of t_2 in the warped models discussed in chapter 2. In models where the $t_2 bW$ couplings is much smaller than the others (as for instance in the warped ST and TT models), we can ignore the single production of t_2 involving $\kappa_{t_2 bW}$ couplings, *i.e.* $t_2 W$, $t_2 b$ and $t_2 bW$ channels. We will mainly discuss $t_2 th$ process but comment on the other processes briefly.

4.2.1 $pp \to t_2 th$ process

Similar to the discussion for the $b_2 bZ$ process, here too we identify the DR and SR channels, and consider the $thth$ final state. As shown in Fig. 4.8, this includes (i) the DR pair-production $t_2 t_2$ (both on-shell) followed by the decay of one of the on-shell $t_2 \to th$, and, (ii) the SR channel including $t_2 t_2^*$ (one of the t_2 off-shell), and in addition, the strict single-production of t_2 shown in Fig. 4.8(b). We therefore include DR and SR and consider the process

$$pp \to t_2 th \to thth \to tbbtbb \ , \tag{4.8}$$

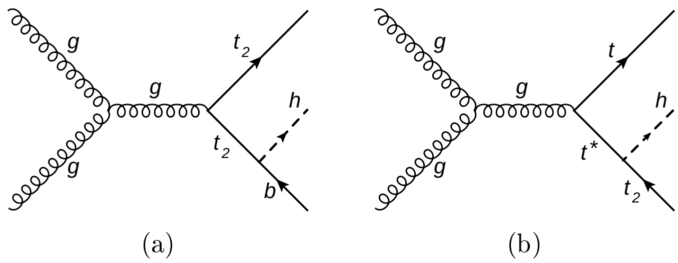

Figure 4.8: Sample partonic Feynman diagrams for $pp \to t_2 th$ process at the LHC. In (a) when both the t_2 are on-shell, we have a DR contribution, while when one of them is off-shell we have the SR process. The other contribution to the SR production coming from the single production diagram shown in (b).

and focus on the $6\ b + 4\ j$ final-state, where j includes only light jets. We obtain the cross-sections at the $tbbtbb$ level and multiply by appropriate BRs relevant to the above final state. We take the Higgs boson mass to be 125 GeV in all our computations. We assume b-tagging efficiency $\eta_b = 0.5$, and demand only four of the six b-jets to be b-tagged (Ref. [106] also follows a similar approach) to get a better signal rate. We require the two top-quarks to be reconstructed from two b-tagged jets and four J (where J stands for either a light-jet or an untagged b-jet) and then the two h to be reconstructed from the remaining two b-tagged jets and two J. Here we do not deal with any complications of combinatorics. We compute the signal and the background cross-sections at the $ttbbJJ$

level since there could be potentially other sources of background. However, due to requiring the four jets to reconstruct to the two h by applying the invariant mass cuts, the SM QCD contribution to the $pp \to ttbbJJ$ process becomes negligible and the dominant SM background contribution comes from the $pp \to tthh$ process. We require a minimum angular separation between any two jets

$$\Delta R(ij) = \sqrt{\Delta\phi_{ij}^2 + \Delta\eta_{ij}^2}\,, \tag{4.9}$$

where ϕ is the azimuthal angle and η is the pseudo-rapidity. To optimize the signal and get rid of the background, we identify the following cuts:

1. **Basic**

   (a) $|y(J)| \leq 2.5$

   (b) $\Delta R(JJ) \geq 0.4$

   (c) $p_T(J) \geq 25$ GeV

2. **Discovery**

   (a) $|y(J)| \leq 2.5$

   (b) $\Delta R(JJ) \geq 0.4$

   (c) For p_T ordered jets:
   $p_T^{1st}(J), p_T^{2nd}(J) \geq 175$ GeV and $p_T^{3rd}(J), p_T^{4th}(J) \geq 25$ GeV

   (d) $|M(J_i, J_j) - m_h| \leq 10$ GeV and $|M(J_k, J_l) - m_h| \leq 10$ GeV where $i \neq j \neq k \neq l$.

The second set of cuts is our "discovery cut" motivated by the fact that for the signal, there is at least one high-p_T Higgs coming from the heavy t_2 decay, and we expect the b-quarks coming from the Higgs decay to have a large p_T. We multiply both signal and background cross sections with a factor

$$\eta_{t_2} = \eta_b^4 \times (\epsilon_{rec}^W)^2 \times (\epsilon_{rec}^t)^2 \times (BR_{W\to jj})^2 \approx 0.0299\ . \tag{4.10}$$

In the warped models detailed in chapter 2, the t_2bW couplings (i.e. κ_{t_2bW}) become very small for heavy t_2 as explained in chapter 3. As a result, the production c.s. for the $pp \to t_2W, t_2b, t_2bW$ channels are small compared to the rest of the single production channels. Among the other channels, the $pp \to t_2t$ channel is weak interaction mediated [2] (the t_2t pair actually comes from an off-shell Z or h) and so is less significant than the $pp \to t_2tZ$ or $pp \to t_2th$ channels, and we do not consider the former due to the small $\text{BR}_{Z\to\ell\ell}$. Thus in the warped models, the $pp \to t_2th$ channel that we have focused on is a promising channel. As already mentioned, the t_2 in the warped model without $Zb_L\bar{b}_L$ protection (DT model) is very heavy making its discovery very challenging. We, therefore, do not consider further the t' in the DT model. The κ's in the warped models with $Zb\bar{b}$ protection (ST and TT models) are given in chapter 2. We present our results for the ST model at the 14 TeV (8 TeV) LHC in Table 4.9 (Table 4.10) after the cuts shown above. We find that $\mathcal{L}_{5\sigma} < \mathcal{L}_{10}$ in most of parameter-space, except for $M_{t_2} = 1250$ GeV for 14 TeV LHC, and we present the maximum of $\mathcal{L}_{5\sigma}$ and $\mathcal{L}_{10}$ in Table 4.9. From $\sigma_{tot} = \sigma_{DR} + \sigma_{SR}$, we find that the 14 TeV LHC can probe M_{t_2} of the order of 1 TeV with 100 fb^{-1} of integrated luminosity in the ST model.

$\mathcal{T}$	M_{t_2} (GeV)	σ_{tot} (fb)	σ_{SR} (fb)	cuts	S (fb)	BG (fb)	$\mathcal{L}$ (fb^{-1})
$\mathcal{T}_1$	500	1207	223.0	Basic	237.4	102.7	-
				Disc.	52.38	0.389	6.379
$\mathcal{T}_2$	750	115.2	18.30	Basic	22.67	102.7	-
				Disc.	13.25	0.389	25.22
$\mathcal{T}_3$	1000	18.38	2.715	Basic	3.088	102.7	-
				Disc.	2.421	0.389	138.0
$\mathcal{T}_4$	1250	3.821	0.590	Basic	0.477	102.7	-
				Disc.	0.415	0.389	1889.2

Table 4.9: Signal (S) and background (BG) cross sections (in fb) for $pp \to t_2th \to ttbbbb$ channel at the 14 TeV LHC for the ST model. The $\mathcal{T}_i$'s correspond to the parameter sets detailed in Table 3.3. The luminosity requirement $\mathcal{L}$ is computed using σ_{tot} after including the factor η_{t_2} defined in Eq. (4.10). These numbers are obtained using $BR_{h\to bb} = 0.8$. The $\sigma_{tot} = \sigma_{DR} + \sigma_{SR}$ is computed at the t_2th level with no cut applied, whereas σ_{SR} is computed at the t_2th level with only the tW invariant mass cut of Eq. (4.11) applied.

[2]However, this could also arize from the decay of the KK Gluon; see Ref. [46].

$\mathcal{T}$	M_{t_2} (GeV)	σ_{tot} (fb)	σ_{SR} (fb)	cuts	S (fb)	BG (fb)	$\mathcal{L}$ (fb^{-1})
$\mathcal{T}_1$	500	175.3	32.48	Basic	35.83	16.43	-
				Disc.	6.702	0.035	49.85
$\mathcal{T}_2$	750	11.30	1.690	Basic	2.353	16.43	-
				Disc.	1.325	0.035	252.3
$\mathcal{T}_3$	1000	1.111	0.168	Basic	0.206	16.43	-
				Disc.	0.162	0.035	2056.8

Table 4.10: Same as in Table 4.9 for the 8 TeV LHC.

As mentioned earlier, the SR process can give important information on the electroweak couplings κ (while the DR depends dominantly on g_S). To explore this aspect, we compute the $pp \to t_2 th$ SR production cross-sections from the $pp \to t_2 th$ signal events by applying the kinematical cut

$$|M(th) - M_{t_2}| \geq \alpha_{cut} M_{t_2};\ \alpha_{cut} = 0.05\ . \tag{4.11}$$

Just as in the case of b_2 production, for the parameter ranges we are interested in, $pp \to t_2 th$ process is dominated by the DR production. We have also verified that with our choice of α_{cut} the σ_{SR} scales as $\kappa^2_{t_2 th}$. Since the SR production can give us information about the off-diagonal $t_2 th$ coupling, in Fig. 4.9 we present model-independently the luminosity required for $pp \to t_2 th$ SR production channel assuming $BR_{t_2 \to th}$ to be 100%. In doing this we vary $\kappa_{t_{2L} t_{1R} h}$ keeping the other coupling $\kappa_{t_{1L} t_{2R} h}$ to zero (as is the case for instance in the warped-model). The background is computed at the $thth$ level after demanding that any one of the th pairs satisfies the invariant mass cut defined in Eq. (4.11). We find that $pp \to t_2 th$ events are signal rate limited (*i.e.*, $\mathcal{L}_{10} > \mathcal{L}_5$) in the parameter range we have considered. In Fig. 4.9 we show the luminosity required for the warped ST model as blue dots and the TT model as green dots.

In the ST or TT models, for heavy t_2, the branching ratios for $t_2 \to th$ and $t_2 \to tZ$ are comparable, *i.e.*,

$$\mathrm{BR}_{t_2 \to th} \approx BR_{t_2 \to tZ}\ . \tag{4.12}$$

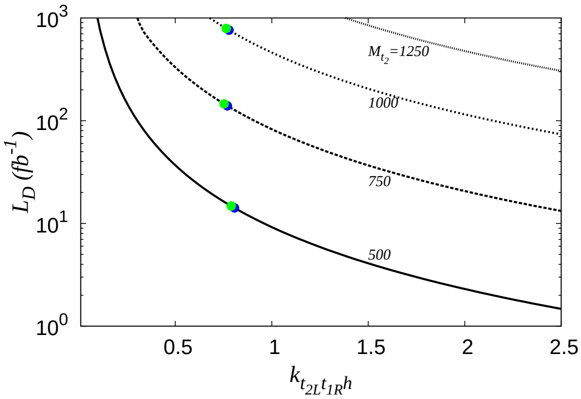

Figure 4.9: Luminosity requirements ($\mathcal{L}_D$, in fb^{-1}) for observing the $pp \to t_2th$ SR process as functions of $\kappa_{t_{2L}t_{1R}h}$ for different M_{t_2} (in GeV) at the 14 TeV LHC. The luminosity is computed after including all BRs and b-tagging efficiency. The blue and green dots correspond to the ST and TT models respectively.

Hence, one could as well study the following processes:

$$pp \to t_2th \to (tZ)th \to bWZbWh \ , \tag{4.13}$$

$$pp \to t_2tZ \to (th)tZ \to bWhbWZ \ , \tag{4.14}$$

$$pp \to t_2tZ \to (tZ)tZ \to bWZbWZ \ . \tag{4.15}$$

Of these the first two can even lead to $4b+6j$ final states which is exactly what we have used for our analysis by demanding only 4 b-tagged jets. We do not expect the LHC reach to be very different for these two channels from what we have estimated. This is because, the main difference between these two channels and what we have considered comes from the facts that the Higgs boson is a bit heavier than the Z and $\mathrm{BR}_{h\to bb} > \mathrm{BR}_{Z\to JJ}$. However for the last process, *i.e.* $pp \to t_2tZ \to (tZ)tZ$, we cannot demand 4 b-tagged jets anymore and as a result we consider one of the Z decaying leptonically to act as the trigger. Since $\mathrm{BR}_{Z\to \ell\ell} < \mathrm{BR}_{Z\to JJ}$, in this case the signal rate will be quite small.

4.2.2 χ LHC Signatures

We assume that the only decay is $\chi \to tW$, which is the case in many BSM scenarios. At the LHC, we consider the χtW production process as we find this to be the dominant χ production channel. As shown in Fig. 4.10, this includes (i) the DR pair-production $\chi_1\chi_1$ (both on-shell) followed by the decay of one of the on-shell χ to tW, and, (ii) the SR channel including $\chi_1\chi_1^*$ (one of the χ off-shell), and in addition, the strict single-production of χ_1 shown in (b). We include both DR and SR and focus on the channel

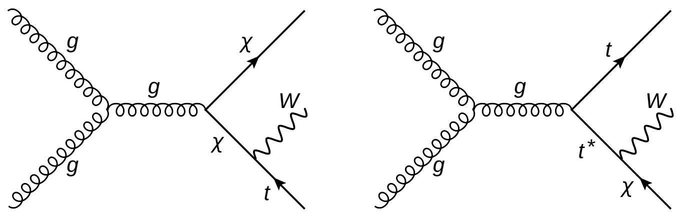

(a) (b)

Figure 4.10: Sample partonic Feynman diagrams for $\chi_1 tW$ process at the LHC. In (a) when both the χ are on-shell, we have a DR contribution, while when one of them is off-shell we have the SR process; the other contribution to SR coming from the single production diagram shown in (b).

$$pp \to \chi_1 tW \to tWtW \to tWt\ell\nu\,. \tag{4.16}$$

We obtain the signal and background cross-sections at the $ttW\ell\nu$ level i.e., only one W decays leptonically. We perform our analysis at this level because for the signal we expect the lepton coming from the W to have large p_T, whereas it is less probable for the background to have a high p_T lepton. This feature of the lepton can be used to isolate the signal from the background. The lepton can be used as a trigger. We consider the $2b\ 6j\ \ell \not{E}_T$ final state where j includes only "light" jets (u, d, c, s) and ℓ includes e and μ. From the $tWt\ell\nu$ level cross-section, we compute the rate for the final-state of interest by multiplying with appropriate branching ratios.

In order to select the signal while suppressing the background, we apply the following "basic" and "discovery" cuts and present the signal and the background cross sections in

Table 4.12 (Table 4.13) for the 14 TeV (8 TeV) LHC:

1. **Basic**: $|y(\ell)| \leq 2.5$; $p_T(\ell) \geq 10$ GeV.

2. **Discovery**: $|y(\ell)| \leq 2.5$; $p_T(\ell) \geq 125$ GeV; $p_T(W) \geq 250$ GeV.

The second set of cuts is chosen to optimize the signal over background ratio. It is our "discovery" cut motivated by the fact that in the signal, there are two high-p_T W's present at the $ttWW$ level and one of them decays to a high-p_T lepton. To account for the various efficiencies we multiply both signal and background cross sections with a factor

$$\eta_{\chi_1} = \eta_b^2 \times (\epsilon_{rec}^W)^3 \times (\epsilon_{rec}^t)^2 \times (BR_{W \to jj})^3 \approx 0.082 \,, \tag{4.17}$$

where η_b is the b-tagging efficiency, ϵ_{rec}^W is the W reconstruction efficiency from jj, ϵ_{rec}^t is the t reconstruction efficiency from bW. Combinatorics might be an important issue for reconstruction but at our level of analysis we ignore this complication. We take $\eta_b = 0.5$, $\epsilon_{rec}^t = 1$, $\epsilon_{rec}^W = 1$ and $W \to jj$ branching ratio $\mathrm{BR}_{W\to jj} = 0.69$. As explained earlier, we then compute $\mathcal{L}_5$ and $\mathcal{L}_{10}$, and the larger of $\mathcal{L}_5$ and $\mathcal{L}_{10}$ is the discovery luminosity.

The κ can be probed by isolating the SR contribution. At the $\chi_1 tW$ level we isolate the SR contribution by applying only the kinematical cut on the invariant mass $M(tW)$,

$$|M(tW) - M_{\chi_1}| \geq \alpha_{cut} M_{\chi_1}; \; \alpha_{cut} = 0.05, \tag{4.18}$$

which ensures that the t quark and the W do not reconstruct to an on-shell χ_1, i.e. this cut removes the DR contribution. To obtain the cross section, σ_{SR}, the choice of α_{cut} is crucial [105]. It is dictated by the fact that we expect σ_{SR} to scale as $\kappa^2_{\chi_1 tW}$ whereas σ_{DR} is dictated by g_s. Taking α_{cut} too small will spoil the scaling because of the contamination from the pair production (but it cannot be too large either as that will make the cross section very small). In Table 4.11 we explicitly demonstrate that our choice of α_{cut} retains the $\kappa^2_{\chi_1 tW}$ scaling.

For all M_χ considered here, we find $\mathcal{L}_5 < \mathcal{L}_{10}$, and therefore in Table 4.12 we present

$\kappa_{\chi_{1R}t_{1R}W}$	$\sigma_{pp\to\chi_1 tW}$ (fb) before cut	$\sigma_{pp\to\chi_1 tW}$ (fb) after cut
0.05	239.37	4.945
0.10	238.91	21.09
0.15	236.31	45.92
0.20	233.52	79.71
0.25	229.40	118.71

Table 4.11: Scaling behavior of $pp \to \chi_1 tW$ single production cross sections after the invariant mass cut defined in Eq. (4.18), for $M_\chi = 750$ GeV.

$\mathcal{X}$	M_χ (GeV)	σ_{tot} (fb)	σ_{SR} (fb)	cuts	S (fb)	BG (fb)	$\mathcal{L}$ (fb^{-1})
$\mathcal{X}_1$	500	2406	261.5	Basic	977.5	3.257	-
				Disc.	146.1	0.115	0.826
$\mathcal{X}_2$	750	235.5	29.31	Basic	99.99	3.257	-
				Disc.	42.74	0.115	2.824
$\mathcal{X}_3$	1000	39.19	5.198	Basic	17.92	3.257	-
				Disc.	11.36	0.115	10.63
$\mathcal{X}_4$	1250	8.576	1.231	Basic	4.305	3.257	-
				Disc.	3.226	0.115	37.42
$\mathcal{X}_5$	1500	2.188	0.364	Basic	1.235	3.257	-
				Disc.	1.010	0.115	119.5
$\mathcal{X}_6$	1750	0.613	0.121	Basic	0.393	3.257	-
				Disc.	0.339	0.115	355.8

Table 4.12: Signal (S) and background (BG) cross sections (in fb) for $pp \to \chi tW \to ttW\ell\nu$ channel at the 14 TeV LHC for the ST model. The $\mathcal{X}_i$'s correspond to the parameter sets detailed in Table 3.4. The luminosity requirement ($\mathcal{L}$) is computed using σ_{tot} after including the factor η_{χ_1} defined in Eq. (4.17). The σ_{tot} is computed at the $\chi_1 tW$ level with no cut applied. σ_{SR} is computed at the χtW level with only an invariant mass cut applied on tW as defined in Eq. (4.18).

$\mathcal{X}$	M_χ (GeV)	σ_{tot} (fb)	σ_{SR} (fb)	cuts	S (fb)	BG (fb)	$\mathcal{L}$ (fb^{-1})
$\mathcal{X}_1$	500	351.6	36.63	Basic	144.0	0.622	-
				Disc.	18.40	0.011	6.560
$\mathcal{X}_2$	750	23.11	2.741	Basic	9.927	0.622	-
				Disc.	4.103	0.011	29.42
$\mathcal{X}_3$	1000	2.362	0.315	Basic	1.092	0.622	-
				Disc.	0.680	0.011	177.5
$\mathcal{X}_4$	1250	0.290	0.042	Basic	0.147	0.622	-
				Disc.	0.109	0.011	1105

Table 4.13: Same as in Table 4.12 for the 8 TeV LHC.

only $\mathcal{L}_{10}$. From Table 4.12 we find that using σ_{tot}, i.e. including both SR and DR, the 14 TeV LHC can probe M_{χ_1} up to 1.5 TeV (1.75 TeV) with 100 fb^{-1} (300 fb^{-1}) of integrated luminosity for the ST model. The numbers in Table 4.12 show that for the parameter ranges we are interested in, the $pp \to \chi_1 tW$ process is dominated by the DR production. Hence, we do not display the cross sections and discovery luminosity separately for the TT model as the difference between them is only due the SR production (which depends on the $\kappa_{\chi_1 tW}$ coupling).

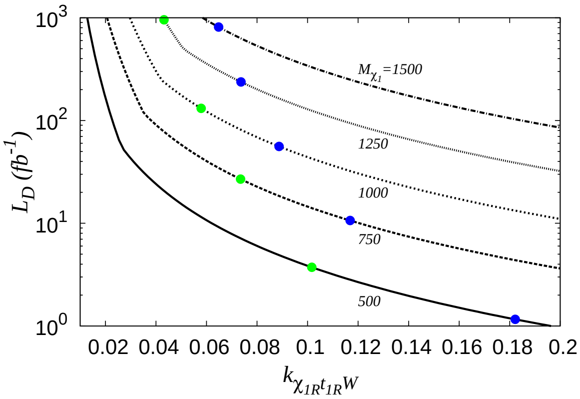

Figure 4.11: Luminosity requirements ($\mathcal{L}_D$, in fb^{-1}) for observing the $pp \to \chi_1 tW$ SR channel as functions of $\kappa_{\chi_{1R}t_{1R}W}$ for different M_{χ_1} (in GeV) at the 14 TeV LHC. $\mathcal{L}_D$ is computed after including all BRs and b-tagging efficiency. The blue and green dots correspond to the ST and TT models respectively.

As mentioned, the κ can be probed by isolating the SR contribution. To present our results model-independently such that it is useful for other models with a χtW coupling, we show in Fig. 4.11 the luminosity requirement ($\mathcal{L}_D$) to observe the $pp \to \chi_1 tW$ SR production process assuming the $\chi_1 \to tW$ BR to be 100%. The blue and green dots show the reach for the SR process for the warped ST and TT models respectively. Although we compute $\mathcal{L}_D$ at the χtW level multiplied by the appropriate BRs, with only the invariant mass cut of Eq. (4.18), we expect that the inclusion of the full decays and the basic and discovery cuts should change $\mathcal{L}_D$ only by a small amount. Here we vary $\kappa_{\chi_{1R}t_{1R}W}$ keeping the other coupling $\kappa_{\chi_{1L}t_{1L}W}$ zero (since this is the case in the ST and TT models). The plot will look identical if we instead vary $\kappa_{\chi_{1L}t_{1L}W}$ keeping $\kappa_{\chi_{1R}t_{1R}W} = 0$. The background is computed at the $tWtW$ level after demanding that any one of the tW pair satisfies the cut defined in Eq. (4.18). The kinks in the graphs appear because of the transition from $\mathcal{L}_5$ to $\mathcal{L}_{10}$ along the increasing values of the coupling. For getting the SR reach in the warped model, Tables 4.12 and 4.13 give the SR cross-section σ_{SR} for the ST model.

Finally, we note that there is another single production channel for χ_1 at the LHC, namely, the $W^\pm$ mediated $pp \to \chi_1 t$. However, unlike the $pp \to \chi_1 tW$ process this is an electroweak process due to which we find its cross-section to be much smaller. Also, we expect $\sigma(\chi_2\chi_2) < \sigma(\chi_1\chi_1)$ due to the larger M_{χ_2}, and since already the χ_1 pair-production is signal rate limited, we do not explore the χ_2 production and the subsequent $\chi_2 \to \chi_1 h$ or $\chi_2 \to \chi_1 Z$ channels.

Chapter 5

Color Octet Electrons at the LHC

In this chapter we study the LHC discovery potential for a generic color octet partner of charged lepton, namely the color octet electron, e_8. Although, here we consider only the e_8, our results are applicable for the color octet partner of muon, *i.e.*, μ_8 also. In Sec. 5.1 we briefly discuss some preonic models of quark-lepton compositeness in which e_8's are present. In Sec. 5.2 we display the interaction Lagrangian of a generic e_8 and compute its decay width. In Sec. 5.3 we explore different production (including pair and single) channels of e_8's in the context of the LHC. We have identified a new set of single production diagrams whose contribution is comparable to other dominant production channels of the e_8. A common feature in all the resonant production channels of the e_8 is the presence of two high-p_T electrons and at least one high-p_T jet in the final state. Using this feature, we implement a search method where the signal is a combination of pair and single production events. In Sec. 5.4 we compute the LHC reach for e_8 using this combined events. We show that this method has potential to increase the LHC reach significantly. We have also used our method to set limit on the compositeness scale.

5.1 Preon models of compositeness

In this section we present some motivating examples of preon models of composite leptons in which color octet leptons are present. These models assume that the SM particles may not be fundamental, and just as the proton has constituent quarks, they are actually bound states of substructural constituents called preons [60]. These constituents are visible only beyond a certain energy scale known as the compositeness scale. A typical consequence of quark-lepton compositeness is the appearance of colored particles with nonzero lepton numbers (leptogluons, leptoquarks) and excited leptons etc. Some composite models naturally predict the existence of color octet fermions with nonzero lepton numbers [60–66]. It is assumed that preons are either fermion or scalar and they are color triplet under $SU(3)_c$. Here we describe two preonic models just to show how color octet lepton arises in compositeness models of leptons.

Fermion-scalar model: In the fermion-scalar models [65, 107–109], leptons are bound states of one fermionic preon (F) and one scalar anti-preon ($\bar{S}$), and quarks are bound states of one fermionic anti-preon ($\bar{F}$) and one scalar anti-preon. In group theoretic language, color decomposition of the tensor product of one color triplet and one color anti-triplet can be written as

$$\begin{aligned} \ell &= (F\bar{S}) \equiv 3 \otimes \bar{3} \equiv 1 \oplus 8 \\ q &= (\bar{F}\bar{S}) \equiv \bar{3} \otimes \bar{3} \equiv 3 \oplus \bar{6} \; . \end{aligned} \tag{5.1}$$

Three-Fermion model: In the three fermion models [63, 64], leptons are assumed to be a bound state of three fermionic preons, and quarks are bound states of two fermionic preons and one fermionic anti-preon . The color decomposition of the tensor products of three color triplets can be written as

$$\ell = (FFF) \equiv 3 \otimes 3 \otimes 3 \equiv 1 \oplus 8 \oplus 8 \oplus 10$$
$$q = (F\bar{F}F) \equiv 3 \otimes \bar{3} \otimes 3 \equiv 3 \oplus \bar{3} \oplus \bar{6} \oplus 15 \ . \tag{5.2}$$

In the above two decompositions of lepton, we identify "1" as the SM lepton and the "8" as the color octet partner of the SM lepton. In the "three-fermion" model "10" is the decouplet partner of the SM lepton. Similarly, we identify "3" as the SM quark and "$\bar{3}$", "$\bar{6}$" and "15" as the exotic partners of the SM quarks. The full $SU(2)_L \otimes U(1)_Y$ structure of the preonic models can be found in Refs. [63–65, 107–109]. In this thesis we restrict ourselves in the lepton sector, in particular we focus on the LHC phenomenology of e_8 in a model independent fashion.

5.2 The Lagrangian of e_8

We write the Lagrangian of e_8 in a model independent manner. Assuming lepton flavor conservation, we consider a general Lagrangian for the e_8 including terms allowed by the gauge symmetries of the SM,

$$\mathcal{L} = \bar{e}_8^a i\gamma^\mu \left(\partial_\mu \delta^{ac} + g_s f^{abc} G_\mu^b\right) e_8^c - M_{e_8} \bar{e}_8^a e_8^a + \mathcal{L}_{int} \ . \tag{5.3}$$

In this thesis, we have ignored the interaction terms of the color octet partners of neutrinos and also all the terms involving electroweak interactions. Presence of these interactions could potentially affect the EWPT observables and experimental limits on those observables can be used to indirectly constraint the theory. But, in this thesis we are more interested to probe e_8 directly at the LHC in a model independent way. Therefore, we focus on the dominant lowest dimensional interactions which are relevant for the production of e_8 at the LHC. The interaction part ($\mathcal{L}_{int}$) contains all the higher-dimensional operators. We consider only the following dominant mass dimension-5 terms that contain the interactions between the SM electrons and the color octet ones [78] and neglect all the higher dimensional (dimension-6 and above) interactions [1],

$$\mathcal{L}_{int} = \frac{g_s}{2\Lambda} G^a_{\mu\nu} \left[\bar{e}^a_8 \sigma^{\mu\nu} \left(\eta_L e_L + \eta_R e_R \right) \right] + \mathrm{H.c.} \ . \tag{5.4}$$

Here $G^a_{\mu\nu}$ is the gluon field strength tensor, Λ is the scale below which this effective theory is valid and $\eta_{L/R}$ are the left/right couplings. Chirality conservation implies the product of η_L and η_R should be zero [78], and therefore we assume $\eta_L = 1$ and $\eta_R = 0$ in our analysis.

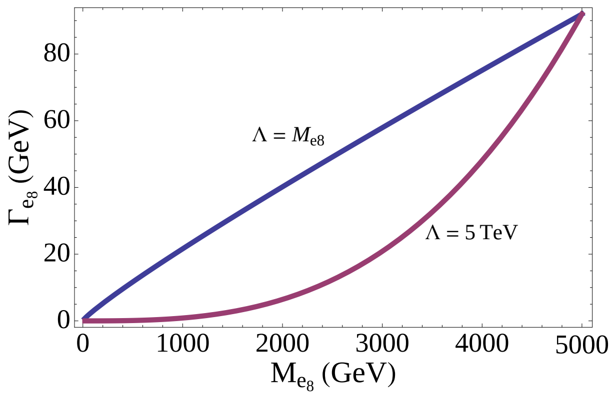

Figure 5.1: Decay width of e_8 as functions of M_{e_8} for $\Lambda = M_{e_8}$ and $\Lambda = 5$ TeV.

From the interaction Lagrangian given in Eq. (5.4) we see that an e_8 can decay to a gluon and an electron (two-body decay mode), *i.e.*, $e_8 \to eg$. With $\eta_L = 1$ and $\eta_R = 0$, the decay width of e_8 can be written as,

$$\Gamma_{e_8} = \frac{\alpha_s(M_{e_8}) M^3_{e_8}}{4\Lambda^2} \ , \tag{5.5}$$

In Fig. 5.1 we show the decay width of e_8 as functions of M_{e_8} with $\Lambda = M_{e_8}$ and $\Lambda = 5$

[1] There are actually more dimension five operators allowed by the gauge symmetries and lepton number conservation like,

$$\frac{\mathcal{C}_8}{\Lambda} i f^{abc} \bar{e}^a_8 G^b_{\mu\nu} \sigma^{\mu\nu} e^c_8 + \frac{\mathcal{C}_1}{\Lambda} \bar{e}^a_8 B_{\mu\nu} \sigma^{\mu\nu} e^a_8 \ .$$

These terms lead to momentum dependent $e_8 e_8 V$ vertices (form factors). Moreover, the octet term can lead to a $e_8 e_8 gg$ vertex which can affect the production c.s. We assume the unknown coefficients associated with these terms are negligible.

TeV. We use NLO α_s to compute the decay width.

5.3 Production at the LHC

In this section we discuss various production mechanisms of e_8's at the LHC and present the production c.s. for different channels. To obtain the c.s., we have implemented the Lagrangian of Eq. (5.3) in FeynRules version 1.6.0 [110] to generate Universal FeynRules Output (UFO) [111] format model files suitable for MadGraph5 [112] that we have used to compute c.s. We have used CTEQ6L PDFs [103] for all our numerical computations.

At a hadron collider like the LHC, resonant productions of e_8's can occur via gg, gq and qq initiated processes where q can be either a light quark or a bottom quark. The gluon PDF dominates at low x region whereas the quark PDFs take over at high-x region. Thus, depending on M_{e_8}, all of the gg, gq and qq initiated processes can contribute significantly to the production of e_8's at the LHC.

For the resonant production e_8's at colliders, two separate channels are generally considered in the literature – one is the pair production [74, 75] and the other is the single production of e_8 [70–73, 76]. In general, pair production of a colored particle is considered mostly model independent. This is because the universal strong coupling constant g_s controls the dominant pair production processes unlike the single production processes where the c.s. depends more on various model parameters like couplings and scales etc. However, as we shall see, for e_8's, the t-channel electron exchange diagrams can contribute significantly to the pair production making it more model dependent.

5.3.1 Pair Production ($\mathbf{gg, qq \rightarrow e_8 e_8}$)

At the LHC, pair production of e_8's is gg or qq initiated, see Fig. 5.2 where we have shown the parton level Feynman diagrams for this channel. Of these, only the electron exchange diagram, shown in Fig. 5.2(d), contains the Λ dependent gee_8 vertex. In Fig. 5.3 we show the $pp \rightarrow e_8 e_8$ c.s. as functions of M_{e_8} for two different choices of Λ, $\Lambda = M_{e_8}$ and

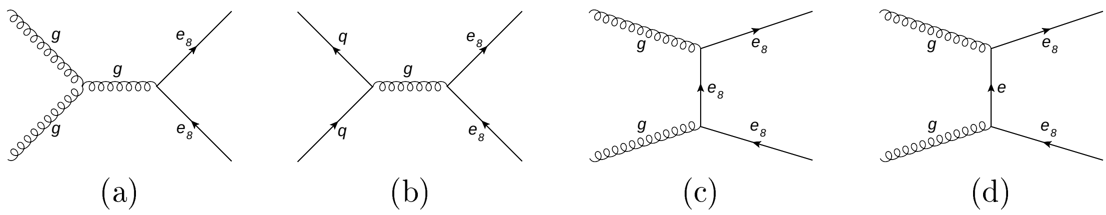

Figure 5.2: Parton level Feynman diagrams for $pp \to e_8 e_8$ process at the LHC.

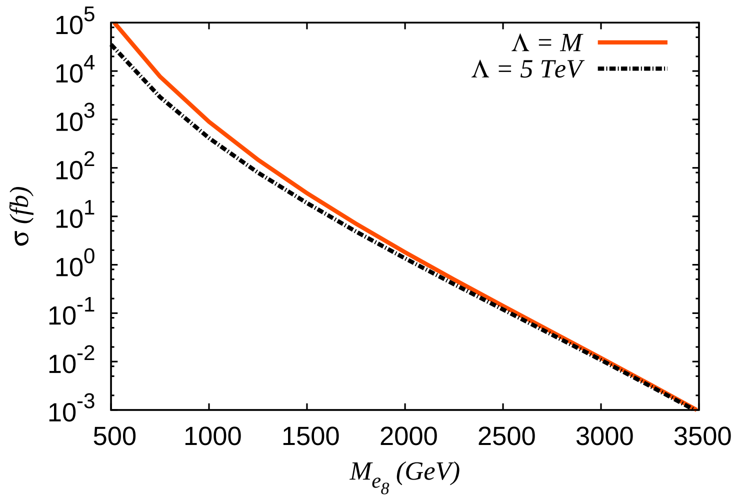

Figure 5.3: The c.s. for $pp \to e_8 e_8$ as functions of M_{e_8} for $\Lambda = M_{e_8}$ and $\Lambda = 5$ TeV at the 14 TeV LHC.

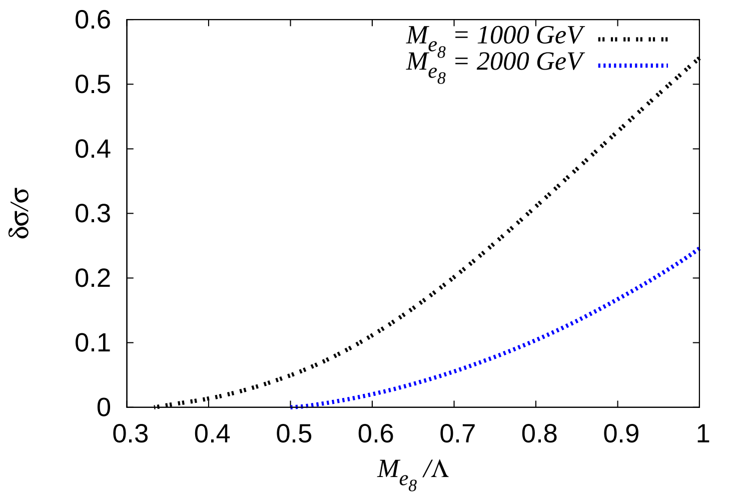

Figure 5.4: Dependence of $\delta\sigma/\sigma$ (defined in Eq. (5.6)) on M_{e_8}/Λ for $M_{e_8} = 1$ TeV and 2 TeV at the 14 TeV LHC.

$\Lambda = 5$ TeV, at the 14 TeV LHC. In Fig. 5.4 we have plotted $\delta\sigma$ as functions of Λ to show the dependence of the pair production c.s. on Λ for $M_{e_8} = 1$ and 2 TeV, where $\delta\sigma$ is a measure of the contribution of the electron exchange diagram and is defined as,

$$\delta\sigma(\Lambda) = \sigma(\Lambda) - \sigma(\Lambda \to \infty) \ . \tag{5.6}$$

As Λ increases the contribution coming from the electron exchange diagrams decreases and for $\Lambda \gg M_{e_8}$ becomes negligible. So the pair production is model independent only for very large Λ. After being pair produced at the LHC, each e_8 decays into an electron (or a positron) and a gluon at the parton level, *i.e.*, $gg/qq \to e_8 e_8 \to eejj$. For large M_{e_8}, these two jets and the lepton pair will have high-p_T. This feature can be used to isolate the e_8 pair production events from the SM backgrounds at the LHC.

5.3.2 Two-body Single Production ($\mathbf{gg, qq \to e_8 e}$)

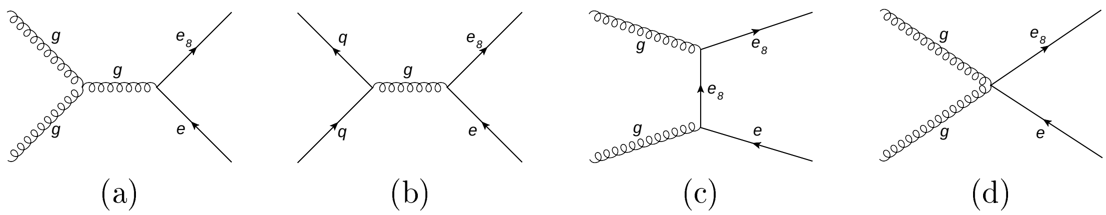

Figure 5.5: Parton level Feynman diagrams for $pp \to e_8 e$ process at the LHC.

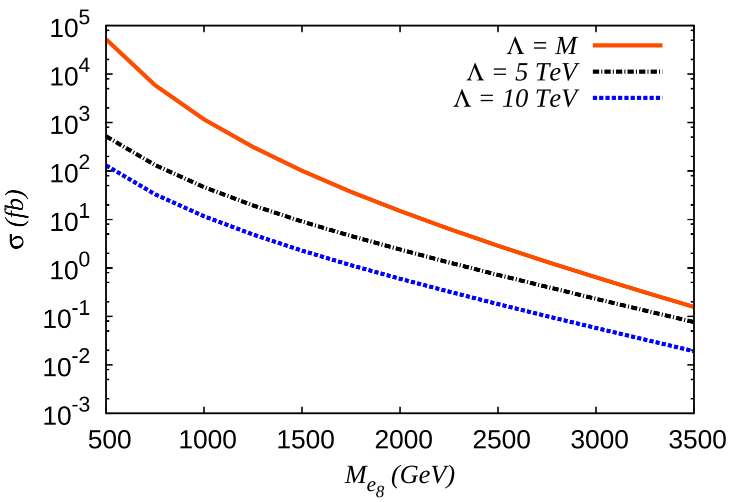

Figure 5.6: The c.s. for $pp \to e_8 e$ as functions of M_{e_8} for $\Lambda = M_{e_8}$, 5 TeV and 10 TeV at the 14 TeV LHC.

The two-body single production channel where an e_8 is produced in association with an electron can have either gg or qq initial states as shown in Fig. 5.5. This channel is model dependent as each Feynman diagram for the $pp \to e_8 e$ process contains a Λ dependent vertex. In Fig. 5.6 we show the $pp \to e_8 e$ c.s. as functions of M_{e_8} with $\Lambda = M_{e_8}$ and 5 TeV and 10 TeV at the 14 TeV LHC. As the e_8 decays, this process gives rise to a eej final state at the parton level. The e and the j produced from the decay of the e_8, have high-p_T. The other e also possesses very high-p_T as it balances against the massive e_8.

5.3.3 Three-body Single Production ($\mathbf{gg, gq, qq \to e_8 ej}$)

Apart from the pair and the two-body single productions, we also consider single production of an e_8 in association with an electron and a jet. The $pp \to e_8 ej$ process includes three different types of diagrams as follows:

1. The diagrams where the ej pair is coming from another e_8. Though there are three particles in the final state, this type of diagram effectively corresponds to two body pair production process.

2. The two body single production ($pp \to e_8 e$) process with a jet radiated from initial state (ISR) or final state (FSR) or intermediate virtual particles can lead to an $e_8 ej$ final state.

3. A new set of diagrams that are different from the two types of diagrams mentioned above. These new channels can proceed through gg, qq and gq initial states as shown in Fig. 5.7.

This new set of diagrams has not been considered so far in the literature. It is difficult to compute the total contribution of these diagrams in a straight forward manner with a leading order parton level matrix element calculation because of the presence of soft radiation jet emission diagrams. In order to get an estimation of the contribution of these

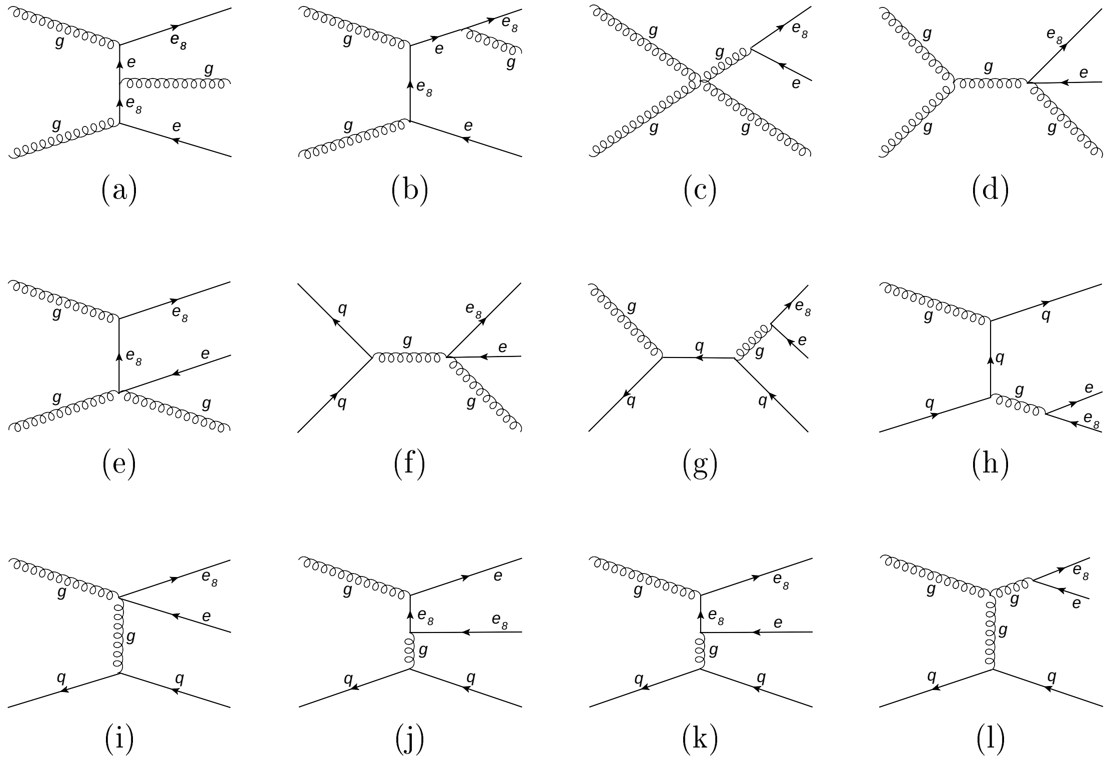

Figure 5.7: Parton level Feynman diagrams for $pp \to e_8 e j$ process of third type at the LHC.

new diagrams without getting into the complicacy of evaluating the soft jet emission diagrams, here, in this section, we present the c.s. only for the gq initiated processes, *i.e.* $gq \to e_8 e j$ since the first and the second types of diagrams of $pp \to e_8 e j$ process can not be initiated by gq state. In Fig. 5.9 we show the c.s. of the $gq \to e_8 e j$ process along with the $pp \to e_8 e_8$ and the $pp \to e_8 e$ processes. We find that the c.s. even for the gq initiated subset can be comparable to the $pp \to e_8 e_8 / e_8 e$ processes for large M_{e_8} despite the facts that these new diagrams have three-body final states and are suppressed by one extra power of the coupling (either g_s or g_s/Λ) compared to the two-body single and pair production processes. However, since there is one less e_8 compared to the pair production process, depending on the coupling the three-body phase space of the single production can be comparable or even larger to the two-body phase space of the pair production for large M_{e_8}. After the e_8 decay, the three-body single production process is characterized by an $eejj$ final state like the pair production. However, unlike the pair production, here one of the jet can have a low transverse momentum most of the time.

5.3.4 Indirect Production (gg → ee)

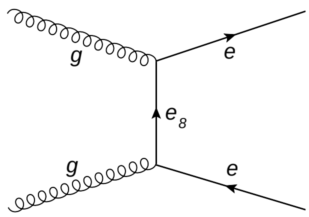

Figure 5.8: Parton level Feynman diagram for indirect production of e_8's at the LHC.

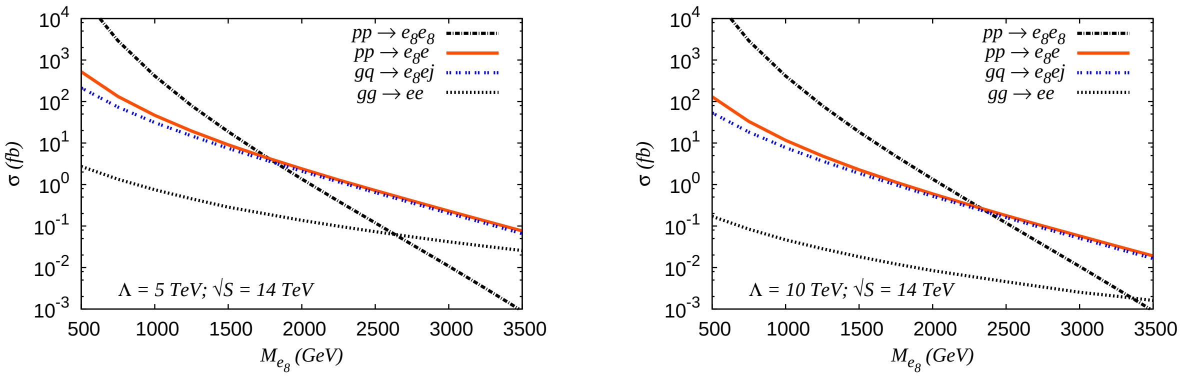

(a)

(b)

Figure 5.9: c.s. for $pp \to e_8 e_8$, $pp \to e_8 e$, $gq \to e_8 e j$ and $gg \xrightarrow{e_8} ee$ processes for $\Lambda = 5$ TeV and 10 TeV at the 14 TeV LHC. The $\sigma(gq \to e_8 e j)$ is computed with the following kinematical cuts: $p_T(j) > 25$ GeV and $|y(j)| < 2.5$.

So far we have considered only resonant production of e_8's. However, a t-channel exchange of the e_8 can convert a gluon pair to an electron-positron pair at the LHC (Fig. 5.8). Similar indirect productions in the context of the future linear colliders such as the ILC and CLiC have been analyzed in [77]. Indirect production is less significant because the amplitude is proportional to $1/\Lambda^2$. Moreover, at the LHC this is also color suppressed because of the color singlet nature of the final states. In Fig. 5.9 we also show the c.s. of the indirect production process at the LHC.

5.4 LHC Discovery Potential

From Fig. 5.9 we see that for small M_{e_8}, the pair production c.s. is larger than the other channels. As M_{e_8} increases, it decreases rapidly due to phase-space suppression and the single production channels (both the two-body and the three-body) take over the pair production (the crossover point depends on Λ). Hence, if Λ is not too high, the single production channels will have better reach than the pair production channel and so, to estimate the LHC discovery reach, we consider both the pair and the single production channels. However, while estimating for the single production channels we have to remember that because of the radiation jets, it will be difficult to separate the two-body and the three-body single productions at the LHC. So, in this paper, we consider a selection criterion that combines events from all the production processes at the LHC.

5.4.1 Combined Signal

To design the selection criterion mentioned above we first note some of the characteristics of the final states of the resonant production processes [2],

1. Process $pp \to e_8 e_8 \to (eg)(eg)$ has two high-p_T electrons and two high-p_T jets in the final state.

2. Process $pp \to e_8 e \to (eg)e$ has two high-p_T electrons and one high-p_T jet in the final state.

3. Process $pp \to e_8 ej \to (eg)ej$ has two high-p_T electrons and at least one high-p_T jet in the final state.

All these processes have one common feature that they have two high-p_T electrons and a high-p_T jet in the final state. Hence, if we demand that the signal events should have two high-p_T electrons and at least one high-p_T jet, we can capture events from all

[2]We focus on the resonant productions because as we saw the indirect production is less significant at the LHC.

the above mentioned production processes. To estimate the number of signal events that pass the above selection criterion we combine the events from all the production channels mentioned in the previous section. However, as already pointed out, it is difficult to estimate the number of signal events with only a matrix element (ME) level Monte Carlo computation due to the presence of soft radiation jets. Hence, we use the MadGraph ME generator to compute the hard part of the amplitude and Pythia6 (via the MadGraph5-Pythia6 interface) for parton showering. We also match the matrix element partons with the parton showers to estimate the inclusive signal without double counting (see the Appendix B for more details on the matched signal).

5.4.2 SM Backgrounds

With the selection criterion mentioned in the previous section to capture all the contributions from different production channels, the SM backgrounds are characterized by the presence of two opposite-sign electrons and at least one jet in the final state. At the LHC, the main source of e^+e^- pairs (with high-p_T) is the Z decay [3]. Hence, we compute the inclusive Z production as the main background. Here, too, we compute this by matching of matrix element partons of $Z+n$ jets ($n=0,1,2,3$) processes[4] with the parton showers using the shower-k_T scheme [113]. For the background, we also consider some potentially significant processes to produce e^+e^- pairs,

$$
\begin{aligned}
pp &\rightarrow tt \rightarrow (bW)(bW) \rightarrow (be\nu_e)(be\nu_e) \ , \\
pp &\rightarrow tW \rightarrow bWW \rightarrow (be\nu_e)(e\nu_e) \ , \\
pp &\rightarrow WW \rightarrow (e\nu_e)(e\nu_e) \ .
\end{aligned}
$$

Note that all these processes have missing energy because of the ν_e's in the final state. In Table 5.1 we show the relative contributions of these backgrounds generated with some

[3]Here we do not include e^+e^- pairs that come from γ^*. However, as we shall demand very high-p_T for both the electrons, this background becomes negligible and would not affect our results too much.

[4]Here $pp \rightarrow Zjj$ includes the processes where the jets are coming from a W or a Z.

basic kinematical cuts (to be described shortly) on the final states . As mentioned, we see in Table 5.1 that the inclusive Z contribution overwhelms the other background processes.

Process	Cross section (fb)
$Z + nj$	$2.11E4$
tt	$1.95E3$
tW	132.15
WW	7.51
Total	$2.32E4$

Table 5.1: The main SM backgrounds for the combined production of e_8's obtained after applying the Basic cuts (see text for definition) at the 14 TeV LHC.

5.4.3 Kinematical Cuts

In Fig. 5.10(a) we display the p_T distributions of e's from the combined signal and the inclusive Z production, respectively. For the signal, we have chosen $M_{e_8} = 2$ TeV and $\Lambda = 5$ TeV. As expected, the distribution for the e coming from the background has a peak about $M_Z/2$ but there is no such peak for the signal. We can also see the difference between the p_T distributions of the leading p_T jets for the signal and the background in Fig. 5.10(b). We also display the distributions of $M(e^+, e^-)$ in Fig. 5.10(c) and $M(e^-, j_1)$ in Fig. 5.10(d) (where j_1 denotes the leading p_T jet) which show very different shapes for the signal and the background. Motivated by these distributions we construct some kinematical cuts to separate the signal from the background.

1. **Basic cuts**

   For $x, y = e^+, e^-, j_1, j_2$ (j_1 and j_2 denote the first two of the p_T-ordered jets respectively),

   (a) $p_T(x) > 25$ GeV

   (b) Rapidity, $|\eta(x)| < 2.5$

   (c) Radial distance, $\Delta R(x, y)_{x \neq y} \geq 0.4$

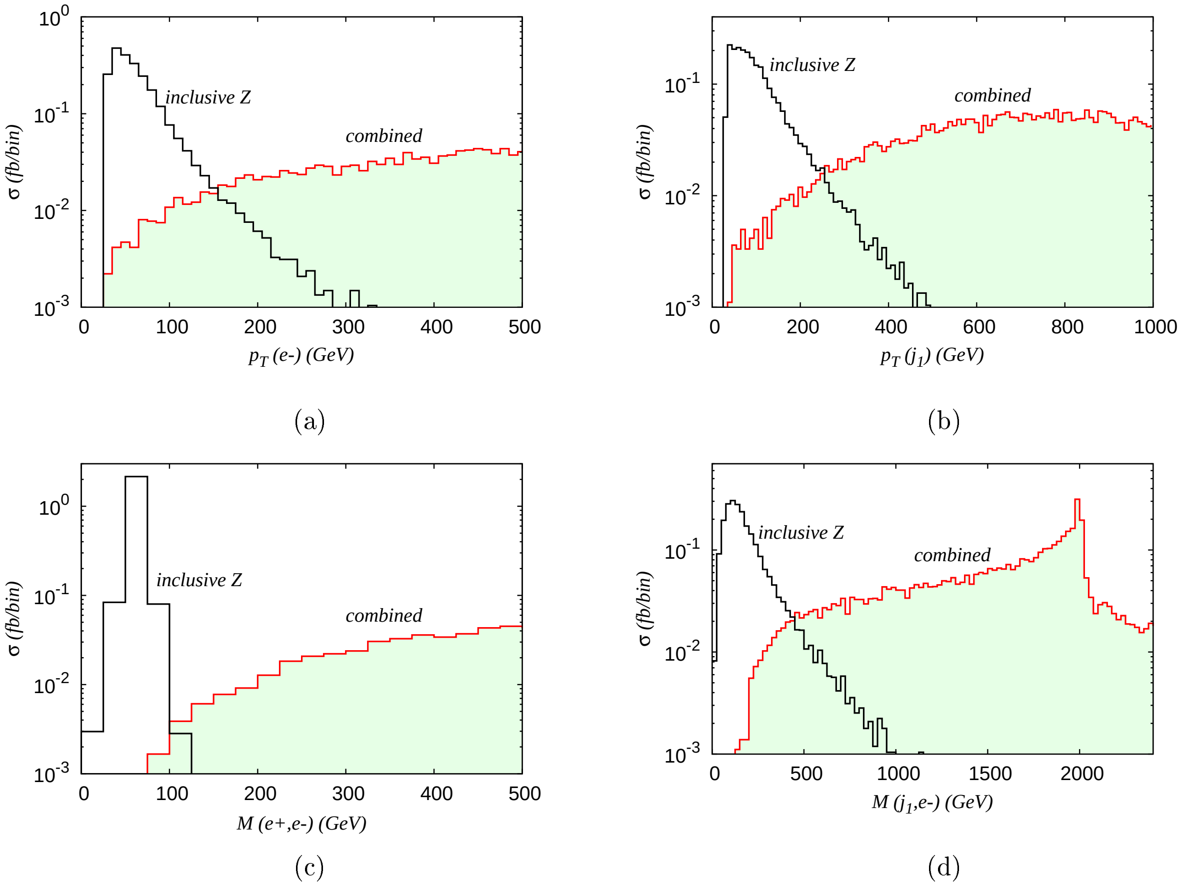

Figure 5.10: Comparison between various distributions for the combined signal with $M_{e_8} = 2$ TeV ($\Lambda = 5$ TeV) and the inclusive Z background for the 14 TeV LHC. The inclusive Z background is scaled by a factor of 10^4.

2. **Discovery cuts**

   (a) All the *Basic* cuts

   (b) $p_T(e^+/e^-) > 150$ GeV; $p_T(j_1) > 100$ GeV

   (c) $M(e^+, e^-) > 150$ GeV

   (d) For at least one combination of (e, j_i): $|M(e, j_i) - M_{e_8}| \leq 0.2M_{e_8}$ where $e = e^+$ or e^- and $j_i = j_1$ or j_2.

The invariant mass cut on $M(e^+, e^-)$ can remove the Z inclusive background almost completely. We also demand that either of the electrons reconstruct to an e_8 when combined with any one of j_1 or j_2. We find that the "Discovery cuts" can reduce the SM background drastically. Especially for higher M_{e_8} the background becomes much smaller compared to the signal, making it essentially background free. For example, taking $M_{e_8} = 0.5$ TeV (1 TeV) we estimate the total SM background with the "Discovery cuts" at the 14 TeV LHC to be about 4 fb (0.3 fb). Although these numbers are only rough estimates for the actual SM backgrounds (as, *e.g.*, we do not consider the effect of any loop induced diagrams) they indicate the SM backgrounds become very small compared to the signal (see Table 5.2) after the "Discovery cuts". In Table 5.2 we show the signal with the above two cuts applied.

M_{e_8}	$\Lambda = 5$ TeV		$\Lambda = 10$ TeV	
(GeV)	Basic (fb)	Disco. (fb)	Basic (fb)	Disco. (fb)
500	2.73E4	1.31E4	2.70E4	1.27E4
750	2.63E3	1.93E3	2.59E3	1.91E3
1000	442.95	367.20	415.35	347.16
1250	105.21	90.25	91.99	80.45
1500	31.73	27.25	24.54	21.86
1750	11.53	9.76	7.52	6.71
2000	4.77	3.92	2.59	2.28
2250	2.26	1.80	0.99	0.85
2500	1.18	0.91	0.42	0.36
2750	0.65	0.49	0.20	0.16
3000	0.37	0.27	0.11	0.08
3250	0.22	0.16	0.06	0.04
3500	0.13	0.09	0.03	0.02

Table 5.2: The combined signal after basic and "Discovery cuts" (see text for the definitions of the cuts) for $\Lambda = 5$ TeV and 10 TeV for different M_{e_8} at the 14 TeV LHC.

5.4.4 LHC Reach with Combined Signal

We define the luminosity requirement for the discovery of e_8 as $L_D = \mathrm{Max}(L_5, L_{10})$, where L_5 denotes the luminosity required to attain 5σ statistical significance for $S/\sqrt{B}$ and L_{10} is the luminosity required to observe 10 signal events. We show L_D as functions of M_{e_8} for the "Discovery cuts" in Fig. 5.11 for $\Lambda = 5$ TeV and 10 TeV at the 14 TeV LHC. In Fig. 5.11 we also plot the L_D using only the pair production process. To estimate the pair production from the combined signal we apply a set of kinematical cuts almost identical to the "Discovery cuts" except that now we demand that the two electrons and the two leading p_T jets reconstruct to two e_8's instead of one:

1. **Pair production extraction cuts**

    (a) All the *Basic* cuts

    (b) $p_T(e^+/e^-) > 150$ GeV; $p_T(j_1) > 100$ GeV

    (c) $M(e^+, e^-) > 150$ GeV

    (d) $|M(e^+, j_k) - M_{e_8}| \leq 0.2 M_{e_8}$ and $|M(e^-, j_l) - M_{e_8}| \leq 0.2 M_{e_8}$ with $k \neq l = \{1, 2\}$.

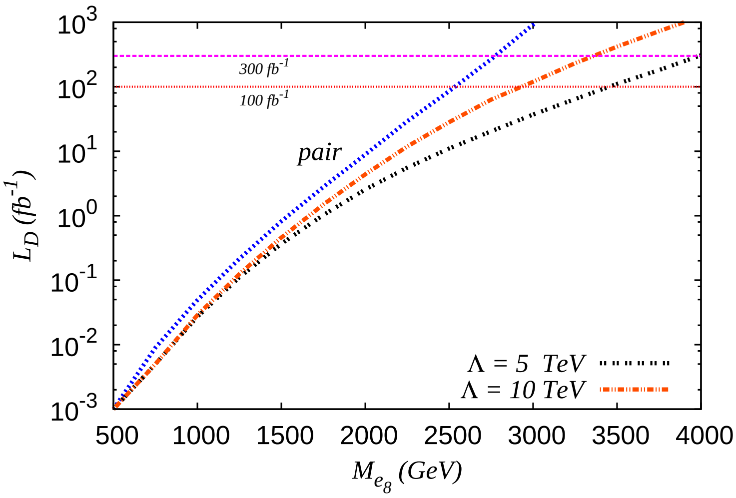

Figure 5.11: The required luminosity for discovery (L_D) as a function of M_{e_8} with $\Lambda = 5$ TeV and 10 TeV at the 14 TeV LHC for combined production with "Discovery cuts" (see text for the definitions of the cuts). The L_D for pair production is computed after demanding two e_8's are reconstructed instead of one.

In Fig. 5.11, L_D goes as L_{10} for both pair and combined productions, as in these cases the backgrounds become quite small compared to the signals. With the "Discovery cuts" the reach goes up to 3.4 TeV and 2.9 TeV (4 TeV and 3.3 TeV) with 100 fb^{-1} (300 fb^{-1}) integrated luminosity for $\Lambda = 5$ TeV and 10 TeV respectively at the 14 TeV LHC. This also shows that for $\Lambda = 5$ TeV (10 TeV) with combined signal at 14 TeV LHC with 300 fb^{-1} integrated luminosity the reach goes up from the pair production by almost 1.2 TeV (0.5 TeV). However, we should keep in mind that this increase depends on Λ. As the single production c.s. goes like $1/\Lambda^2$, if Λ is smaller than 5 TeV then the reach of the combined production will increase even more but for higher Λ (like $\Lambda = 10$ TeV as shown in Fig. 5.11) its L_D plot will approach more towards the pair production plot.

Chapter 6

Summary and conclusions

This thesis deals with the LHC phenomenology of vectorlike quarks that arise in various warped extra dimensional theories and the color octet electrons which appear in some quark-lepton compositeness models. Chapter 1 is an introductory chapter where we briefly discuss some theoretical shortcomings of the SM and motivate the need for BSM physics that explains some of the unanswered questions of the SM. Many BSM extensions predict the existence of new heavy fermions with masses near the TeV scale. In this thesis we study the LHC phenomenology of two types of such new heavy fermions, namely the vectorlike quarks (VLQ) that arise for instance in various warped extra-dimensional theories, and the color octet electrons (e_8) that appear in some quark-lepton compositeness models. We briefly survey some theoretical as well as recent experimental references that are relevant to our study.

In Chapter 2 we review the construction of the RS model, including the derivation of the warped metric as a solution to the Einstein's equations [83]. We show how this model solves the gauge hierarchy problem of the SM and present a short discussion on models with bulk gauge and fermion fields coupled with a Higgs peaked at the IR brane. We give the details of some warped models both without [91] and with [92] custodial protection of the $Z\bar{b}_L b_L$ coupling [97] that have been proposed earlier in the literature. Our work has been presented in Refs. [97, 99] where we discuss the gauge sector and different quark representations of these models. For each of these models we carefully work out various Lagrangian terms in the mass basis relevant to the phenomenology we discuss in the thesis. In Chapter 3 we present the parameter choices, which we use for our numerical results, for the different warped-space models discussed in Chapter 2. We consider three different cases of warped models differing in the fermion representations under $SU(2)_L \otimes SU(2)_R \otimes U(1)_X$ gauge group. We label them by the representation t_R appears in, namely, Doublet Top (DT), Singlet Top (ST) and Triplet Top (TT) models. More than one b' (charge -1/3), t' (charge 2/3) and χ (charge 5/3), can be present depending on the model, and they can mix among themselves and the SM quarks. We plot mass eigenvalues and various important couplings for the LHC phenomenology as functions of bulk mass parameter c_{q_L} for different warped models. We identify all kinematically allowed two-body decay modes of b', t' and χ, and compute total decay widths and branching ratios of them in the warped models we discussed earlier.

In Chapter 4 we study the LHC signatures of vectorlike b', t' and χ quarks. We implement different warped models in matrix element and event generators MadGraph 5 [112] and CalcHEP [102] to compute signal and main irreducible SM backgrounds. We explore the pair production channel for discovery of the new VLQs. However, in addition to pair production, we also look into some of their important single production channels since single production processes can give useful information about the electroweak nature of the underlying models. There are some distinct signatures of vectorlike nature of the b', t' and χ. For example, a unique signature of a vectorlike b' is that it decays to bZ and bh modes in addition to the tW mode which is also present for a chiral (4th generation) b'. We study the LHC signatures of the b' particularly focusing on bZ and bh channels to expose its vectorlike nature [99]. We explore the $pp \to b'b'$ pair production and, $b'Z$, $b'h$ and $b'bZ$ single production processes at the 14 TeV LHC followed by their decays to different final states [99]. Using the $b'b' \to bZbZ \to bjjbll$ channel we find that the LHC reach to be about $M_{b'} \approx 1250$ GeV with about 1300 fb^{-1} integrated luminosity. For $pp \to b'Z$ channel we also present model independent contour plots for c.s. and luminosity varying $\kappa_{b'bZ}$ and $M_{b'}$. We consider $pp \to b'bZ \to bZbZ$ channel which includes the double resonant (DR) pair production ($b'b'$) and also the single resonant (SR) production of b' including the contribution from $b'b'^*$ where one of the b' is offshell. We expect that SR contribution scales as $\kappa^2_{b'bZ}$ while DR contribution depends on the g_S. We show that $\kappa_{b'bZ}$ can be extracted by using an invariant mass cut [97]. Isolating SR contribution from $pp \to b'bZ$ events by using the invariant mass cut, we explicitly demonstrate that SR c.s. indeed scales as $\kappa^2_{b'bZ}$.

For the t' phenomenology we explore the $pp \to t'th \to thth$ channel which includes the (DR+SR) production of t' and compute the signal c.s. for different t' masses in the warped models and main irreducible SM backgrounds at the 8 and 14 TeV LHC. We find that the 14 TeV LHC can probe the t' mass of the order of 1 TeV with 100 fb^{-1} of integrated luminosity in the warped space models.

For the χ we consider $pp \to \chi tW \to tWtW$ channel which includes the (DR+SR) production of χ. We find that using this channel the 14 TeV LHC can probe $M_\chi \approx 1.5$ TeV (1.75 TeV) with 100 fb^{-1} (300 fb^{-1}) of integrated luminosity. Similar to the b', we show that the SR production of the t' and χ can be used to extract the new physics couplings related to those processes.

For b', t' and χ we present model independent discovery luminosity plots as functions of couplings for different masses using SR production which has the potential of giving information on the underlying electroweak nature of these states. Although our study is motivated by warped space models, we present our results in a model independent fashion wherever possible.

Chapter 5 deals with color octet electrons arising in some composite models. These models assume that SM particles may not be fundamental and they are actually bound states of substructural constituents called preons [60]. These constituents are visible only beyond the compositeness scale Λ. Some composite models naturally predict the existence of color octet fermions with nonzero lepton numbers.

We discuss the LHC phenomenology of e_8 in an effective theory framework. To generate signal and background events, we have implemented the Lagrangian in FeynRules [110] to generate Universal FeynRules Output (UFO) [111] format model files suitable for MadGraph5 [112] to generate events. Although, here we consider only the e_8, our results are applicable for the color octet partner of muon, *i.e.*, μ_8 also. We briefly discuss various preonic models of quark-lepton compositeness in which e_8 are present. We display the interaction Lagrangian of a generic e_8 and decay width of e_8 for different choice of Λ. Our work has been presented in Ref. [114] where we explore various resonant productions (pair and various single production channels) of e_8's in the context of the LHC. We have identified a new set of single production diagrams whose contribution is comparable to other dominant production channels of the e_8. In a realistic computation, after parton showering and hadronization, it is very difficult to separate different production processes from each other. A common feature in all the resonant production channels of the e_8 is the presence of two high p_T electrons and at least one high p_T jet in the final state. Using this feature, in our work [114], we implement a search method where the signal is a combination of pair and single production events. This method has potential to increase the LHC reach significantly. To generate the combined events we use MLM shower-k_T matching algorithm [113] to match the matrix element partons with the parton showers. The main SM background comes from the inclusive Z production and we compute the $Z + n$ jets ($n = 0, 1, 2, 3$) background using the shower-k_T scheme.

Assuming 100% branching ratio for the decay, $e_8 \to eg$, we estimate the LHC discovery potential for the e_8's. We show that using only the pair production channel the 14 TeV LHC can probe e_8 with mass up to 2.5 TeV (2.8 TeV) with 100 fb^{-1} (300 fb^{-1}) of integrated luminosity. We demonstrate that this reach can be increased further by combining signal events from different production processes. However, this increment is Λ dependent as the single production c.s. scales as $1/\Lambda^2$. For $\Lambda = 5$ TeV (10 TeV) the increment is about 0.9 TeV (0.4 TeV) with 100 fb^{-1} of integrated luminosity at the 14 TeV LHC and with 300 fb^{-1} of integrated luminosity it is about 1.2 TeV (0.5 TeV). We point out that our analysis can also be used to probe Λ, the compositeness scale, for any fixed M_{e_8}. This is possible because of the scaling of the single production c.s. with Λ. We show that for $M_{e_8} = 2$ TeV the 14 TeV LHC with 100 fb^{-1} (300 fb^{-1}) of integrated luminosity can probe $\Lambda \sim 35$ TeV (55 TeV). We note that the data from the current leptoquark searches at the LHC can be used to search for e_8's also. We point out that the current data for first generation charged leptoquark in the pair production channel clearly rules out a e_8 of mass less than 900 GeV [67, 68].

Appendix A

Model Implementation

To obtain signal c.s., we have implemented various Lagrangian terms of warped model VLQs and Lagrangian for e_8 in FeynRules version 1.6.0 [110]. The user needs to provide FeynRules with the minimal information required to describe the new model. The FeynRules code then generates Universal FeynRules Output (UFO) [111] format model files suitable for Monte-Carlo generator MadGraph5 [112] that we have used to estimate the signal c.s. For SM background computations we have used model files which are already available with the MadGraph5 package.

A.1 DT model implementation in FeynRules

As an example, we show an implementation of the DT model in FeynRules. In the DT model we compute the numerical values of the terms appearing in the bottom mass matrix in Eq. (2.48). Using these values one can compute the mixing angles in Eq. (2.49) and hence all the couplings in the Lagrangian as shown in Eqs. (2.53)-(2.56). To implement the DT model we use existing SM FeynRules files where we add three bottom mass matrix elements M_b (`Mb`), $M_{b'}$ (`Mbp`) and $M_{bb'}$ (`Mbbp`) as external parameters (notations used in FeynRules are shown in braket). Next, we define internal parameters $\sin\theta_{L,R}$ (`SL,SR`) and $\cos\theta_{L,R}$ (`CL,CR`) as functions of M_b, $M_{b'}$ and $M_{bb'}$. We need to provide some information of the b' (bp) quark in FeynRules (we refer readers to FeynRules manual to know about the syntax) where we define a new fermion class as follows

```
F[5] == {
  ClassName       -> bp,
  SelfConjugate   -> False,
  Indices         -> Index[Colour],
  Mass            -> {Mbp, 1000},
  Width           -> {Wbp, 21.304},
  QuantumNumbers  -> {Q -> -1/3},
  PDG             -> 7,
  PropagatorLabel -> {"bp"},
  PropagatorType  -> Straight,
  PropagatorArrow -> Forward,
  FullName        -> {"bp-quark"}},
```

We assign a new Monte-Carlo PDG code "7" for b'. FeynRules program cannot compute the total width of a particle using the masses and couplings information unless the analytical formula for the total width is defined explicitly in the code. We have computed the total width using analytical formula and used that value in the block above. We define interaction terms of the DT model (Eqs. (2.53)-(2.56)) following FeynRules syntax as

- Kinetic term for b'

  ```
  LbpKIN := I bpbar.Ga[mu].del[bp, mu];
  ```

- QCD and QED interactions

  ```
  LbpQCD := gs bpbar.Ga[mu].T[a].bp G[mu,a];
  LbpQED := -(ee/3) bpbar.Ga[mu].bp A[mu];
  ```

- charged current interactions

```
LbpCC := (gw SL/Sqrt[2]) tbar.ProjM[mu].bp W[mu];
```

- Neutral current interactions

```
LbpNC1 := gz ((-1/2 CL^2 + 1/3 sw2) bbar.ProjM[mu].b Z[mu] +
           (1/3 sw2) bbar.ProjP[mu].b Z[mu] +
           (-1/2 SL^2 + 1/3 sw2) bpbar.ProjM[mu].bp Z[mu] +
           (1/3 sw2) bpbar.ProjP[mu].bp Z[mu];
LbpNC2 := gz (1/2 CL SL) bbar.ProjM[mu].bp Z[mu]
```

- Higgs interactions

```
LbpH := -((Mb CL CR - Mbbp CL SR) bbar.ProjP.b H +
        (Mb SL SR - Mbbp SL CR) bpbar.ProjP.bp H +
        (-Mb CL SR + Mbbp CL CR) bbar.ProjP.bp H +
        (-Mb SL CR - Mbbp SL SR) bpbar.ProjP.b H)/v;
```

- Full Lagrangian for b' in the DT model

```
Lbp := LbpKIN + LbpQCD + LbpQED + (LbpCC + HC[LbpCC]) +
      (LbpNC1 + LbpNC2 + HC[LbpNC2]) + (LbpH + HC[LbpH]);
```

In a similar way we have written FeynRules files for t', χ and e_8 Lagrangian terms to generate MadGraph5 model files. In the future we plan to make these model files public.

Appendix B

Preparation of Matched Signal

While generating the combined signal for e_8 and inclusive Z background, we sometime face double counting of an event. This can happen when a process after parton showering is actually the same process at the partonic level. Double counting can be avoided by considering a matching scale. This scale Q_{cut} determines whether a jet has come from parton showering (if the jet-p_T is below Q_{cut}) or originated at the partonic level (if the jet-p_T is above Q_{cut}). We match the matrix element partons with the parton showers using the shower-k_T scheme [113] in MadGraph5 with the matching scale $Q_{cut} \sim 50$ GeV. We choose appropriate matching scale Q_{cut} for signal and background by looking at the smoothness of their differential jet rate distributions as shown in Fig. B.1 and B.2 respectively. The smoothness of the transition region indicates how good the choice of Q_{cut} is. After varying Q_{cut} from 25 GeV to 100 GeV, we find Q_{cut} about 50 GeV is a good choice of matching scale for both the signal and background. We generate the combined signal including the different production processes as discussed in section 5.4 as follows

$$\begin{aligned}
pp &\xrightarrow{e_8} ee + 0\text{-j (includes } P_{ind}) \\
pp &\xrightarrow{e_8} ee + 1\text{-j (includes } P_{ind}+\text{ 1-j, } P_{2Bs}\text{)} \\
pp &\xrightarrow{e_8} ee + 2\text{-j (includes } P_{ind}+\text{ 2-j, } P_{2Bs}+\text{ 1-j, } P_{pair}\text{ , } P^3_{3Bs}\text{)} \\
pp &\xrightarrow{e_8} ee + 3\text{-j (includes } P_{ind}+\text{ 3-j, } P_{2Bs}+\text{ 2-j, } P_{pair}+\text{ 1-j, } P^3_{3Bs}+\text{ 1-j)}
\end{aligned} \tag{B.1}$$

where P_{pair}, P_{2Bs}, P^3_{3Bs} and P_{ind} are the pair, two body single, three body single of third type (as defined in 5.3.3) and indirect production channels respectively. An elaborate discussion on matching is beyond the scope of this thesis, and we refer the reader to Ref. [113] and the references therein for more details on the matching scheme and the procedure.

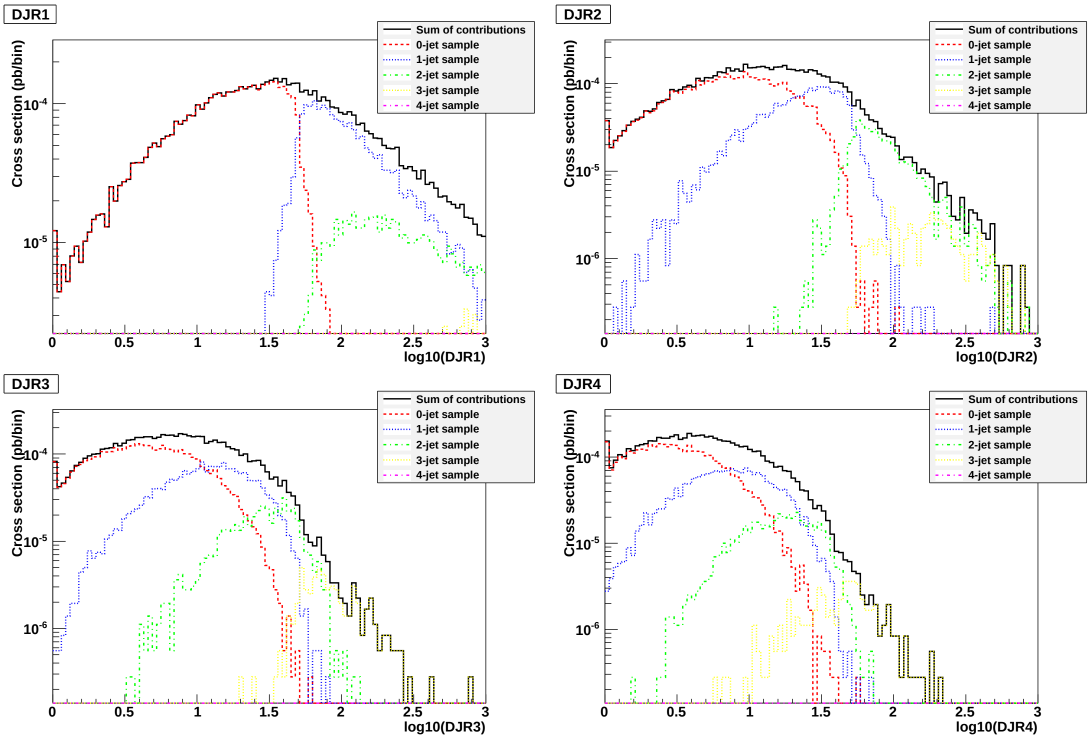

Figure B.1: Differential jet rate distributions for the combined signal with $M_{e_8} = 2$ TeV and $\Lambda = 5$ TeV at the 14 TeV LHC. Here we choose $Q_{cut} = 50$ GeV.

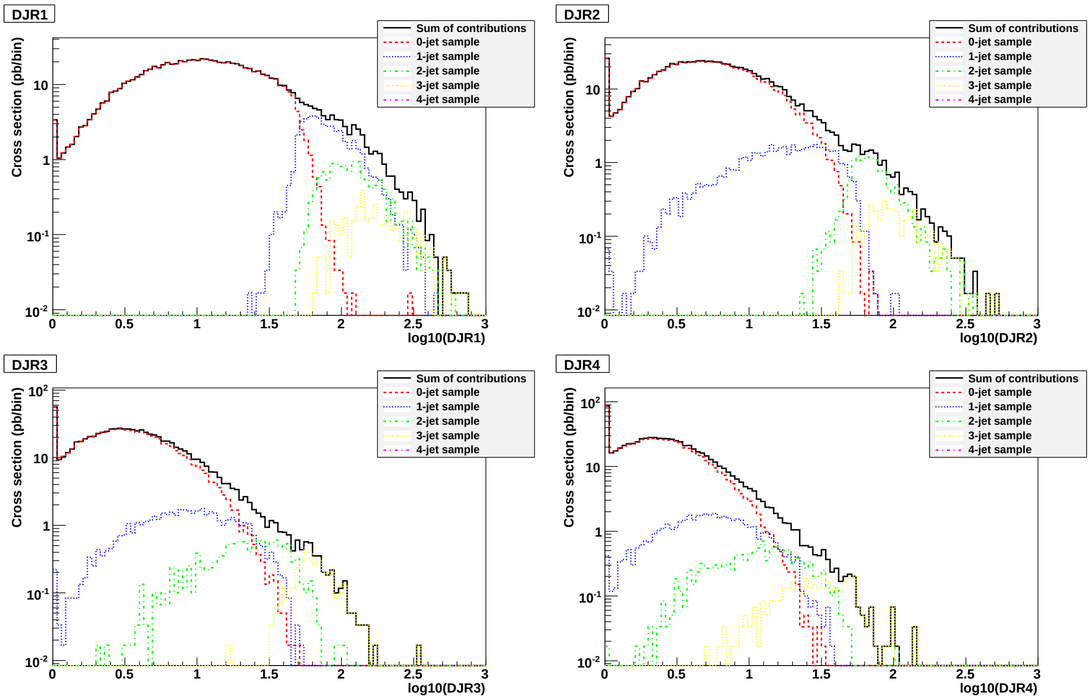

Figure B.2: Differential jet rate distributions for the inclusive Z (includes $Z + 0, 1, 2, 3$ jets) background at the 14 TeV LHC. Here we choose $Q_{cut} = 50$ GeV.

Bibliography

[1] G. Aad *et al.* [ATLAS Collaboration], Phys. Lett. B **716**, 1 (2012) [arXiv:1207.7214 [hep-ex]].

[2] S. Chatrchyan *et al.* [CMS Collaboration], Phys. Lett. B **716**, 30 (2012) [arXiv:1207.7235 [hep-ex]].

[3] A. Djouadi and A. Lenz, Phys. Lett. B **715**, 310 (2012) [arXiv:1204.1252 [hep-ph]].

[4] [ATLAS Collaboration], ATLAS-CONF-2013-034.

[5] [CMS Collaboration], CMS-PAS-HIG-13-005.

[6] O. Eberhardt, G. Herbert, H. Lacker, A. Lenz, A. Menzel, U. Nierste and M. Wiebusch, Phys. Rev. Lett. **109**, 241802 (2012) [arXiv:1209.1101 [hep-ph]].

[7] R. Contino, L. Da Rold and A. Pomarol, Phys. Rev. D **75**, 055014 (2007) [hep-ph/0612048].

[8] C. Anastasiou, E. Furlan and J. Santiago, Phys. Rev. D **79**, 075003 (2009) [arXiv:0901.2117 [hep-ph]].

[9] N. Vignaroli, JHEP **1207**, 158 (2012) [arXiv:1204.0468 [hep-ph]].

[10] A. De Simone, O. Matsedonskyi, R. Rattazzi and A. Wulzer, JHEP **1304**, 004 (2013) [arXiv:1211.5663 [hep-ph]].

[11] T. Han, H. E. Logan, B. McElrath and L. -T. Wang, Phys. Rev. D **67**, 095004 (2003) [hep-ph/0301040].

[12] M. S. Carena, J. Hubisz, M. Perelstein and P. Verdier, Phys. Rev. D **75**, 091701 (2007) [hep-ph/0610156].

[13] S. Matsumoto, T. Moroi and K. Tobe, Phys. Rev. D **78**, 055018 (2008) [arXiv:0806.3837 [hep-ph]].

[14] J. Berger, J. Hubisz and M. Perelstein, JHEP **1207**, 016 (2012) [arXiv:1205.0013 [hep-ph]].

[15] J. Kang, P. Langacker and B. D. Nelson, Phys. Rev. D **77**, 035003 (2008) [arXiv:0708.2701 [hep-ph]].

[16] P. W. Graham, A. Ismail, S. Rajendran and P. Saraswat, Phys. Rev. D **81**, 055016 (2010) [arXiv:0910.3020 [hep-ph]].

[17] S. P. Martin, Phys. Rev. D **82**, 055019 (2010) [arXiv:1006.4186 [hep-ph]].

[18] F. del Aguila, L. Ametller, G. L. Kane and J. Vidal, Nucl. Phys. B **334**, 1 (1990).

[19] F. del Aguila, G. L. Kane and M. Quiros, Phys. Rev. Lett. **63**, 942 (1989).

[20] A. Djouadi and G. Moreau, Phys. Lett. B **660**, 67 (2008) [arXiv:0707.3800 [hep-ph]].

[21] A. Azatov, O. Bondu, A. Falkowski, M. Felcini, S. Gascon-Shotkin, D. K. Ghosh, G. Moreau and S. Sekmen, Phys. Rev. D **85**, 115022 (2012) [arXiv:1204.0455 [hep-ph]].

[22] C. Bouchart and G. Moreau, Phys. Rev. D **80**, 095022 (2009) [arXiv:0909.4812 [hep-ph]].

[23] G. Moreau, Phys. Rev. D **87**, 015027 (2013) [arXiv:1210.3977 [hep-ph]].

[24] N. Bonne and G. Moreau, Phys. Lett. B **717**, 409 (2012) [arXiv:1206.3360 [hep-ph]].

[25] A. Djouadi, G. Moreau and F. Richard, Phys. Lett. B **701**, 458 (2011) [arXiv:1105.3158 [hep-ph]].

[26] A. Djouadi, G. Moreau, F. Richard and R. K. Singh, Phys. Rev. D **82**, 071702 (2010) [arXiv:0906.0604 [hep-ph]].

[27] A. Djouadi, G. Moreau and F. Richard, Nucl. Phys. B **773**, 43 (2007) [hep-ph/0610173].

[28] C. Bouchart and G. Moreau, Nucl. Phys. B **810**, 66 (2009) [arXiv:0807.4461 [hep-ph]].

[29] F. del Aguila, J. A. Aguilar-Saavedra and R. Miquel, Phys. Rev. Lett. **82**, 1628 (1999) [hep-ph/9808400].

[30] F. del Aguila, M. Perez-Victoria and J. Santiago, JHEP **0009**, 011 (2000) [hep-ph/0007316].

[31] J. A. Aguilar-Saavedra, Phys. Rev. D **67**, 035003 (2003) [Erratum-ibid. D **69**, 099901 (2004)] [hep-ph/0210112].

[32] G. Cacciapaglia, A. Deandrea, D. Harada and Y. Okada, JHEP **1011**, 159 (2010) [arXiv:1007.2933 [hep-ph]].

[33] G. Cacciapaglia, A. Deandrea, L. Panizzi, N. Gaur, D. Harada and Y. Okada, JHEP **1203**, 070 (2012) [arXiv:1108.6329 [hep-ph]].

[34] Y. Okada and L. Panizzi, Adv. High Energy Phys. **2013**, 364936 (2013) [arXiv:1207.5607 [hep-ph]].

[35] J. A. Aguilar-Saavedra, R. Benbrik, S. Heinemeyer and M. Perez-Victoria, arXiv:1306.0572 [hep-ph].

[36] R. Contino and G. Servant, JHEP **0806**, 026 (2008) [arXiv:0801.1679 [hep-ph]].

[37] J. Mrazek and A. Wulzer, Phys. Rev. D **81**, 075006 (2010) [arXiv:0909.3977 [hep-ph]].

[38] C. Dennis, M. Karagoz, G. Servant and J. Tseng, hep-ph/0701158.

[39] G. Cacciapaglia, A. Deandrea, L. Panizzi, S. Perries and V. Sordini, JHEP **1303**, 004 (2013) [arXiv:1211.4034 [hep-ph]].

[40] J. A. Aguilar-Saavedra, Phys. Lett. B **625**, 234 (2005) [Erratum-ibid. B **633**, 792 (2006)] [hep-ph/0506187].

[41] J. A. Aguilar-Saavedra, JHEP **0612**, 033 (2006) [hep-ph/0603200].

[42] A. Atre, M. Chala and J. Santiago, JHEP **1305**, 099 (2013) [arXiv:1302.0270 [hep-ph]].

[43] K. Harigaya, S. Matsumoto, M. M. Nojiri and K. Tobioka, Phys. Rev. D **86**, 015005 (2012) [arXiv:1204.2317 [hep-ph]].

[44] J. A. Aguilar-Saavedra, JHEP **0911**, 030 (2009) [arXiv:0907.3155 [hep-ph]].

[45] M. Carena, A. D. Medina, B. Panes, N. R. Shah and C. E. M. Wagner, Phys. Rev. D **77**, 076003 (2008) [arXiv:0712.0095 [hep-ph]].

[46] R. Barcelo, A. Carmona, M. Chala, M. Masip and J. Santiago, Nucl. Phys. B **857**, 172 (2012) [arXiv:1110.5914 [hep-ph]].

[47] C. Bini, R. Contino and N. Vignaroli, JHEP **1201**, 157 (2012) [arXiv:1110.6058 [hep-ph]].

[48] A. Atre, M. Carena, T. Han and J. Santiago, Phys. Rev. D **79**, 054018 (2009) [arXiv:0806.3966 [hep-ph]].

[49] T. Han, I. Lewis and Z. Liu, JHEP **1012**, 085 (2010) [arXiv:1010.4309 [hep-ph]].

[50] A. Atre, G. Azuelos, M. Carena, T. Han, E. Ozcan, J. Santiago and G. Unel, JHEP **1108**, 080 (2011) [arXiv:1102.1987 [hep-ph]].

[51] M. Buchkremer, G. Cacciapaglia, A. Deandrea and L. Panizzi, arXiv:1305.4172 [hep-ph].

[52] G. Brooijmans *et al.* [New Physics Working Group Collaboration], arXiv:1005.1229 [hep-ph].

[53] D. K. Ghosh, A. Nyffeler, V. Ravindran, N. Agarwal, P. Agarwal, P. Bandyopadhyay, R. Basu and B. Bhattacherjee *et al.*, Pramana **76**, 707 (2011).

[54] A. Alves, E. R. Barreto, D. A. Camargo and A. G. Dias, JHEP **1307** (2013) 129 [arXiv:1306.1275 [hep-ph]].

[55] [ATLAS Collaboration], ATLAS-CONF-2013-056.

[56] [ATLAS Collaboration], ATLAS-CONF-2013-060.

[57] [ATLAS Collaboration], ATLAS-CONF-2012-137.

[58] [CMS Collaboration], CMS-PAS-B2G-12-012.

[59] [CMS Collaboration], CMS-PAS-B2G-12-015.

[60] J. C. Pati and A. Salam, Phys. Rev. D **10**, 275 (1974) [Erratum-ibid. D **11**, 703 (1975)].

[61] H. Terazawa, K. Akama and Y. Chikashige, Phys. Rev. D **15**, 480 (1977).

[62] Y. Ne'eman, Phys. Lett. B **81**, 190 (1979).

[63] H. Harari, Phys. Lett. B **86**, 83 (1979).

[64] M. A. Shupe, Phys. Lett. B **86**, 87 (1979).

[65] H. Fritzsch and G. Mandelbaum, Phys. Lett. B **102**, 319 (1981).

[66] I. A. D'Souza and C. S. Kalman, Singapore, Singapore: World Scientific (1992) 108 p

[67] S. Chatrchyan *et al.* [CMS Collaboration], Phys. Rev. D **86**, 052013 (2012) [arXiv:1207.5406 [hep-ex]].

[68] S. Chatrchyan *et al.* [CMS Collaboration], Phys. Rev. Lett. **110**, 081801 (2013) [arXiv:1210.5629 [hep-ex]].

[69] G. Aad *et al.* [ATLAS Collaboration], Phys. Rev. D **85**, 072003 (2012) [arXiv:1201.3293 [hep-ex]].

[70] T. G. Rizzo, Phys. Rev. D **33**, 1852 (1986).

[71] T. G. Rizzo, Phys. Rev. D **34**, 133 (1986).

[72] K. H. Streng, Z. Phys. C **33**, 247 (1986).

[73] A. Celikel and M. Kantar, Turk. J. Phys. **22**, 401 (1998).

[74] J. L. Hewett and T. G. Rizzo, Phys. Rev. D **56**, 5709 (1997) [hep-ph/9703337].

[75] A. Celikel, M. Kantar and S. Sultansoy, Phys. Lett. B **443**, 359 (1998).

[76] M. Sahin, S. Sultansoy and S. Turkoz, Phys. Lett. B **689**, 172 (2010) [arXiv:1001.4505 [hep-ph]].

[77] A. N. Akay, H. Karadeniz, M. Sahin and S. Sultansoy, Europhys. Lett. **95**, 31001 (2011) [arXiv:1012.0189 [hep-ph]].

[78] J. Beringer *et al.* [Particle Data Group Collaboration], Phys. Rev. D **86**, 010001 (2012).

[79] F. Abe *et al.* [CDF Collaboration], Phys. Rev. Lett. **63**, 1447 (1989).

[80] U. Baur and K. H. Streng, Phys. Lett. B **162**, 387 (1985).

[81] W. Bartel *et al.* [JADE Collaboration], Z. Phys. C **36**, 15 (1987).

[82] I. Abt *et al.* [H1 Collaboration], Nucl. Phys. B **396**, 3 (1993).

[83] L. Randall and R. Sundrum, Phys. Rev. Lett. **83**, 3370 (1999) [hep-ph/9905221].

[84] Y. Grossman and M. Neubert, Phys. Lett. B **474**, 361 (2000) [hep-ph/9912408].

[85] T. Gherghetta and A. Pomarol, Nucl. Phys. B **586**, 141 (2000) [hep-ph/0003129].

[86] H. Davoudiasl, J. L. Hewett and T. G. Rizzo, Phys. Lett. B **473**, 43 (2000) [hep-ph/9911262].

[87] A. Pomarol, Phys. Lett. B **486**, 153 (2000) [hep-ph/9911294].

[88] S. Chang, J. Hisano, H. Nakano, N. Okada and M. Yamaguchi, Phys. Rev. D **62**, 084025 (2000) [hep-ph/9912498].

[89] J. M. Maldacena, Adv. Theor. Math. Phys. **2**, 231 (1998) [hep-th/9711200].

[90] M. E. Peskin and T. Takeuchi, Phys. Rev. Lett. **65**, 964 (1990).

[91] K. Agashe, A. Delgado, M. J. May and R. Sundrum, JHEP **0308**, 050 (2003) [hep-ph/0308036].

[92] K. Agashe, R. Contino, L. Da Rold and A. Pomarol, Phys. Lett. B **641**, 62 (2006) [hep-ph/0605341].

[93] K. Agashe and R. Contino, Nucl. Phys. B **742**, 59 (2006) [hep-ph/0510164].

[94] M. S. Carena, E. Ponton, J. Santiago and C. E. M. Wagner, Nucl. Phys. B **759**, 202 (2006) [hep-ph/0607106].

[95] K. Agashe, S. Gopalakrishna, T. Han, G. -Y. Huang and A. Soni, Phys. Rev. D **80**, 075007 (2009) [arXiv:0810.1497 [hep-ph]].

[96] H. Davoudiasl, S. Gopalakrishna, E. Ponton and J. Santiago, New J. Phys. **12**, 075011 (2010) [arXiv:0908.1968 [hep-ph]].

[97] S. Gopalakrishna, T. Mandal, S. Mitra and G. Moreau, arXiv:1306.2656 [hep-ph].

[98] H. Davoudiasl, J. L. Hewett and T. G. Rizzo, Phys. Rev. D **63**, 075004 (2001) [hep-ph/0006041].

[99] S. Gopalakrishna, T. Mandal, S. Mitra and R. Tibrewala, Phys. Rev. D **84**, 055001 (2011) [arXiv:1107.4306 [hep-ph]].

[100] J. Alwall, P. Demin, S. de Visscher, R. Frederix, M. Herquet, F. Maltoni, T. Plehn and D. L. Rainwater *et al.*, JHEP **0709**, 028 (2007) [arXiv:0706.2334 [hep-ph]].

[101] A. Pukhov, E. Boos, M. Dubinin, V. Edneral, V. Ilyin, D. Kovalenko, A. Kryukov and V. Savrin *et al.*, hep-ph/9908288.

[102] A. Pukhov, hep-ph/0412191.

[103] J. Pumplin, D. R. Stump, J. Huston, H. L. Lai, P. M. Nadolsky and W. K. Tung, JHEP **0207**, 012 (2002) [hep-ph/0201195].

[104] S. Gopalakrishna, T. Han, I. Lewis, Z. -g. Si and Y. -F. Zhou, Phys. Rev. D **82**, 115020 (2010) [arXiv:1008.3508 [hep-ph]].

[105] B. Coleppa, T. Mandal and S. Mitra, in preparation.

[106] A. Girdhar and B. Mukhopadhyaya, arXiv:1204.2885 [hep-ph].

[107] K. -i. Matumoto, Prog. Theor. Phys. **52**, 1973 (1974).

[108] O. W. Greenberg and C. A. Nelson, Phys. Rev. D **10**, 2567 (1974).

[109] O. W. Greenberg, Phys. Rev. Lett. **35**, 1120 (1975).

[110] N. D. Christensen and C. Duhr, Comput. Phys. Commun. **180**, 1614 (2009) [arXiv:0806.4194 [hep-ph]].

[111] C. Degrande, C. Duhr, B. Fuks, D. Grellscheid, O. Mattelaer and T. Reiter, Comput. Phys. Commun. **183**, 1201 (2012) [arXiv:1108.2040 [hep-ph]].

[112] J. Alwall, M. Herquet, F. Maltoni, O. Mattelaer and T. Stelzer, JHEP **1106**, 128 (2011) [arXiv:1106.0522 [hep-ph]].

[113] J. Alwall, S. de Visscher and F. Maltoni, JHEP **0902**, 017 (2009) [arXiv:0810.5350 [hep-ph]].

[114] T. Mandal and S. Mitra, Phys. Rev. D **87**, 095008 (2013) [arXiv:1211.6394 [hep-ph]].

[115] D. Goncalves-Netto, D. Lopez-Val, K. Mawatari, I. Wigmore and T. Plehn, Phys. Rev. D **87**, 094023 (2013) [arXiv:1303.0845 [hep-ph]].